DESIGN AND CONTROL OF A
MINIATURE ROTARY ROBOT JOINT

DESIGN AND CONTROL OF A MINIATURE ROTARY ROBOT JOINT

By

RUSSELL SINDREY, B.Eng.Mgt., M.B.A.

A Thesis

Submitted to the School of Graduate Studies

in Partial Fulfillment of the Requirements

for the Degree

Master of Applied Science

McMaster University

MASTER OF APPLIED SCIENCE (2006) McMaster University

(Mechanical Engineering) Hamilton, Ontario

TITLE: Design and Control of a Miniature Rotary Robot Joint

AUTHOR: Russell Sindrey, B.Eng.Mgt., M.B.A. (McMaster University)

SUPERVISOR: Dr. Gary M. Bone, Associate Professor

NUMBER OF PAGES: xvi, 125

ABSTRACT

Over the past 20 years research into miniature actuators has been increasing. In addition to having a compact geometry, desirable characteristics for miniature actuators include having a large power-to-weight ratio, fast response, fine resolution of movement and high power efficiency. In the first part of this thesis the design of a miniature rotary robot joint is presented. Two single acting miniature cylinders each with a bore diameter of 4 mm drive the joint using water as the hydraulic fluid. The cylinders are mated to a rack and pinion mechanism that converts the opposing linear motion of the cylinders shafts into rotation. Also within the design, a novel position sensor using magnetic field sensing technology is presented. Overall, the joint measures 11 mm wide x 8.8 mm high x 150 mm long.

In the second part of this thesis a hydraulic servo positioning system is presented along with a novel valve modeling technique and two position control strategies. Four low-cost, 3-way on/off solenoid valves were used to control the flow of the water in and out of the cylinders. The two nonlinear position controllers employed were a position-velocity-acceleration plus model-based feedforward controller (PVA+FF) and a novel PVA + FF plus sliding mode controller. For experiments involving horizontal rotation of the joint while carrying no load the PVA+FF controller achieved a steady-state error of ± 0.77° or ± 0.06 mm in terms of rack position. The steady-state error produced by the PVA + FF plus sliding mode controller was ± 0.85° or ± 0.07 mm. The maximum tracking

error produced by both controllers was 5^{o} or 0.41 mm and occurred during the initial cycloidal rising portion of a 120^{o} displacement. The root mean square error (RMSE) of the PVA + FF and PVA + FF plus sliding mode controllers were 42 % and 54 % less than that produced by a linear PVA controller.

Both controllers were found to be robust to changes in payload. This was experimentally verified by adding masses of 6.5 g and 13.5 g to the end of the output link of the joint. By conducting similar experiments in the vertical direction it was found that the PVA + FF plus sliding mode controller was more robust, achieving on average a 30 % reduction in RMSE compared to the FF + PVA controller.

ACKNOWLEDGEMENTS

I would like to express my sincere gratitude to my supervisor, Dr. Gary Bone for his guidance and support without which this thesis would not have been possible. I would also like to thank technicians Mr. Mark Mackenzie and Mr. Joe Verhaeghe for their help with the manufacturing and electrical connections for the joint. Finally, I would like to thank my family, friends and colleagues for their encouragement and support.

TABLE OF CONTENTS

LIST OF FIGURES

LIST OF TABLES

ABBREVIATIONS

CCW	Counter clockwise
CW	Clockwise
DZC	Dead zone compensation
FF	Feedforward
I/O	Input/output
PCM	Pulse code modulation
PID	Proportional plus integral plus derivative
PVA	Position plus velocity plus acceleration
PWM	Pulse width modulation
RMSE	Root mean square error
SISO	Single-input single-output
SSE	Steady state error

NOMENCLATURE

θ, θ_d	Measured and desired joint angles
$y, \dot{y}, \ddot{y}$	Measured rack position, velocity and acceleration
$y_d, \dot{y}_d, \ddot{y}_d$	Desired rack position, velocity and acceleration
D_{g1}, D_{g2}	Pinion and spur gear pitch diameters
T_{max}	Theoretical maximum joint torque
F_{max}	Theoretical maximum force generated by miniature cylinder
A	Bore area of miniature cylinder
M	System's dynamic mass (water plus all moving joint components)
β	Bulk modulus
Q	Volumetric flow rate
P_{ws}, P_a, P_b	Water supply pressure, pressure inside chambers A and B
V_H	Hall voltage
E	Magnetic field strength
$V1$, $V2$, $V3$, $V4$	Valves 1, 2, 3, 4
R_1, R_2, R_3, R_4	Flow resistance of valves 1, 2, 3, 4
ΔP	Pressure drop across valve
F_l	Total friction and pressure losses in system
F_c, F_v, F_s	Coulomb force loss, viscous force loss, stiction force
v, v_s	Velocity, Stribeck velocity

e	Position error
u, u_{pva}, u_{FF}, u_{sw}	Duty cycle control signal, PVA signal, FF signal, switching signal
K_p, K_v, K_a	PVA controller gains
K_{OB}	Velocity observer gain
ϕ, ε	Height and width of sliding surface boundary layer
λ	Switching gain

CHAPTER 1

INTRODUCTION

1.1 Preface

Over the past 20 years, interest in miniature actuators has increased substantially thanks in large part to the advancements in micromachining, semiconductor chip technology, smart materials and microprocessing capabilities. Miniature actuators have numerous potential applications including: miniature mobile robots, surgical robots, space robotics, cellular phone vibrators, micro-positioning devices and humanoid robot hands. Although exact performance requirements are application specific, in general miniature actuators should have the following characteristics: compact geometry, large power-to-weight ratio, fast response and high power input efficiency.

Miniature actuators can be classified into two groups: traditional and new age actuators. The traditional actuators consist of miniaturized electromagnetic motors and hydraulic/pneumatic cylinders. New age actuators are primarily made of smart materials that have been developed over the last 20 years or so. They include: shape memory alloys, piezoelectric motors and conductive polymers.

The main challenge in most miniature actuator applications is to identify a suitable actuator that allows for the desired compact geometry while still delivering the required performance. Most of the new age actuators are in their infancy and in most cases are not commercially available. While miniature electromagnetic motors can be readily purchased and their control is well developed, they are not suitable for all applications. Miniature cylinders can also be purchased off-the-shelf, however their control is more difficult than standard size cylinders due to the increased influence of static and coulomb friction. The increase in the friction effects can be explained by noting that the friction is proportional to the cylinder's bore diameter since the seal length equals the bore circumference, while the force of the fluid on the piston is proportional to its area. Therefore, as the cylinder's diameter is reduced the ratio of the friction to piston force increases proportionally. Up to now very little research has been done on the position control of miniature cylinders.

1.2 Objectives and Organization of Thesis

There are two main objectives of this thesis. The first objective is to design and build a miniature rotary robot joint. Also, an appropriate miniature actuator will be selected to drive the joint rotation. The joint is to be designed for a proprietary application and must have overall dimensions of less than 12 mm wide by less than 9 mm high. The joint should also have a rotational range of 180° and be able to produce a maximum torque of at least 30 mNm. The type of actuator used to drive the joint rotation will be selected based on the previously mentioned design requirements for the joint. The second main objective of the thesis is to model the dynamics of the joint servo positioning system and to study servo control strategies for the selected miniature actuator.

The thesis is organized as follows. In chapter 2 previous works in two main areas are reviewed. First, the performance characteristics of various miniature actuator technologies are examined along with a review of their uses in previously designed miniature joints. Second, the literature pertaining to control strategies for low-pressure water hydraulics and on/off solenoid valves is reviewed. In chapter 3 the justification for selecting low-pressure water hydraulics as the actuating means for the joint is given. Also in this chapter, the design of the rotary joint and internal position sensor is presented. Chapter 4 examines the servo positioning system hardware and the modeling of the system dynamics. The system model includes a novel volumetric flow rate model of the on/off solenoid valves, the pressure and friction losses within the system, and the mechanical dynamics of the joint. Two nonlinear controllers are presented in chapter 5. The first controller combines the feedforward of the nonlinear dynamics of the system with linear position-velocity-acceleration (PVA) control. The second controller adds an additional sliding mode control action to further compensate for modeling errors. The simulated and experimental results are presented and compared to results from a linear controller. In chapter 6 the two nonlinear controllers are tested for robustness. Each controller is subjected to tests involving varying payload and vertical motion. Conclusions are outlined in chapter 7, along with the significant achievements of the thesis and recommendations for future work.

CHAPTER 2

LITERATURE REVIEW

2.1 Introduction

In this chapter the relevant research literature pertaining to the fields of miniature actuators and the control of pneumatic and hydraulic servo positioning systems will be reviewed. The review of miniature actuators will cover previous designs, applications, and measured performance. The review of previous works in hydraulic and pneumatic servo positioning control will focus specifically on control methods for low-pressure water hydraulics and simple on/off solenoid valves.

2.2 Miniature Actuators

Over the last 20 years the field of miniature actuators has experienced substantial growth in both academia and industry. The growth has been sparked by the increase in the number of perceived applications for miniature actuators as well as the recent advancements in micromachining, semiconductor chip technology, and the development of new smart materials. While there are numerous types of miniature actuators, this section reviews the five major technologies: electromagnetic motors, hydraulic and pneumatic actuators, piezoelectric motors, shape memory alloy actuators, and conductive polymers.

2.2.1 Electromagnetic Motors

Electromagnetic motors are available as small as 1.9 mm in diameter and 10 mm in length [1]. Miniature motors are typically classified as having diameters of 10 mm or less and are available in one of three types: brush, brushless, or stepper. Brushless motors are used for servo applications requiring a motor with a diameter of less than 6 mm due to the manufacturing size limitations of mechanical brushes. In general, brush motors are not as popular for miniature applications due to the short life expectancy of the brushes caused by the combination of their small size and high motor speeds [2].

Typically, miniature electromagnetic motors can run at speeds as high as 100,000 rpm, produce torques between tens and hundreds of micro-newtons depending on their size, and have power-to-weight ratios of less than 0.25 W/g [1] [3] [4]. The generated torque can be increased by attaching a gearhead to the motor at the cost of enlarging the overall size of the actuator. The loss of generated torque with decreasing size of the motor can been observed from equation 2.2.1 [5] given by,

$$T = kD^2L \tag{2.2.1}$$

where D and L are the armature diameter and length respectively, and k is a constant which depends on the magnetic field source, the bearings, and the brushes, if any. The equation states that the decrease in torque is proportional to the cube of the decrease in the armature dimensions.

Several researchers have studied the use of miniature motors as a means of actuation for miniature robotic applications. Yamashita et al used two DC brushless servomotors to drive a 2 degree-of-freedom (DOF) bending mechanism for a miniature robot manipulator [6]. The overall diameter of the mechanism was 9 mm and it consisted of two 1 DOF parallel slider linkage sets. One linkage in each of the two sets was connected to a motor via a lead screw that transformed the rotation of the motor shaft into linear motion of the linkage. One linkage set was orientated in the horizontal plane and the other in the vertical plane allowing the mechanism to bend both horizontally and vertically. The mechanism had a rotational range of $\pm 90^{o}$ in each plane and the linear motion of the individual slider linkages was repeatable to less than 1 mm.

Peirs, Reynaerts, and Van Brussel used a RMB SMOOVY brushless DC servomotor to drive the bending action of a miniature joint [7]. The motor was 3 mm in diameter, 7 mm long, and capable of producing 25 μNm of continuous torque. The joint consisted of the motor, its housing body, a planetary gearbox, a platform representing the second link in the chain, and a worm gear set. The planetary gearbox and worm gear assembly resulted in a gear reduction of 1:700. The joint measured 12 mm in diameter by 20 mm long, had a rotational range of $\pm 40^{o}$, generated torque of up to 1.1 mNm and had a maximum speed of 260 deg/s.

In their creation of a miniature mobile robot Dario et al designed an electromagnetic motor known as a wobble motor [8]. The designed wobble motor consisted of a star shaped stator with three coils located inside an external ring rotor. When two of the three coils were supplied current a magnetic field was generated which encloses around the rotor. The resulting magnetic forces cause the rotor to be drawn towards the two powered coils. By turning on different pairs of coils in procession the rotor rotates around the stator much like a person using a hula-hoop. The mobile robot is made up of two wobble motors that act as the active outside wheels, an inside frame to hold the structure together, and two passive wheels attached to the frame to help maintain the robots balance. Each wobble motor was 9.2 mm in diameter and only 3 mm long. The maximum rotational speed of the motor was 170 rpm and its stall torque was 160 μNm. The mobile robot had a volume of only 1000 mm^3 and maximum linear speed of 90 mm/s.

In order to apply closed-loop control to miniature rotary motors, miniature encoders are necessary to sense the positional change of the motor shaft. Unfortunately, encoders for use with motors 5 mm in diameter or less are not commercially available. However, in their research Nicoud, Matthey and Caprari developed a miniature rotary encoder with a diameter of 3 mm [2]. The encoder had a resolution of 6 slots per turn and was attached to an RMB SMOOVY brushless motor. During manufacturing it was found that the small size of the encoder caused degradation of the relative precision of the slots. This resulted in alignment errors of up to 20 % that added to the complexity when calibrating the encoder.

2.2.2 Hydraulic and Pneumatic Actuators

Hydraulics and pneumatics have received attention from researchers over the past 20 years for miniature actuator applications due to their relatively high power-to-weight ratios and compact geometries. In general, hydraulic actuators are better suited for applications requiring higher forces and slower speeds when compared to pneumatic actuators.

In 1989, Fukuda, Hosokai and Uemura developed an in-pipe inspection mobile robot using flexible pneumatic actuators [9]. The robot was designed to inspect the inside of 2" diameter pipes within a nuclear power plant. The robot consisted of three modules, each containing four flexible rubber pneumatic actuators located at 90° increments. Two types of flexible actuators were used: a stretch type and a shrink type, otherwise known as the Mckibben artificial muscle. The shrink type contracts when pressurized, while the stretch type expands. Each actuator consisted of a rubber tube with an inside diameter of 3 mm and an outer diameter of 5 mm, a nylon sleeve and two support caps, one of which had an inlet/outlet port for the gas. The two outside modules contained shrink type actuators while the middle module contained the stretch type. The linear locomotion of the robot resembled that of an inchworm. In order to move along the pipe, the shrink actuators on one end would be pressurized causing their diameters to inflate. The resulting holding force between the pressurized tubes and the inner wall of the pipe held the module in place while the stretch actuators were pressurized, pushing the other end module forward. The tubes in the displaced end module would then inflate, holding that end of the robot in place while the other two modules were de-pressurized causing them to be pulled forward. The robot could also bend by pressurizing the appropriate stretch actuators inside the middle module. The flexible actuators could produce upwards of 7.5 N at a supply pressure of 0.39 MPa.

Flexible hydraulic or pneumatic actuators can also be designed using bellows. In 1998, Kallio et al used hydraulic bellows to develop a 3 DOF parallel micromanipulator used for tasks involving micrometer movements [10]. Three bellows were arranged in a tripod-like setting atop a base and connected to a mobile platform that held a thin needle end-effector. The bellows were elongated by filling them with hydraulic oil that was stored in a tank inside the base. The x-y-z position of the end-effector was varied by filling any combination of the three bellows with oil. The flow of oil was regulated by three piezoelectric actuators that were submerged inside the oil tank. Each of the piezoelectric flow actuators was connected to a bellows. When a voltage was supplied to the actuator it deformed forcing oil from the tank into the bellows, causing it to elongate. Due to the small motion range of the piezoelectric actuator (± 250 μm), very fine resolution in the control of the oil flow was possible. Consequently, the manipulator had a displacement resolution of less than one micrometer.

In 1991, Suzumari, Iikura and Tanaka developed a flexible microactuator that could be powered using either air or hydraulic fluid [11]. The actuator consisted of small tube that was split into three equal chambers. Connected to each chamber was a tiny tube, which supplied the air or hydraulic fluid to the chamber. By varying the pressures and/or fluid volume inside each of the chambers the researchers could control any one of the actuator's three degrees-of-freedom: pitch, yaw, and stretch. Fibre-reinforced rubber was used to construct the tube and chamber walls of the actuator giving it its flexibility. The researchers developed a series of flexible microactuators with outside diameters ranging between 1 and 20 mm and implemented them as artificial robot fingers for manipulating light weight objects.

In 1999, researchers Peirs, Reynaerts and Van Brussel developed their own miniature hydraulic cylinders for use in a parallel bending manipulator [12]. The cylinders had an internal diameter of 3 mm, a stroke of 10 mm, and at a pressure of 10 bar could generate a theoretical force of 7 N. However, the cylinder's net usable force was less due to friction effects, which were quantified experimentally as between 0.4 to 0.9 N for the static friction and between 0.3 to 0.4 N for the dynamic friction. The difference in the two friction values, known as the stick-slip effect, caused notable positioning problems. The manipulator contained three cylinders arranged in an equilateral triangle arrangement and was 12 mm in diameter and 30 mm long. The three cylinders were connected to a top platform through the use of ball bearings. The manipulator had a rotational capability of 30 – 35 degrees and used silicon oil as its working fluid. The silicon oil was supplied to the cylinders through piezoelectric valves that the researchers designed. The valves contained a piezoelectric stack and were designed to be normally open. Due to the stack's small displacement capability of 6 μm, difficult, precise assembly of the valve was required. Also, a voltage of 100 V was necessary in order to fully close the valve.

2.2.3 Piezoelectric Motors

Miniature piezoelectric motors (also known as ultrasonic motors) represent a higher torque, lower speed alternative to miniature electromagnetic motors. A piezoelectric motor can generate up to six times the torque of a similar size electromagnetic motor, achieve speeds upwards of 1000 rpm and have power-to-weight ratios in the range of 3 to 5 W/g [13].

A piezoelectric motor typically has a fairly simple structure consisting primarily of a stator made of piezoelectric ceramic and a rotor. While several ceramic stator geometries are possible, the operating principal remains virtually the same. A high frequency voltage supply of around 30 to 50 kHz is supplied to the piezoelectric ceramic, which in turn exhibits high frequency mechanical vibrations. These vibrations cause the rotor that is in contact with the stator to float across the stator's surface [1]. Both linear and rotary piezoelectric motors can be created depending on the geometry of the stator and rotor. The torque of the motor is generated from the friction force between the stator and the rotor. Adhesive films are sometimes applied to the surface of the rotor to increase the friction force [1].

Currently, commercial piezoelectric motors can be found as small as 3 mm in diameter. Physkinstrument produces a miniature piezoelectric motor that is 3 mm in diameter, 6 mm long, produces a maximum torque of 0.4 mNm, and has a maximum speed of 1000 rpm [14].

In addition to the commercial activity, many researchers have begun studying piezoelectric motors for their potential use in miniature drive applications. In 1997, Flynn developed a miniature piezoelectric rotary motor 3 mm in diameter and 8 mm long [15]. The stator element was made into the shape of a ring using bulk PZT ceramic. The motor was capable of a no-load speed of 1710 rpm and a peak power output of 27 mW, while having a stall torque of 10 mNm.

Tani et al developed a unique stator geometry for their piezoelectric motor in 1998 [16]. The motor consisted of a disk-shaped rotor and a cantilever stator with piezoelectric elements made of PZT ceramic attached to its underside. As the PZT elements oscillated under an AC supply voltage, the oscillations were transferred to the stator causing the rotor to rotate across the stator surface. The motor measured 2 mm in diameter by 2 mm high and was capable of speeds between 50 – 450 rpm. No torque data was given in their paper.

In 1998 Bexell and Johansson created a piezoelectric motor using PZT bulk ceramic in the form of beam elements [17][18]. Their configuration contained six beam elements, which were stood on end and fastened to the surface of a disk-shape stator. A disk-shaped rotor was then placed on top of the other ends of the beam elements. As the free ends of the beam elements vibrated, they pushed the rotor causing it to rotate. Under a maximum supply voltage of 50 V and a fixed drive frequency of 10 kHz the motor generated a maximum torque of 3.5 mNm and a no-load speed of 65 rpm.

As an alternative to using bulk PZT ceramic, in 2003 Dong et al fabricated a piezoelectric motor using a PZT film metal composite tube as an oscillating stator [19]. The motor shaft was inserted through the center of the tube and its rotation was driven by the first bending mode of the tube. The motor was subjected to a maximum supply voltage of 80 V at a drive frequency of 67 kHz. The diameter and length of the motor was 1.5 mm and 7 mm respectively. The motor was capable of a maximum torque of 45 μNm and a no-load speed of 2000 rpm.

2.2.4 Shape Memory Alloy Actuators

Shape memory alloy (SMA) wires have become of interest to researchers due to their very small diameters (down to 25 μm [20]) and capability of producing large unit forces as high as 150 N/mm^2 [21]. SMA wires are deformed at a 'cold' temperature and are able to revert back to their 'memorized' shape when heated above a critical transition temperature [22]. The 'memory effect' exhibited by SMA wires is driven by a crystalline phase transition from martensite to austenite that occurs as the wires are heated through the application of electric current. The martensite phase behaves in a plastic manner and is easily deformed. As the SMA wire realigns its crystal lattice to an austenite phase, the wire becomes increasingly elastic and as its stiffness rises, large unit forces are generated in the wire. SMA wires can be one of two types: SMA 1 or SMA 2 [23]. SMA 1 wire is cold deformed at a temperature around 20°C and has a transition temperature that can range from 60°C to 90°C. The transition temperature of SMA 2 wire is set around 0°C so that it will behave in an elastic manner at room temperature.

SMA 1 wires need to be coupled with a return force in order to revert back to their cold deformed state after heating. Usually this force is supplied through the use either a bias spring or a SMA 2 type wire. It is well known among researchers in the SMA field that SMA wires have much faster response times during heating (ms) than they do during the cooling phase (s).

Several miniature actuator mechanisms have been developed by various researchers using SMA materials. Ikuta, Tsukamoto and Hirose were among the first researchers to use SMAs for miniature robot actuator applications [24]. In 1988, they developed an SMA actuator consisting of 5 identical segments each 13 mm in diameter and 40 mm long. Each segment consisted of a central stainless steel spring that provided the return force for the mechanism, surrounded by a series of SMA springs made of Ti-Ni alloy. In an effort to speed up the cooling phase of the SMA springs and reduce the outside temperature of the mechanism a tube filled with water was inserted through the central return spring to indirectly cool the SMA springs. In order to heat the SMA springs to the transition temperature of 60°C, 1 A of current was required. In terms of performance, each segment had a maximum bending angle of 60°, maximum torque capability of 6.9 Nm, maximum speed of 30 deg/s, and a power-to-weight ratio of approximately 0.56 W/g. The time responses in the heating and cooling phases were not given.

Peirs, Reynaerts and Van Brussel have developed several miniature actuators driven by SMA wires [21][25]. One such device was a snake-like robot made up of modular bending actuators as described in [25]. Each module contained straight SMA wires that supplied the active force and two elastic spring hinges, which provided the restoring force. During the tests of their various devices they observed that the SMA wires provided maximum strain rates of 3 % and unit forces of 150 N/mm^2 [21]. The researchers noted several problems relating to the SMA actuators [21]. The small diameters of the SMA wires made it difficult to clamp the wires inside the mechanisms and to make the required miniature electrical connections. Also, the low electrical resistance of the wires meant that high currents needed to be used to generate sufficient heat. Consequently, the SMA actuators were found to have very low efficiencies on the order of 1 %. In addition, the small strain rate of the SMA wire meant that relatively long wires had to be used in order to obtain reasonable displacements, reducing the compactness of the actuators. Finally, hysteresis of up to 20 % was found to be present in the temperature - phase transformation relationship. This coupled with the non-linear stress-strain relationship of the wire made the actuators very difficult to control.

In 2001, Ascada, Mascaro and Roy developed a 'wet actuator' consisting of a 1.5 mm diameter SMA wire embedded in a compliant, 3 mm diameter water-filled vessel [26]. The actuator resembled that of an artificial muscle that contracted when the SMA wire was heated past its transition temperature of 90°C. The SMA wire was submerged into water, which continuously flowed through the vessel to supply direct cooling through forced convection. The authors stated that it has been shown in previous research that forced convection can decrease the relaxation (cooling) time of an SMA wire to ¼ the time required for natural convection [26]. In addition to its role in cooling, the water was pressurized so that it could act as the return force mechanism. The wet actuator design was able to reach cycle speeds of up to 1.5 Hz.

In 2004, Hino and Maeno developed a joint for a robot finger that was actuated by an SMA wire [27]. The SMA wire was connected to a return spring and a parallel configuration was created through the use of a pulley. The joint rotated in one direction when current was supplied to the SMA wire and was pulled back to its initial position by the return spring as the SMA wire cooled. The SMA wire was cooled by natural air convection. Various diameters of SMA wire were tried in the joint ranging from 0.5 mm to 2.0 mm. From these tests it was observed that as the diameter increased, the force increased from 0.9 N to 6.7 N. However, both the contraction (heating) and extension (cooling) velocities of the joint decreased from 5.6 mm/s to 2.5 mm/s and 3.9 mm/s to 0.1 mm/s respectively. It can be seen from this velocity trend that the ratio of the extension velocity over the contraction velocity also decreased from 0.7 to 0.04. Hence, the cooling time becomes a more significant restriction on the cycle speed of the actuator as the wire diameter increases. The contraction ratio of the wire was also found to decrease from 5 % to 3 % with the increase in the SMA wire diameter.

2.2.5 Conductive Polymer Actuators

Conductive polymers are a special kind of actuator that use a reversible ion transport mechanism found in redox reactions to generate displacement [28][29]. The actuator consists of two conductive polymer electrodes sandwiched around an electrolyte solution. A voltage is supplied across the two electrodes inducing an electrochemical reaction in which ions transfer from one electrode to the other through the electrolyte. As the ions move, the volumes of the electrodes change causing them to deform. Depending on the configuration of the actuator this will result in either a bending action or a linear expand/contract motion.

Conductive polymers have received notable attention for use as miniature actuators due to their large stress capability, low voltage requirements, and relatively large strains compared to piezoelectric and shape memory alloys. The average voltage requirement for a conductive polymer actuator is between 1 – 5 V while they can generate strains between 0.5 % and 10 % [30] and stresses up to 25 Mpa [31]. However, due to their very slow cycle times (on the order of several seconds) conductive polymers have average power-to-weight ratios of only 0.04 W/g [32].

In 2000, Jager, Ingemar and Lundstrom developed a micro robot arm using conductive polymers [33]. The conductive polymer electrodes were made of polypyrrole-gold bilayers and the robot was submerged in an aqueous solution that acted as the medium for the ion transport mechanism. Overall, the robot was 670 μm long, 250 μm wide and consisted of a bendable arm and an end-effector with three bendable fingers. The robot was programmed to pickup a 100 μm bead and move it a distance of 67 μm in a repeatable manner.

It is often desirable to operate conductive polymers in a linear displacement configuration in order to fully take advantage of the stresses they induce. Della Santa, Rossi and Mazzoldi created one such linear actuator in 1996 [30]. The actuator in question consisted of a 32 μm thick polypyrrole film doped with benzensulphonate anions that was submersed in a liquid electrolyte bath, which acted as an ionic reservoir. The conductive film was capable of strains between 0.5 – 10 %.

In order to make conductive polymers useful for robotic applications it is necessary that they be able to operate outside a solution-based environment. In order to accomplish this, Madden et al replaced the normally used liquid electrolyte with an electrolyte gel and fully encapsulated the actuator in a polyethylene film held together by gold-coated clamps [34]. The active electrode was made of 40 μm thick polypyrrole film. The actuator was able to generate 0.5 Mpa of stress and 2% strain.

Hara et al created artificial muscle fibres using polypyrrole-metal coil composites [31]. The composite was encapsulated with an electrolyte solution and a counter electrode, which surrounded the inside wall of the capsule. The voltage to the actuator was cycled between –0.9 V and 0.7 V causing the muscle fibre to contract and elongate. The fibres had a maximum strain capability of 8 %, but moved very slowly taking 20 s to reach a strain rate of just 4 %. The muscle fibres were however capable of generating high stresses with a bundle of 10 fibres, measuring roughly 1 mm in diameter, exerting 2.26 N of force.

2.3 Position Control of Low-Pressure Water Hydraulics and Servo Systems Using On/Off Solenoid Valves

In this section two areas of position servo control are reviewed that are relevant to the work presented in the following chapters of this thesis. These areas are: position control of low-pressure water hydraulics and position control of hydraulic and pneumatic servo systems using on/off solenoid valves.

Researchers have recently begun to explore the use of low-pressure water hydraulics as a means of actuation for robotic and servo positioning applications. Cho et al utilized low-pressure water as the fluid medium for their positioning system, which consisted of a double-acting cylinder, a proportional 4/3 solenoid valve, and a 200 kg payload mass [35]. The designed controller consisted of three parts: 1) a feedforward term with the goal of cancelling the poles and zeros from the linear model of the valve, cylinder, mass and viscous friction term, 2) non-linear static and coulomb friction compensation and 3) discrete sliding mode action. The linear model used in the feedforward term was derived using the Bezout identity. For the experiments, the sampling time was set to be 0.01 s and the water supply pressure was set at 30 bar. The horizontal position control of the system was tested over a multi-step response with smooth trapezoidal trajectories and a motion range of 100 mm. The worst-case measured steady state and tracking errors were 0.23 mm and 5 mm respectively.

Linjama et al used low-pressure water hydraulics along with low cost on/off solenoid valves to position control a hydraulic cylinder [36]. Their hydraulic positioning system consisted of a double-acting cylinder with a bore diameter of 32 mm and 500 mm stroke, eight on/off solenoid valves and a load mass. The eight valves were arranged in pairs with one valve in the pair connecting one of the cylinder chambers to the water supply and the other valve acting as a discharge for the opposing chamber. The researchers implemented and compared three different control strategies: 3 state control, 5 state control and modified 3 state control. In the 3 state control scheme only four of the valves were used with one of the two valve pairs being activated depending on the direction of the error. In this manner only one velocity was possible in each direction. To achieve dual velocity control, the 5 state control scheme used all eight valves. The high velocity was achieved by activating two parallel sets of valves, while the low velocity was activated in the same manner as in the 3 state controller. The desired velocity was selected based on the proximity to the desired end position. A modified 3 state control scheme was introduced in order to obtain dual velocity with only using four valves. In this scheme the low velocity was obtained by only activating one of the discharge valves, while the high velocity was achieved as in the 3 state control. In all three control schemes a breaking distance parameter was used to determine when to shut off the valves in order to reach the desired position. Experiments were conducted using three load masses: 28 kg, 100 kg and 200 kg. The water supply pressure and sampling time of the controller were set at 30 bar and 2 ms respectively. For a step response of 20 mm, worst-case steady state errors of 0.4 mm, 0.2 mm and just under 0.3 mm were observed for the 3 state, 5 state, and modified 3 state controllers respectively. The researchers also found that while the mass affected the pressure transients within the system it did not noticeably affect the positional error.

Due to their low cost many researchers have studied the use of on/off solenoid valves as an alternative to more expensive proportional valves for both hydraulic and pneumatic applications. One of the first researchers to due this was Noritsuga, who in 1987 used two 3/2 on/off solenoid valves coupled with an automobile-type fuel injection valve to position control a double-acting pneumatic cylinder with a bore diameter of 50 mm and a stroke of 200 mm [37]. The two 3/2 solenoid valves were set up to discharge the air from the cylinder chambers when shut off and supply air when activated. The fuel injection valve was of normally closed type and when open allowed the air to flow in either direction between the two chambers. The 3/2 valves were activated using simple on/off control, while the fuel injection valve utilized a technique known as pulse-width-modulation (PWM), in which the valve is activated for a desired length, or duty cycle, of a predefined time period. In his experiments, Noritsuga used a pulse-width time period of 20 ms, giving a control frequency of 50 Hz. The duty cycle for the injection valve was calculated proportionally to the positional error. The system demonstrated a worst-case steady state error of 0.4 mm and a rise time of 0.9 s for a step input of 50 mm.

Kurz et al also used the PWM control method to position control a flexible fixturing device driven by two hydraulic cylinders [38]. The system consisted of 2, 4/3 solenoid valves connected in series with four flow control valves and two double-acting hydraulic cylinders. The pulse-width period used was 24 ms and as in [37], the duty cycle to the valves was proportional to the positional error. Accuracy in piston positioning to within 0.001 inches was reported.

Van Varseveld and Bone developed a novel PWM algorithm as part of a control strategy for the position control of a payload mass driven by a double-acting pneumatic cylinder with a bore diameter of 27 mm and a 152 mm stroke [39]. The algorithm coordinated the duty cycles of the system's two on/off solenoid valves in order to overcome the valves' dead zones. This produced an almost linear relationship between the cylinder velocity and PWM control signal. The overall controller design consisted of PID control with friction compensation and position feedforward. The position feedfoward term was calculated using the linear process model obtained from experimental data and the application of system identification techniques. A worst-case steady state error of 0.21 mm and rise times of 180 ms for step inputs from 0.11 mm to 64 mm were observed along with a maximum tracking error of 2 mm to a 64 mm S-curve profile. In addition, the controller was robust to a 6 times increase in system mass.

One alternative to PWM is a method known as pulse-code-modulation (PCM). PCM consists of using a series of on/off solenoid valves of differing orifice diameters that act to approximate the behaviour of a single proportional valve. The valve set is controlled using a binary array to specify the state of each valve (on or off). Rong et al used a form of PCM to control the horizontal positioning of a double-acting cylinder [40]. The researchers used a binary array consisting of six 2-way on/off solenoid valves to control the flow rate of the hydraulic fluid and a 4/3 solenoid valve to control the direction of the flow between the two cylinder chambers. From their experimental trials a best-case positional accuracy of between 0.2-0.3 mm was observed.

On/off solenoid valves have also been controlled using sliding mode control. In [41] simulation results for controlling an on/off solenoid driven hydraulic valve spool is presented. Paul et al used sliding mode control to control the positioning of a double-acting pneumatic cylinder [42][43]. The cylinder had a bore diameter of 25.4 mm and a 305 mm stroke. The airflow to the two chambers was independently controlled through the use of four on/off solenoid valves. The sliding surface used by the controller was defined as a line and no boundary layer was implemented. For a step input of 126 mm a maximum steady state error of approximately 1 mm was observed.

2.4 Summary

Over the past 20 years the research into miniature actuator technologies has been on the rise. The technologies that have received the most attention are electromagnetic motors, pneumatic and hydraulic actuators, piezoelectric motors, shape memory alloy actuators and conductive polymers. The latter is by far the youngest technology and has only been actively studied over the past 10 years. These along with shape memory alloys show enormous potential as miniature force actuators due to their large unit force capabilities (25 Mpa for conductive polymers and 150 Mpa for shape memory alloys) and their compact geometries compared to the other technologies. However, the use of these actuators is currently limited due to their slow response times. Electromagnetic and piezoelectric motors have been found to provide high speeds and fast response, but produce very small output torque. The use of miniature hydraulic and pneumatic actuators has not been investigated to the same extent as electromagnetic and ultrasonic motors or shape memory alloys. Although research in the area is limited the existing work has shown that these actuators have been operated at pressures up to 10 bar.

Servo positioning control of low-pressure water hydraulic actuators is a newly emerging field. Over the past six years the researchers at Tampere University of Technology in Tampere Finland have been the lone contributors using various control techniques along with both proportional and 2/2 on/off solenoid valves to position control double-acting cylinders. However, the cylinders tested were relatively large with bore diameters over 30 mm.

On/off solenoid valves have been extensively used over the last 40 years in hydraulic and pneumatic position control due to their low cost. The predominant valves used by researchers have been the 2/2 and 3/2 solenoid valve types. Control of these valves has evolved from simple on/off control to the use of PWM and sliding mode control techniques.

CHAPTER 3

DESIGN OF JOINT MECHANISM

3.1 Introduction

In the beginning of this chapter an explanation is given for selecting low-pressure water hydraulics as the actuation means for the joint. Next, the overall mechanical structure of the miniature joint is described. This is followed by an examination of the kinematics and dynamics of the joint. Finally, the design process for the internal position sensor is outlined.

3.2 Justification for Low-Pressure Water Hydraulics

Low-pressure water hydraulics was selected as the actuation means for the miniature joint for several reasons. First, hydraulic actuators have very favourable mechanical characteristics, including a high power-to-weight ratio, large mechanical stiffness, smooth motion, and the ability to achieve a high level of accuracy. In addition, the alternative technologies were found to be, at present, incapable of meeting the application requirements as described in chapter 1. Electric and piezoelectric motors have very small power-to-weight ratios and are not capable of meeting the combined size and torque requirements for the application. SMA and conductive polymers, while capable of producing high unit forces, presently have very slow response times that make them impractical for servo positioning applications. Standard sized pneumatic cylinders have been quite successful in servo positioning systems. However, the compressibility of the air makes pneumatics harder to control and less accurate than hydraulics. These issues magnify when implementing miniature cylinders as observed in [44].

3.3 Structure of Mechanical Joint

The designed miniature hydraulic joint measures 11 mm wide x 8.8 mm high x 150 mm long and contains several main components: two miniature cylinders, a gear assembly, an output link, a position sensor assembly, and a top and bottom housing to hold the joint together. This section focuses on the mechanical components. The position sensor design will be explored in detail in section 3.5.

A 3D model of the internal assembly of the joint is shown in Figure 3.3.1.

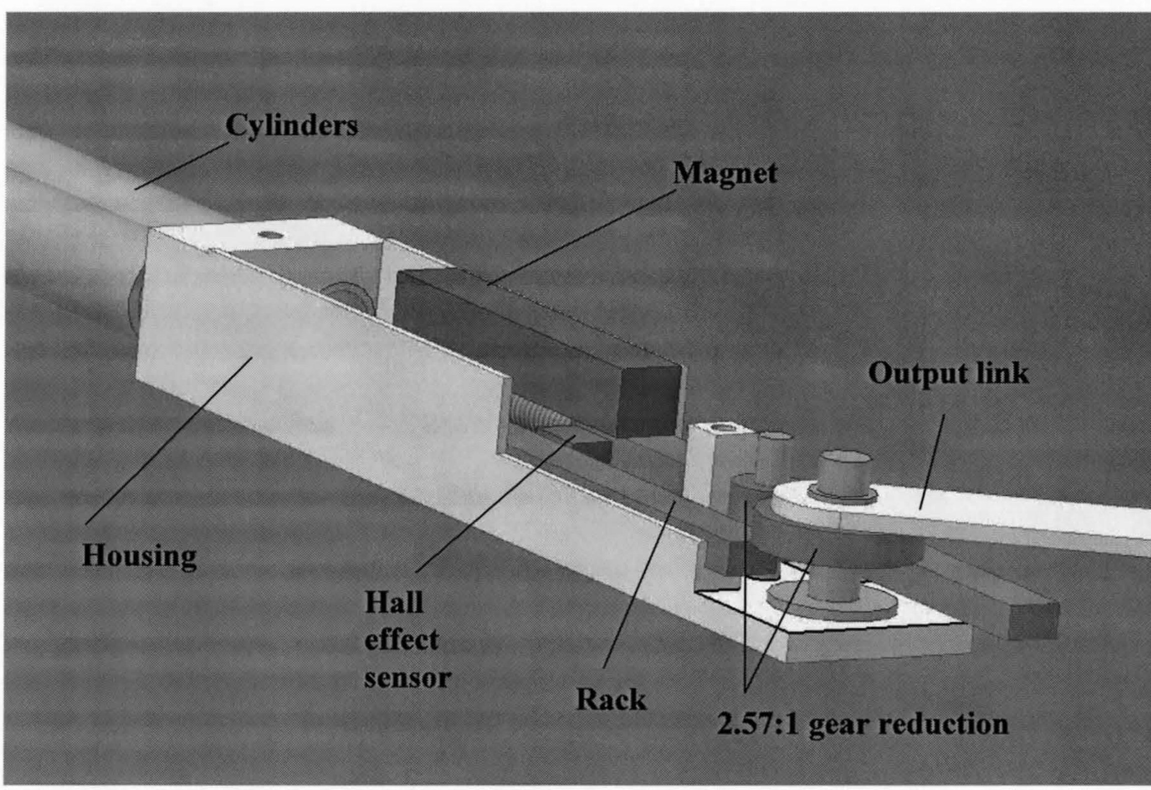

Figure 3.3.1: Internal assembly of miniature robot joint

Double-acting cylinders with a bore diameter of less than 9.5 mm are not commercially available. Therefore, in order to obtain reversible joint rotation, two pneumatic single acting cylinders with 4 mm bore diameters were combined with a rack and pinion assembly. The cylinders were modified for use with water by increasing their inlet orifices. In addition, the return spring inside each cylinder was removed to eliminate the return force. The push-push configuration of the joint is shown in Figure 3.3.2.

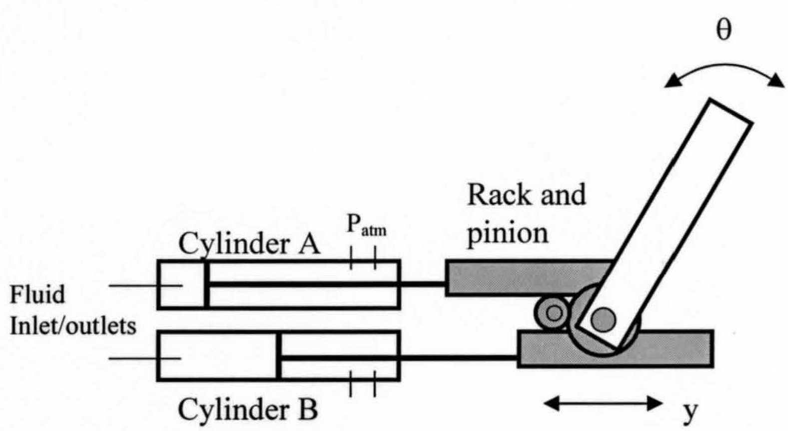

Figure 3.3.2: Push-push joint configuration

The rack and pinion assembly consists of two racks meshed with a pinion gear. This push-push configuration couples the motion of the two cylinder rods together, resulting in the desired reversible joint rotation. A larger spur gear is also coupled with the pinion in order to increase the joint torque through gear reduction. The corresponding gear ratio between the spur gear and pinion is 2.57:1.

The top and bottom housings for the joint were designed to act as a guide way for the racks as well as provide structural support for the joint assembly.

3.4 Joint Kinematics and Dynamics

The miniature robot joint converts the linear motion of the cylinder rods into rotational motion through the use of a designed gear assembly structure. A key objective of the joint was to generate as much useful torque as possible while remaining within the bounds of the size limitations. Since the joint needed to be less than 12 mm wide, the largest commercially available gear that could be used had an outside diameter of 0.417" (10.6 mm) and a pitch diameter of 0.375" (9.525 mm). The pitch diameter of the pinion gear was 0.146" (3.71 mm). From these dimensions the relationship between the linear position of the cylinder rods (mm) and the angle of the joint (deg) can be given as:

$$\theta = \frac{y}{\pi \times D_{g1}} \times \frac{D_{g1}}{D_{g2}} \times 360^0 \tag{3.4.1}$$

where y is the linear position, and D_{g1} and D_{g2} are the pitch diameters of the pinion and larger spur gear respectively. From equation 3.4.1, the linear to angular motion relationship is found to be: 1 mm = 12°. One can see from this relationship that a small error in the cylinder rod position can lead to a relatively large error in the angular position of the joint. This amplification in error is due to the small size of the gears used and represents a major challenge when attempting to control the joint. The overall range of rotation of the joint was designed to be 180°. While the maximum stroke of the miniature cylinders is 20 mm, giving a maximum achievable joint rotation of 240°, the range was limited so that the cylinders would not bottom out, leading to damage of the cylinder piston and seals.

The maximum theoretical force that can be exerted by the miniature cylinders at their rated maximum pressure of 700 kPa is 8.8 N. Therefore, the maximum theoretical joint torque can be determined by:

$$T_{\max} = F_{\max} r = F_{\max} \times \frac{D_{g1}}{2} \times \frac{D_{g2}}{D_{g1}} \tag{3.4.2}$$

where D_{g1} and D_{g2} are the pitch diameters of the pinion and spur gear respectively. From equation 3.4.2 the maximum theoretical torque generated by the joint is 42 mNm. Of course in reality the dynamic torque of the joint is less due to the friction forces that the joint must overcome.

3.5 Safe Gear Load Calculations

Due to the small size of the brass gears used in the joint it is necessary to make sure that the gear teeth can withstand both the maximum theoretical dynamic and static loads. The maximum dynamic load that can be safely applied to a gear tooth is calculated using the maximum theoretical pitch velocity of the gears. In the actual joint the maximum velocity would be affected by friction and pressure losses caused by the valves, tubes, connectors, and inlet ports of the cylinders. However, if any of these components were changed the safe tooth load would also change. Therefore, to make the calculations more robust to changes in the hydraulic system and to add in a factor of safety, it was deemed appropriate to exclude the friction and pressure loss effects from the safe tooth load calculations.

By excluding all friction and pressure loss effects, the dynamic equation of the joint reduces to:

$$\Delta F = P_{\max} A = P_{\max} \pi \frac{D^2}{4} = Ma \tag{3.5.1}$$

where D is the bore diameter of the miniature cylinder, P_{max} is the maximum rated pressure of the cylinder, M is the mass of the water and all moving components of the joint, and a is the acceleration of the racks (m/s^2). Given that D = 4 mm, P_{max} = 700 kPa[1] (7 bar), and M = 0.0329 kg, the acceleration of the joint racks is found to be 267.48 m/s^2. The calculation of the system's moving mass can be found in appendix A. The maximum velocity can be found using:

$$v_f^{\,2} = v_i^{\,2} + 2ad_{\max} \tag{3.5.2}$$

and:

$$d_{\max} = \frac{\theta_{\max}}{360^0} \times C_{g2} = \frac{175^0}{360^0} \times \pi \times 9.525\,\text{mm} \tag{3.5.3}$$

where d_{max} is the maximum distance travelled by the rack, θ_{max} is the maximum corresponding joint rotation, and C_{g2} is the circumference of the spur gear. Assuming the joint starts at rest (v_i = 0), the maximum velocity reached by the rack is 2.79 m/s.

The equation used to determine the safe gear tooth load is given by [45]:

$$W = \frac{SFY}{D_p}\left(\frac{600}{600+v}\right) \tag{3.5.4}$$

where W is the safe gear load in lbs, S is the safe static stress in psi, F is the face height of the gear in inches, Y is the tooth form factor, D_p is the diametral pitch of the gear, and v is the pitch line velocity in ft/min. Since the face height of the pinion and spur gears are different, 0.125" and 0.0625" respectively, the safe tooth load must be calculated

[1] All pressure values given in thesis are gauge pressures.

separately for each. Using data from the tables provided in [45] and noting that v = 2.79 m/s = 549.2 ft/min, the safe tooth loads calculations are as follows:

$$W_{g1} = \frac{12{,}000 \times 0.125'' \times 0.176}{48}\left(\frac{600}{600+549.2}\right) = 2.87\,\text{lbs} \approx 12.78\text{ N}$$

$$W_{g2} = \frac{12{,}000 \times 0.0625'' \times 0.270}{48}\left(\frac{600}{600+549.2}\right) = 2.20\,\text{lbs} \approx 9.80\text{ N}.$$

Hence, the dynamic loads that can be safely applied to the pinion and spur gear respectively, are 12.78 N and 9.80 N. Both safe loads are greater than the maximum theoretical force of 8.8 N generated by the miniature cylinders. Also, the maximum velocity used in the calculations is greater than would be achieved in the real system. Therefore, the gear teeth on both gears will hold for all possible dynamic conditions.

The maximum safe gear load in the static case can be calculated using equation 3.4.4 and setting $v = 0$. For the static case, the safe gear loads for the two gears are:

$$W_{g1} = \frac{12{,}000 \times 0.125'' \times 0.176}{48}\left(\frac{600}{600+0}\right) = 5.5\ \text{lbs} \approx 24.47\text{ N}$$

$$W_{g2} = \frac{12{,}000 \times 0.0625'' \times 0.270}{48}\left(\frac{600}{600+0}\right) = 4.22\,\text{lbs} \approx 18.78\text{ N}.$$

Therefore, the static loads that can be safely applied to the two gears are 24.47 N and 18.78 N respectively. Again, both of the safe loads are above 8.8 N, so the gear teeth will not fail under static loading.

3.6 Design of the Hall Effect Position Sensor

Typically in robotic applications it is desirable to locate positional sensors, such as rotary encoders, as close to the joint as possible to maximize the accuracy of the measurements. Due to the small size and compactness of the hydraulic robot joint a miniature positional sensor was required. Ideally, one would choose a miniature rotary encoder to measure the change in joint angle directly. Unfortunately, no encoders were commercially available that met the size requirements so other miniature sensory technologies had to be pursued.

The selected miniature sensor design is based on a phenomenon known as the Hall effect. This effect, which was discovered by Edwin Hall in 1879, occurs when a current-carrying conductor is placed in a magnetic field, resulting in the generation of a voltage in a direction perpendicular to both the current and magnetic field [46]. The resulting voltage, known as the Hall voltage, is directly proportional to the strength of the magnetic field ($V_H \propto E$).

Hall effect sensors produce a voltage proportional to the strength and polarity of a magnet's magnetic field. In general, the magnitude of the voltage generated varies with the sensor's proximity to a magnetic pole. There are several different possible Hall effect sensor and magnet configurations that yield various voltage-proximity curves. In position sensing, one wishes to maximize the linearity between the sensor's output and the actual position. The linearity of the Hall effect sensor was found to be maximized by placing the sensing face of the sensor perpendicular to the long side of a bar magnet that is magnetized along its length. The linear range of the installed version of this sensor set up is discussed in section 4.2.2 of chapter 4.

In order to minimize the overall size of the robot joint, the position sensor was designed to fit within the joint's compartment housing. The Hall effect sensor itself was attached directly to one of the racks, while the rectangular bar magnet was press fitted into a slot in the upper housing. Done in this way the sensor moves with the rack and the magnet stays stationary. An illustration of the sensor and magnet inside the joint is shown in Figure 3.3.1.

Since the Hall effect sensor is attached to the rack, it is the linear position of the rack that is measured and not the actual rotation of the joint. However, the instantaneous joint angle can be estimated from the rack position using Equation 3.4.1 from above. This is an estimate since the gear mechanism introduces errors in practice.

CHAPTER 4

SYSTEM MODELING

4.1 Introduction

Although one can control a hydraulic servo positioning system with simple linear PID control, more accurate positional control is possible by employing a model-based controller. In order to successfully implement a model-based controller, the dynamics of the system must be modeled. While low-pressure hydraulic systems do not suffer from the complications found in pneumatic systems such as, fluid compressibility and internal energy changes within the fluid, the higher fluid density results in increased inlet pressure losses and larger viscous friction losses. It is very important to model these losses accurately in order to achieve high controller tracking performance.

In the first part of this chapter the entire hydraulic servo positioning system is described in detail. Next, the calibration procedure and results are given for the pressure sensors and Hall effect position sensor. The derivation of the system's dynamic equation follows, after which, the valve and system force losses are modeled. Finally, the derived model of the system is tested against the real system to determine its validity.

4.2 Hydraulic System Hardware

In this section the overall system structure is described. In addition, the sensor calibration procedure and results for the pressure sensors and Hall effect position sensor are described, along with an evaluation of the noise generated by each sensor.

4.2.1 System Structure

A schematic representation of the hydraulic servo system is shown in Figure 4.2.1.

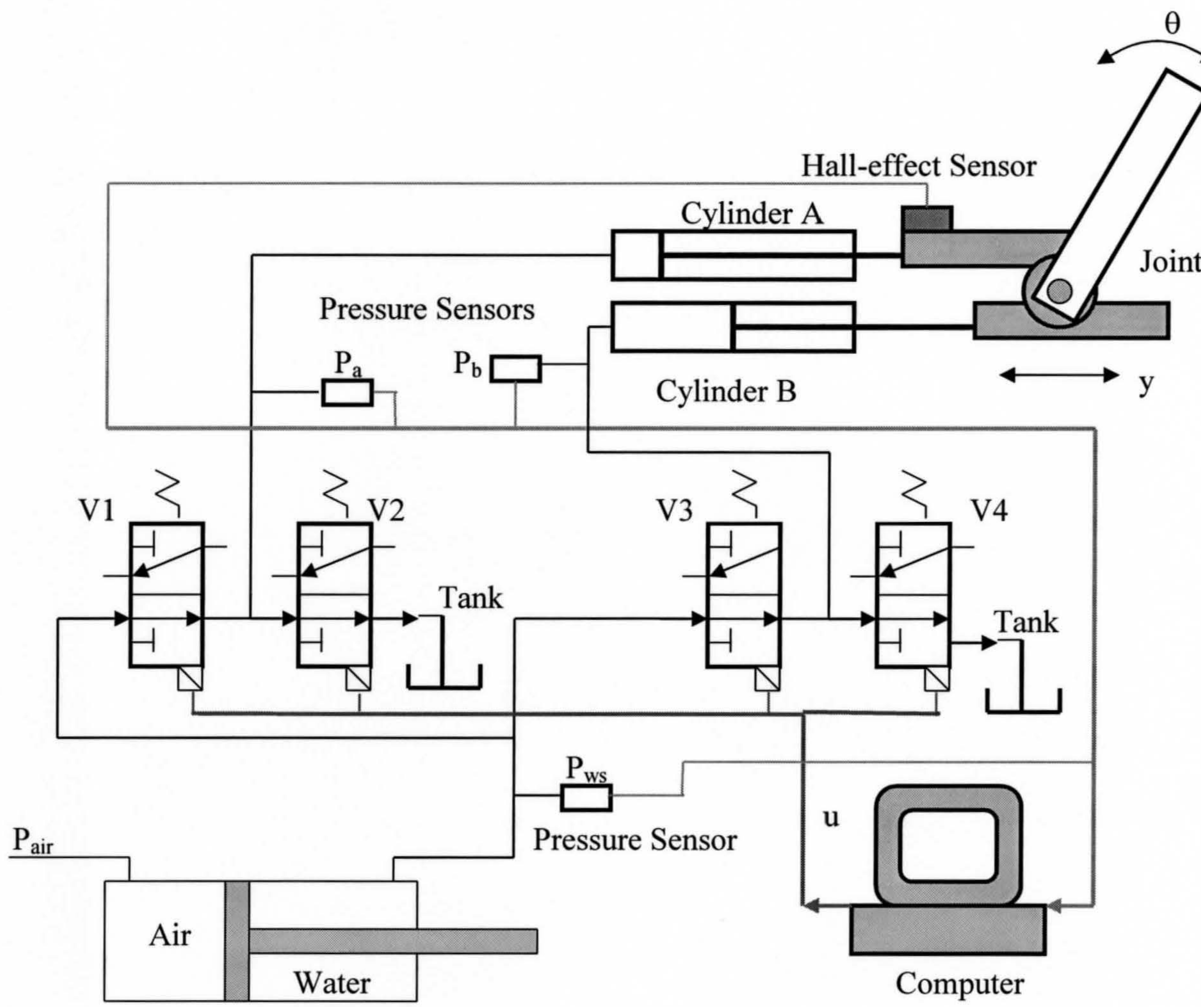

Figure 4.2.1: Hydraulic servo positioning system hardware.

In order to control the flow of water to the two miniature cylinders, four 3/2, on/off solenoid valves were used. Ideally for increased control, one would use valves in which the flow rate is proportional to the voltage supplied. However, miniature proportional valves of the appropriate size were not commercially available. In order to change the solenoid valves to a 2/2 type, the normally open discharge port of each valve was plugged. This converted the valves to a normally closed configuration. Valves 1 and 3 (V1 and V3) are used to supply cylinders A and B with water respectively, while valves 2 and 4 (V2 and V4) are used to discharge water from the cylinders into a reservoir tank. Since the water is virtually an incompressible fluid, the joint will not move unless a pair of opposing valves is open. Therefore, the bi-directional joint can rotate in one direction if V1 and V4 are turned on while V2 and V3 are in the off state. Rotation in the opposite direction occurs if V2 and V3 are turned on while V1 and V4 are in the off state.

Three gauge pressure sensors are installed in the system. P_{ws} is the pressure measurement of the water supplied to the system. This measurement was used when modeling the system force losses and for control. The measurements P_a and P_b from the other two pressure sensors are used to estimate the pressures inside the chambers of cylinder A and B respectively. While the chambers' pressure measurements were not used in the positional control of the joint, the sensors were installed in case force/pressure control is ever desired in the future.

The water used by the hydraulic joint is pressurized using an "air over water" system. In this system, air is supplied at a constant pressure to the rodless side of a cylinder with a 40 mm bore diameter and 100 mm stroke. As the incoming air pushes on the piston head, the water, which is stored in the rodded end of the cylinder, is pressurized. Since the piston face on the rod side has a smaller area, the pressure of the water is amplified with respect to the air supply pressure. The pressure amplification for the supply system was found to be: $P_{water} = 1.19 \times P_{air}$. Since, the maximum supply pressure of the air is 620 kPa, the maximum water pressure that can be supplied to the system is 738 kPa.

The valves and sensors are connected to a National Instruments DAQmx I/O board that communicates with a standard PC. For all calibration and control experiments the sensors sampling period was 1 ms. Between the valves and the DAQmx board is a digital-to-digital converter that converts the 5V low-current digital signal from the computer into a 24V high-current signal that is sent to the valves. Further explanation into the use of the converter is given in section 4.4. The controller code is written in C language; and compiled and run in the National Instruments LabWindows environment.

Photographs of the fully assembled robot joint carrying a 6.5 g mass and of the entire hydraulic servo positioning system are shown in Figures 4.2.2 and 4.2.3 respectively.

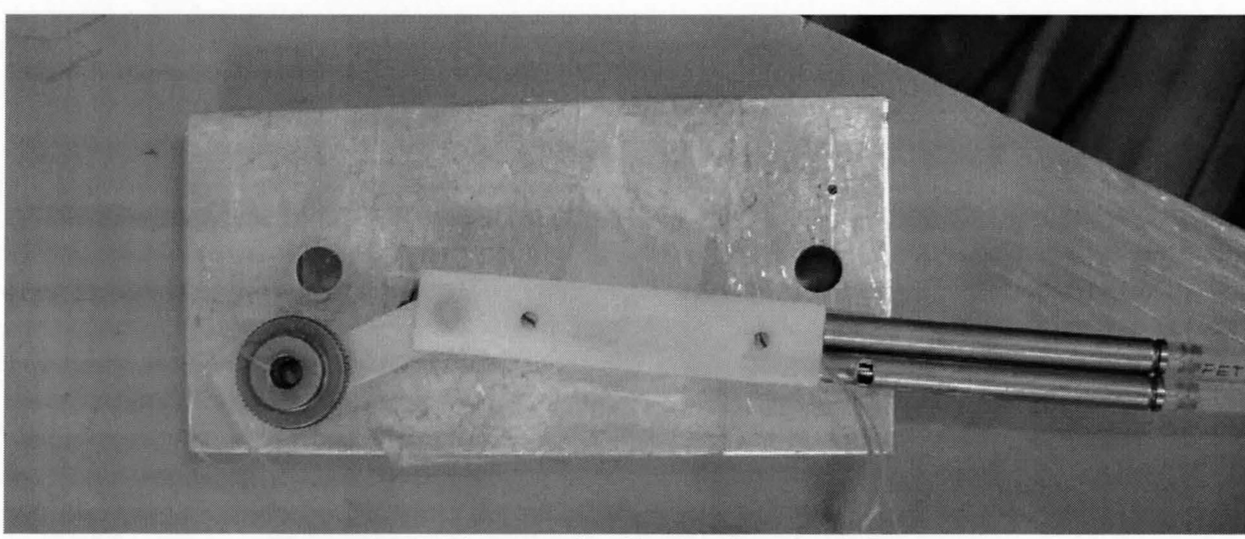

Figure 4.2.2: Photograph of hydraulic robot joint

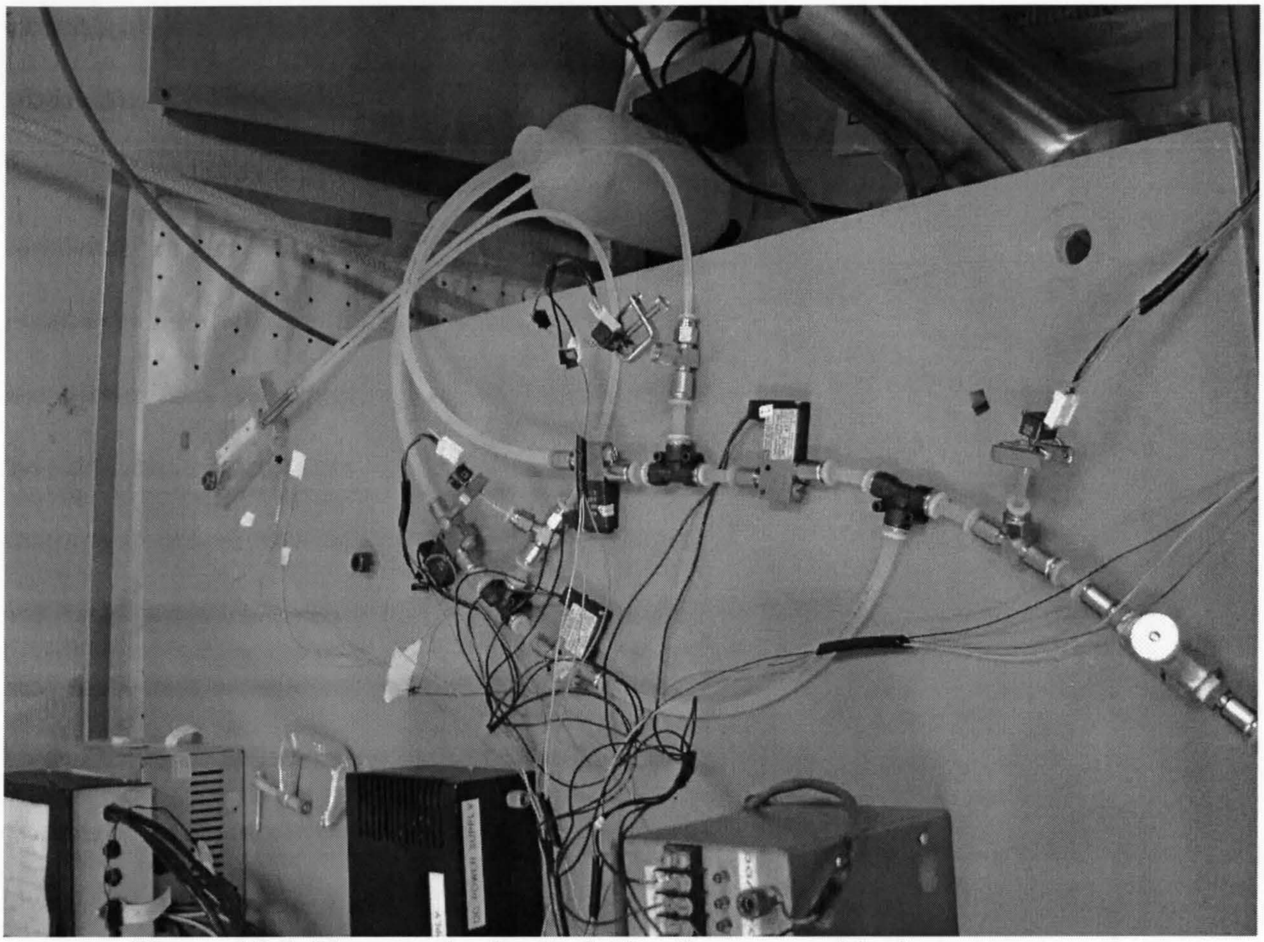

Figure 4.2.3: Photograph of entire hydraulic servo positioning system

4.2.2 Calibration of Sensors

The Hall effect position sensor was calibrated after first fully assembling the joint. The angular position of the joint was modified manually by pushing on the end of one of the racks. To obtain the various angles the joint was rotated both clockwise and counter-clockwise in order to average out the effect of any gear backlash on the sensor measurement. At every location the voltage was read by the DAQmx board and stored in the computer. The true angle of the joint was measured using a protractor. Since both the Hall effect sensor and DAQmx board generate a certain level of noise, 1000 data points were taken and averaged for each angular position. Overall, 15 different angles, spanning the entire range of the joint were measured. Their results are shown in Table 4.2.1 and the resulting calibration curve is plotted in Figure 4.2.4. Since the resolution of the protractor was 1^{o} the angular measurements shown in Table 4.2.1 are accurate to within $\pm$ 0.5^{o}. Therefore, the accuracy of the calibration equation 4.2.1 used to produce the plots in degrees in the remainder of this thesis is limited to $\pm$ 0.5 degrees.

Table 4.2.1: Calibration data for Hall effect position sensor.

Angular position (deg)	**Hall effect sensor reading (V)**
3	3.866
24	3.793
53	3.408
55	3.378
66	3.244
69	3.215
94	2.866
97	2.828
106	2.711
125	2.510
126	2.494
138	2.320
156	2.047
174	1.706
176	1.671

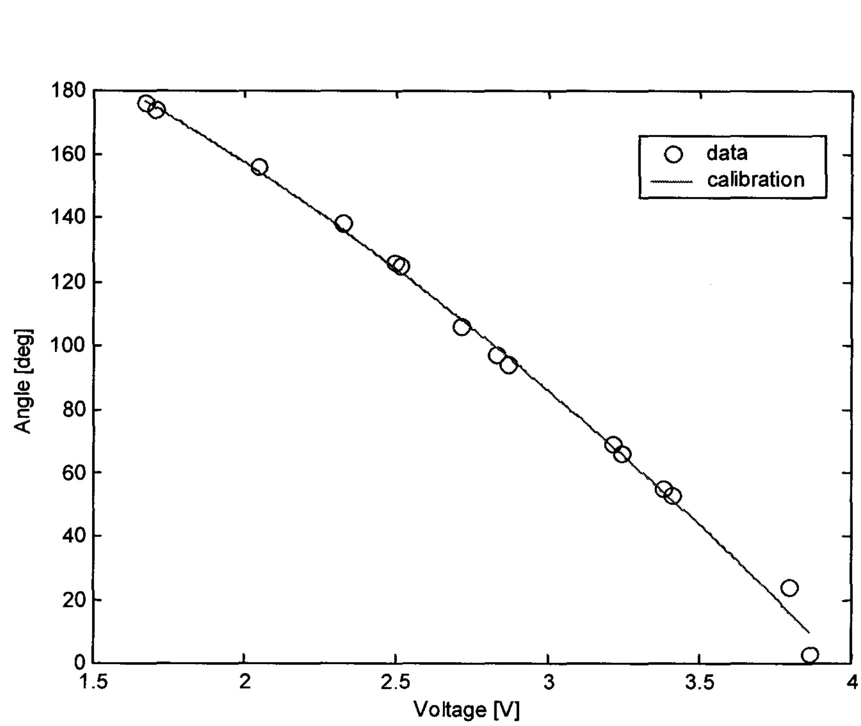

Figure 4.2.4: Calibration curve for Hall effect positional sensor.

From the measurements it was found that the output of the Hall effect sensor was linear between angles 20° and 160°. In order to increase the accuracy of the sensor measurement across the entire motion range of the joint a 2nd order polynomial curve was used to fit the data. The resulting calibration curve equation for the sensor is given by:

$$\theta = -9.122x^2 - 25.58x + 244.94 \tag{4.2.1}$$

where θ and x are the joint angle and sensor voltage respectively.

The pressure sensors used in the system are designed to give a linear output over a pressure range of 0 psig to 100 psig. The three pressure sensors were calibrated by connecting them to an adjustable air supply. The air supply system consists of a pressurized line, which provides air at 90 psig, and an accumulator with a manual regulator. The air pressure was varied from 0 psig to 60 psig and the voltage measurements from the three pressure sensors were simultaneously read into the computer using the DAQmx board. Each of the sensors was found to give a linear output response. The calibration lines for the three sensors are as follows:

$$P_a = 167.65x - 96.526 \tag{4.2.2}$$

$$P_b = 167.13x - 95.364 \tag{4.2.3}$$

$$P_{ws} = 167.38x - 95.845 \tag{4.2.4}$$

where P_a, P_b, P_{ws} are the pressures in kPa and x is the measured sensor voltage. The calibration line for P_a is plotted in Figure 4.2.5.

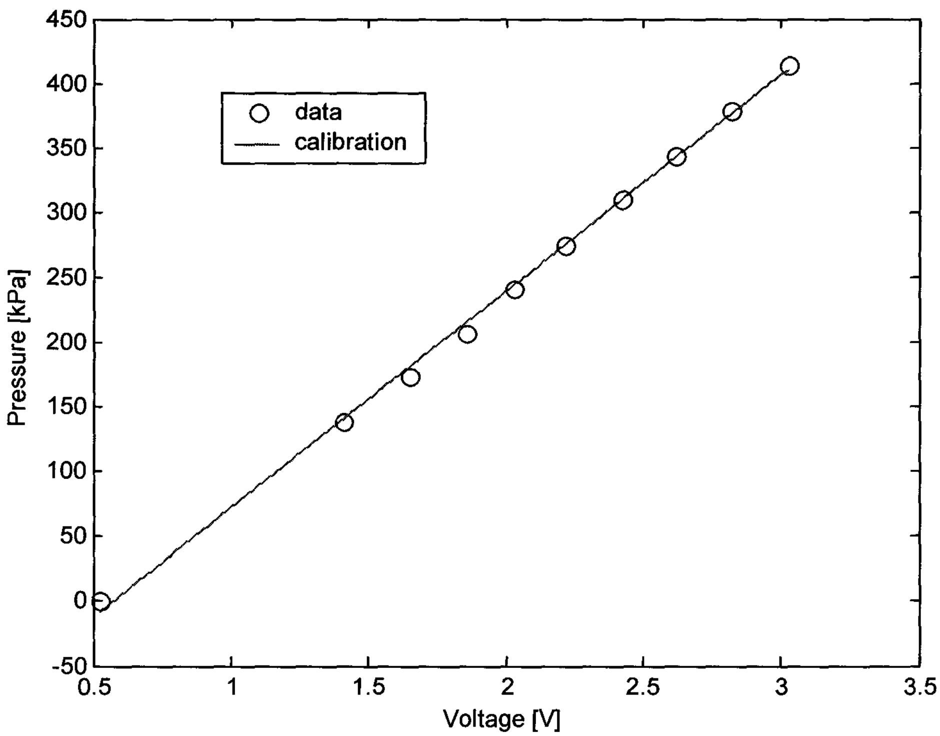

Figure 4.2.5: Calibration line for pressure sensor reading P_a.

4.2.3 Sensor Noise

All electrical devices generate some degree of noise. A very noisy signal can deteriorate the accuracy of a sensor measurement to the point where it is no longer useful. In order to ensure the quality of a sensor's signal, the magnitude and frequency spectrum of the sensor noise must be examined and the appropriate filtering applied if necessary. Examples of the measurements and noise spectrums for the Hall effect sensor and pressure sensor P_a are shown in Figures 4.2.6 and 4.2.7 respectively.

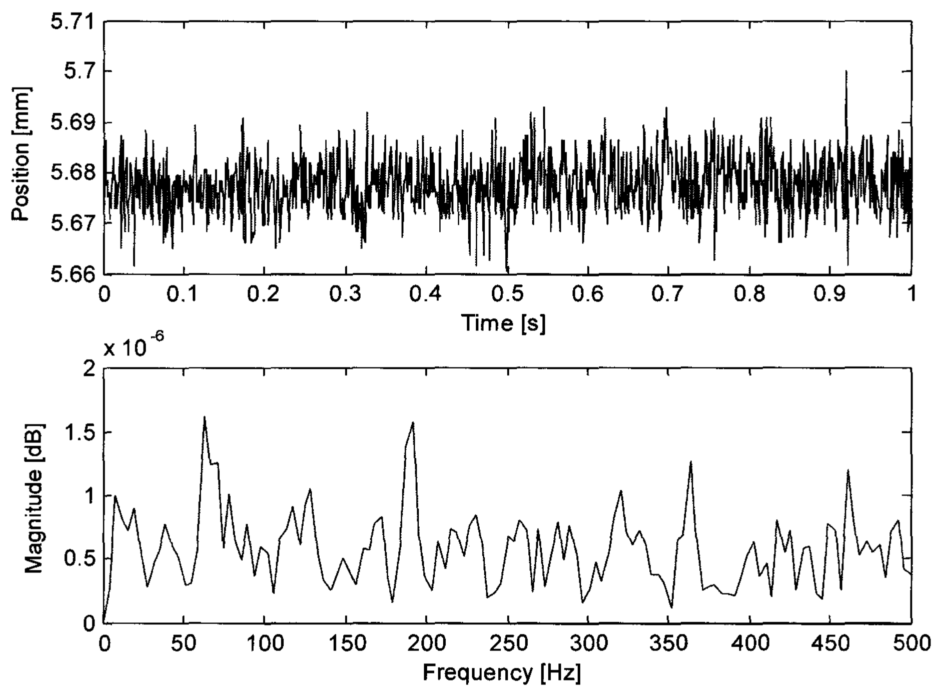

Figure 4.2.6: Hall sensor position measurement and noise spectrum.

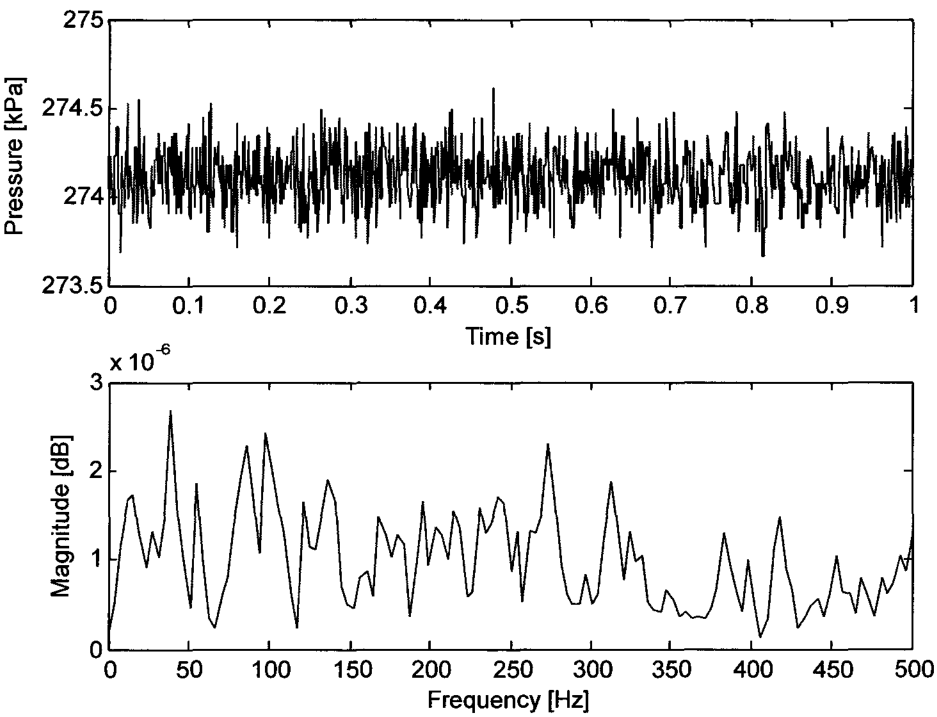

Figure 4.2.7: Sensor P_a pressure measurement and noise spectrum.

It was found that the measurement from the Hall effect sensor contained ± 0.02 mm (± 0.24°) of noise and the measurement from the pressure sensors contained ± 0.4 kPa of noise. Also, from the noise spectrums in Figures 4.2.6 and 4.2.7 it can be seen that both types of sensors appear to generate white noise, with the magnitude being relatively constant across all frequencies. Since the magnitude of the noise is small and there exists no obvious cut off frequency, it was deemed unnecessary to apply an analog or digital filter when implementing the control strategies.

4.3 Derivation of System Dynamics Equation

In this section the dynamic equation for the hydraulic servo positioning system is derived. The system consists of several key elements. The dynamics of each element is examined separately and then combined to create the overall dynamic equation of the system.

The water is the most important element in the system as it is the working fluid and its dynamics are ultimately responsible for the actuation of the joint. Due to its relatively high density (998 kg/m^3 @ 20^{o}C) compared to air, water is often thought of as an incompressible fluid. While this is not exactly accurate, water is highly incompressible, as quantified by its large bulk modulus (β) value of 2.19 x 10^9 N/m^2 [47]. In order to determine if the water inside the servo positioning system can be treated as incompressible its percentage change in volume must be found for the known operating pressure of the system. Since the water pressure must not exceed 700 kPa (the maximum rated pressure of the miniature pneumatic cylinders) the maximum percentage volume change of the water (assuming no air in the system) can be found as,

$$\frac{dV}{V} = \frac{P_{ws}}{\beta} = \frac{700{,}000 N/m^2}{2.19x10^9 N/m^2} = 0.00032 = 0.032\% \tag{4.3.1}$$

Although theoretically the percentage volume change of the water is very small, in practice there will always be some air trapped in the system. This acts to decrease the effective bulk modulus of the water. However, for the purposes of modeling the system for control it is assumed that no air is present and therefore the volumetric flow rate of the water is constant throughout the entire system.

The dynamic behaviour of the hydraulic joint can be described by,

$$P_a A - P_b A - f = m\ddot{y} \tag{4.3.2}$$

where P_a and P_b are the chamber pressures inside cylinders A and B, A is the bore area of cylinders A and B, f is the friction losses caused by the joint gears and cylinders' pistons and seals, m is the moving mass of the joint, and $\ddot{y}$ is the linear acceleration of the rack. The moving mass of the joint is the total mass of all moving parts with the joint structure. This includes the mass of the two racks, the pinion gear, the spur gear, the two cylinder rods and piston heads, the Hall effect sensor, and the second link.

Valves are used to control the flow of a fluid through a hydraulic or pneumatic circuit and are typically the most significant source of resistance to the flow. In practice, the fluid flow resistance of a valve is geometry dependant and results in nonlinear relationships between the pressure drop across the valve and the flow rate. However, as a simplification the valve can be modeled as an ideal fluid resistor [48] given by,

$$\Delta P = RQ \tag{4.3.3}$$

where ΔP is the pressure drop across the valve, R is the hydraulic flow resistance of the valve, and Q is the volumetric flow rate of the water.

To complete the dynamic model of the system the various pressure and friction losses must also be considered. Since the pressure losses at the valve have already been considered, the remaining locations of the pressure losses in the system are the cylinder inlet ports, and the tubing connectors, which include t-connectors and elbows. The friction losses in the system are made up of the viscous friction between the water and tubing walls, the friction between the cylinder seals and piston, and the friction within the joint's gear mechanism. Instead of trying to model each of these losses individually, a more practical solution is to lump them together and measure their combined effects experimentally. The modeling of the combined system force losses is presented in detail in section 4.5.

With the dynamics of all the elements identified, the dynamic equation for the entire hydraulic system can now be derived. Applying Newton's second law over the entire system, the effect of the pressure drop across the valves can be added to the dynamics of the hydraulic joint given previously in equation 4.3.2. For the case when valves 1 and 4 are open this gives,

$$(P_{ws} - \Delta P_1)A - \Delta P_4 A - F_l = M\ddot{y} \tag{4.3.4}$$

where P_{ws} is the gauge pressure of the water supply, ΔP_1 and ΔP_4 are the pressure drops across valves 1 and 4, A is the bore area of the miniature pneumatic cylinders, F_l is the total friction and pressure losses inside the system, M is the moving mass of the joint plus the mass of the water, and $\ddot{y}$ is the linear acceleration of the racks. Substituting equation 4.3.3 in for ΔP_1 and ΔP_4 gives,

$$(P_{ws} - R_1 Q_1)A - R_4 Q_4 A - F_l = M\ddot{y} \tag{4.3.5}$$

Noting that since the water is assumed incompressible, $Q_1 = Q_4 = \dot{y}A$, and rearranging equation 4.3.5 gives,

$$P_{ws}A - (R_1 + R_4)\dot{y}A^2 - F_l = M\ddot{y} \tag{4.3.6}$$

where $\dot{y}$ is the linear velocity of the racks. Equation 4.3.6 states that the acceleration force of the joint is equal to the force generated by the pressurized water supply minus the forces required to maintain the flow through the valves and overcome the friction and pressure losses in the system. For motion in the opposite direction equation 4.3.6 can be applied by simply replacing R_1 and R_4 with R_3 and R_2 respectively.

4.4 Flow Resistance Model of Valves

4.4.1 Valve Selection

As mentioned in the previous section, the rotational control of the hydraulic joint is ultimately achieved by controlling the volume flow rate of the water through the system. Ideally, proportional valves in which the flow rate is proportional to the voltage supplied to the valve would be used. However, miniature proportional valves compatible with water are difficult to find and highly expensive. A less expensive and more readily available solution is to use small on/off pneumatic solenoid valves whose stainless steel structure and relatively large orifice diameter make them suitable candidates for use with water. It was observed that the smaller orifice diameters found in comparable pneumatic proportional valves, when combined with the high viscosity of water, lead to large pressure drops and unsteady flow conditions. A plot of an experimental flow rate test using a small proportional pneumatic poppet valve is shown in Figure 4.4.1. In the test the valve orifice was set to its fully open position and the water supply pressure was set to 60 psi (414 kPa). As the flow rate increased, a large pressure drop occurred inside the valve causing it to prematurely close. As can be seen from Figure 4.4.1, the continuous opening and closing of the valve resulted in unsteady water flow.

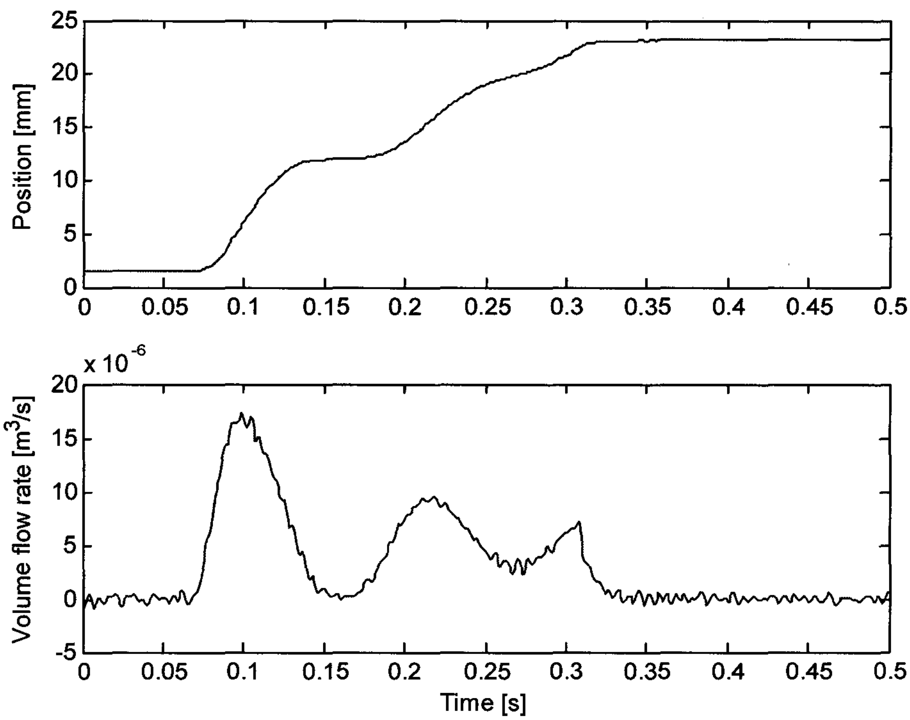

Figure 4.4.1: Flow rate of water through proportional poppet valve.

4.4.2 Description of Control Signal Sent to Valves

As outlined by equation 4.3.6 in the previous section, in order to control the dynamic response of the hydraulic joint one must be able to control the flow resistance of the valves. In a proportional valve the flow resistance is a function of the voltage supplied to the valve. An on/off solenoid valve can be made to approximate the behaviour of a proportional valve by pulse-width-modulating (PWM) the voltage to the valve. As mentioned in chapter 2, the PWM technique involves quickly switching the valve between the on and off states. The time period in which the valve goes through one on/off cycle is referred to as the PWM period [39]. The opening and closing time delay for the solenoid valve is 5 ms and 2 ms respectively. Therefore, the valve requires a minimum 7 ms to complete one on/off cycle. A PWM period of 16 ms was selected in an effort to balance the opposing requirements for fast response and high signal resolution.

In the PWM technique, the valve is commanded to be in the "on" state for a percentage of the PWM period. This commanded percentage is known as the valve's duty cycle. To illustrate how the control signal works in practice, consider a commanded duty cycle of 50 %. In this case, the valve would be commanded to turn on for the first 8 ms and then to turn off for the remaining 8 ms. Since each valve required a supply voltage of 24 V, the voltage was not sent directly from the computer. Instead, a digital on/off signal (5 V or 0 V) was sent from the computer to the digital-to-digital converter that converted the computer signal into an appropriate supply voltage (24 V or 0 V) that was sent to the valves.

In order to avoid generating large pressure pulsations within the system, only the signal to the discharge valve (V2 or V4), where the pressure is close to that of atmospheric, was pulse-width-modulated. The valve supplying water to the other cylinder (V1 or V3) was kept on during the entire PWM period. For example, looking at Figure 4.2.1 if one wanted to extend cylinder rod A, and thereby retract cylinder rod B, V1 would be turned on and V4 would received the desired duty cycle. Given this signal strategy the dynamic equation of the system becomes,

$$P_{ws}A - \left[R_1 + R_4(u)\right]\dot{y}A^2 - F_l = M\ddot{y} \tag{4.4.1}$$

where u is the duty cycle signal from the controller. Hence, to control the hydraulic joint it is first necessary to model the change in the discharge valve's flow resistance as a function of the duty cycle.

4.4.3 Derivation of Valve Model

Experiments were conducted to capture the volumetric flow rate of the water through the valve for different combinations of pressure drop and PWM duty cycle. This data was then used to model the valve. The experimental set up is shown in Figure 4.4.2.

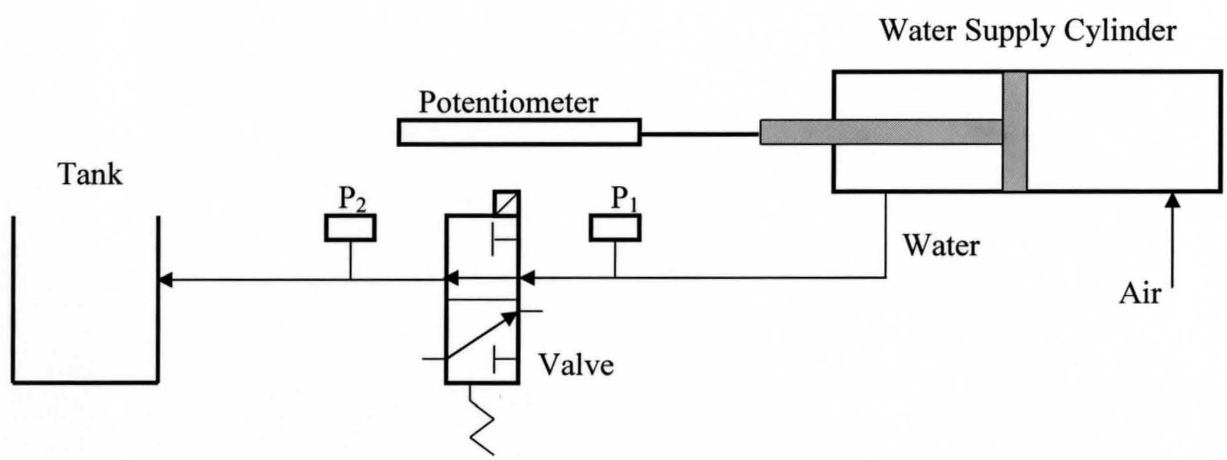

Figure 4.4.2: Experimental set up for valve modelling.

Two pressure sensors were placed on either side of the valve in order to measure the pressure drop ($P_1 - P_2$) across the valve. The pressure drop was varied by manually adjusting the supplied water pressure via the air supply's dial gauge. The discharge side of the valve was open to atmosphere and the water was discharged into an open tank. The volume flow rate of the water was measured in the following manner. First, the position of the supply cylinder's piston rod was measured through the use of a linear potentiometer attached to the end of the piston rod. The velocity of the piston rod was then estimated by applying the central difference method to the recorded position measurements. Finally, the volume flow rate of the water was calculated by multiplying the velocity by the area of the piston face inside the water chamber. Several different pressure drop values were tested for each of the ten different PWM duty cycles. A plot from one of the tests is shown in Figure 4.4.3. The duty cycle and water supply pressure values for the test were 70 % and 290 kPa respectively.

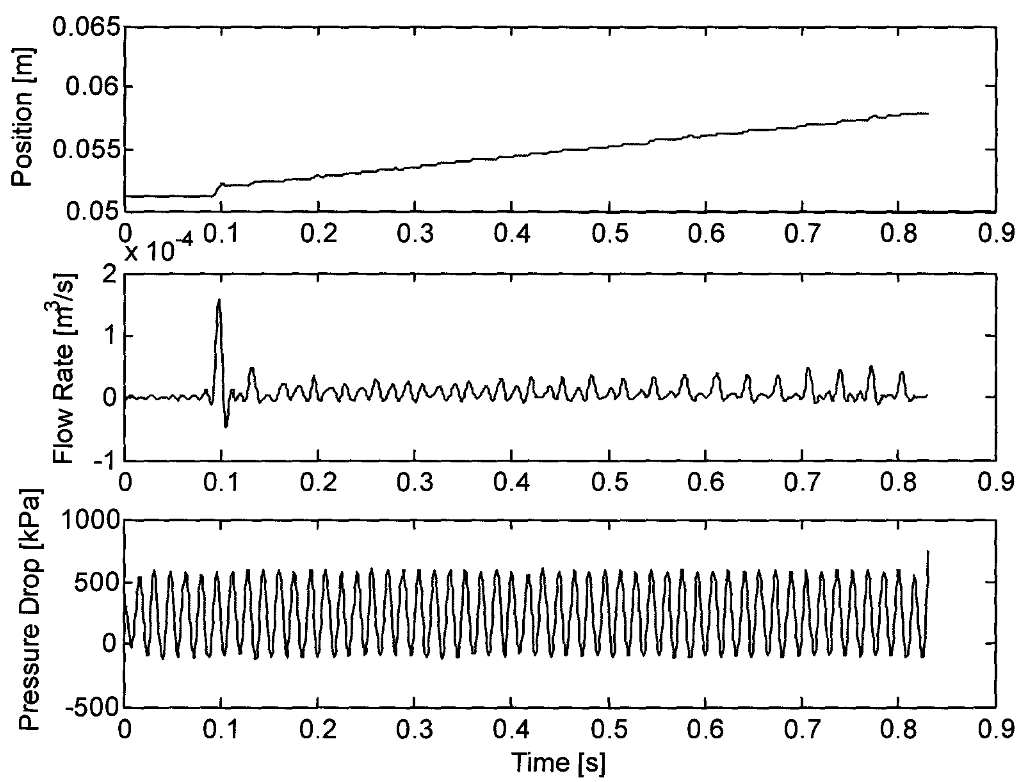

Figure 4.4.3: Valve volumetric flow rate test.

From Figure 4.4.3 it can be seen that during the initial motion of the piston rod the volume flow rate spikes. This is due to the stick-slip phenomenon present between the piston rod and the cylinder seals. After this point, the flow rate continues to oscillate, although at a small magnitude, due to the pressure pulsations generated by the PWM signal. Despite the presence of the oscillations, the positional movement of the piston rod is relatively smooth. Due to the linearity of the positional measurement, the flow rate data was converted into an average value for the entire motion range occurring after the stick-slip zone. The average pressure drop across the valve was also found over this range. Therefore, each test resulted in one data point.

Upon completion of the tests, the data points corresponding to each PWM duty cycle were plotted onto separate graphs, resulting in a flow rate versus pressure drop curve for each duty cycle. Two of the generated curves are shown in Figures 4.4.4 and 4.4.5 respectively.

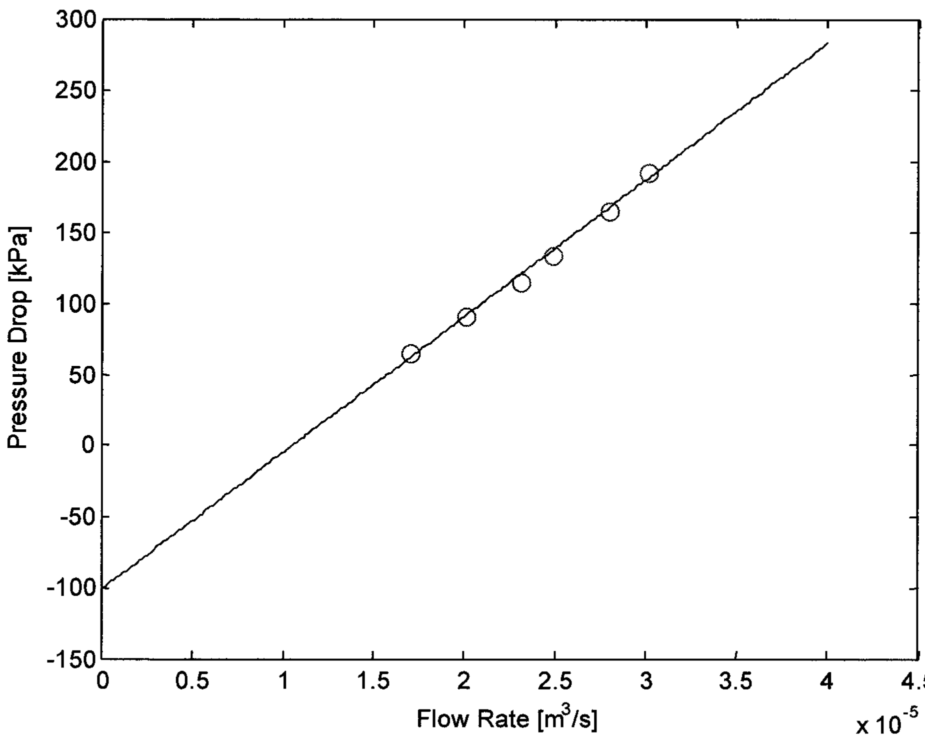

Figure 4.4.4: Pressure drop versus flow rate curve (duty cycle = 100 %).

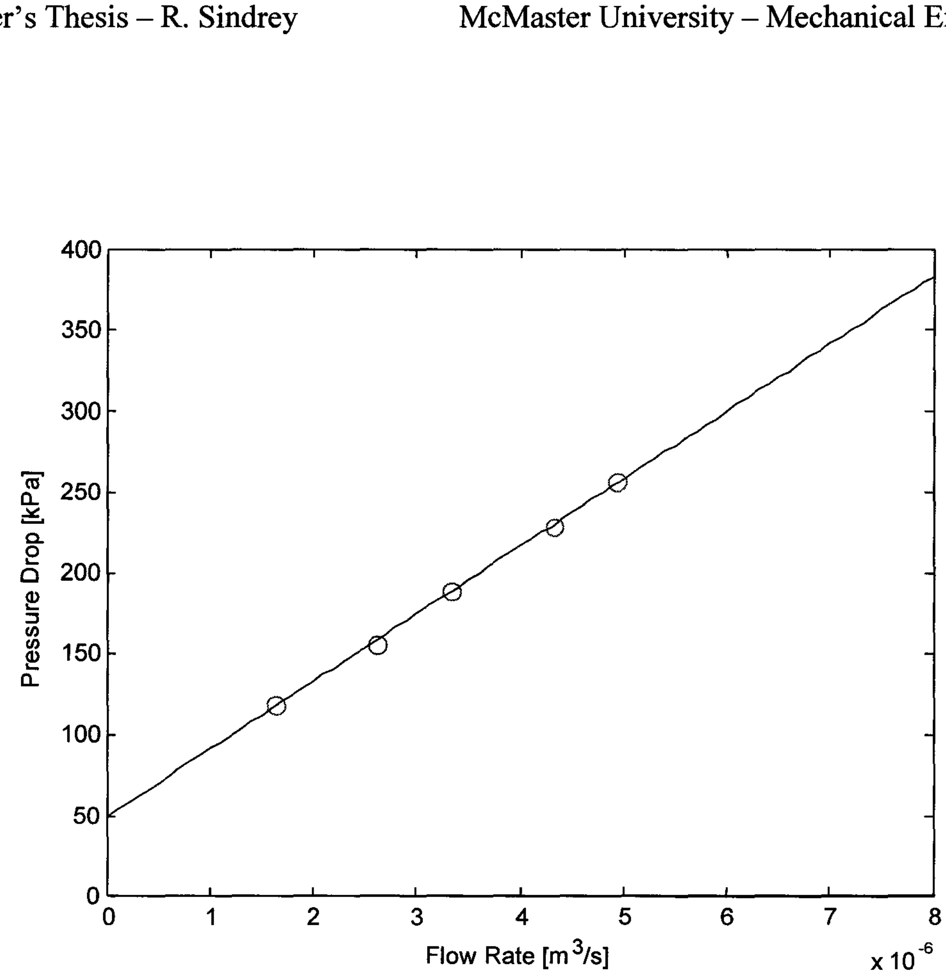

Figure 4.4.5: Pressure drop versus flow rate curve (duty cycle = 42 %).

It can be seen from Figures 4.4.4 and 4.4.5 that the relationship between the pressure drop across the valve and the volume flow rate of the water is linear for the range that could be measured with the experimental set up. However, since the lines do not intersect at (0,0) there is obviously uncaptured nonlinear dynamics between the lowest measured flow rate and zero on each graph. Therefore, the linear model is only valid for the flow rates measured.

In order to relate the duty cycle to the valve's flow resistance the magnitude of the valve's flow resistance for each duty cycle was found by simply calculating the slope of each line. The plot of the valve flow resistance versus the PWM duty cycle is shown in Figure 4.4.6. The resulting valve equation from curve fitting the data is given by,

$$R = (1.8372x10^{14})d^{-2.1706} \qquad (4.4.2)$$

where R is the flow resistance of the valve in kPa/m^3/s and d is the PWM duty cycle. The R-squared value of the curve-fit to the data was 0.986.

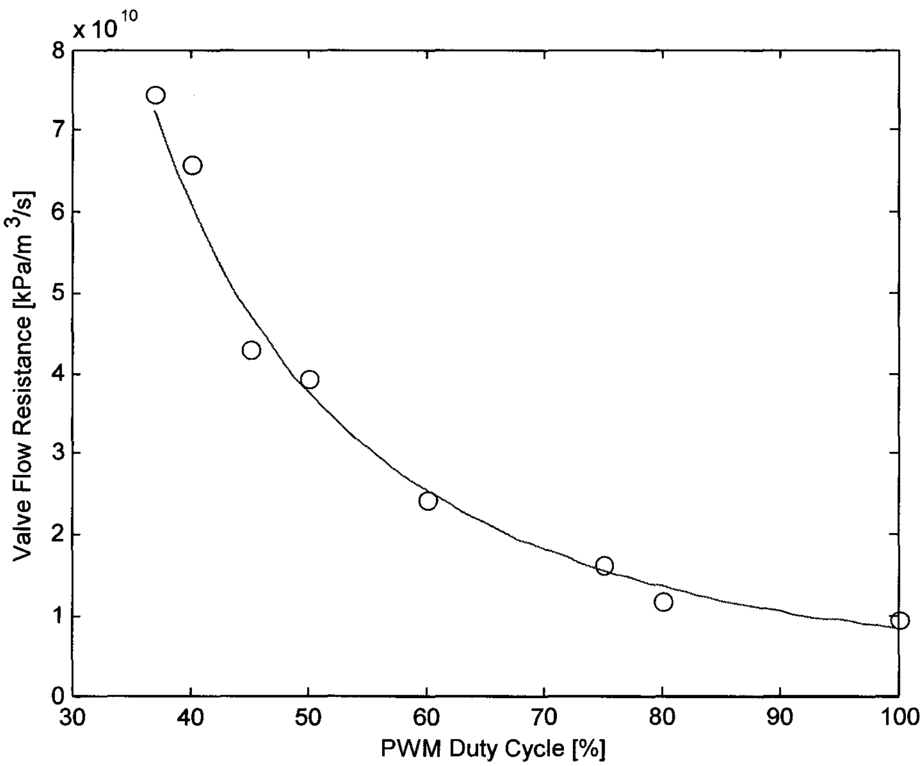

Figure 4.4.6: Valve flow resistance versus PWM duty cycle.

4.5 Model of Force Losses in System

In this section an explanation of how the system force losses were estimated is given, along with the procedure for modelling the velocity and position dependant force loss elements.

4.5.1 Estimation of Force Losses

An important element to any mechanical servo system model is the friction effects within the system. As mentioned in section 4.3, all of the hydraulic servo system's friction and pressure losses were grouped together and considered as one system-wide force loss. The overall force loss of the system was estimated through experimentation. In each experiment the water supply pressure was manually set and the joint was rotated from rest in either the clockwise or counter-clockwise direction by opening the appropriate pair of valves. The water supply pressure (P_{ws}) and the rack position (y) were measured and the velocity and acceleration of the racks were estimated by applying the central difference method to the position signal. The system force loss was then calculated by rearranging equation 4.3.6 to give,

$$F_l = P_{ws}A - (R_1 + R_4)\dot{y}A^2 - M\ddot{y} \tag{4.5.1}$$

where R_1 and R_4 represent the flow resistances of one pair of valves. Both the supply and discharge valve were given a duty cycle of 100 % in order to avoid oscillations in the pressure, acceleration, and velocity signals, which would have made it difficult to estimate the force loss.

Experiments were conducted for a series of water supply pressures ranging from 245 kPa to 575 kPa. Both clockwise (CW) and counter-clockwise (CCW) rotations were tested for each supply pressure. A plot from one of the experiments showing the rack position, velocity, acceleration, and estimated system force loss is shown in Figure 4.5.1.

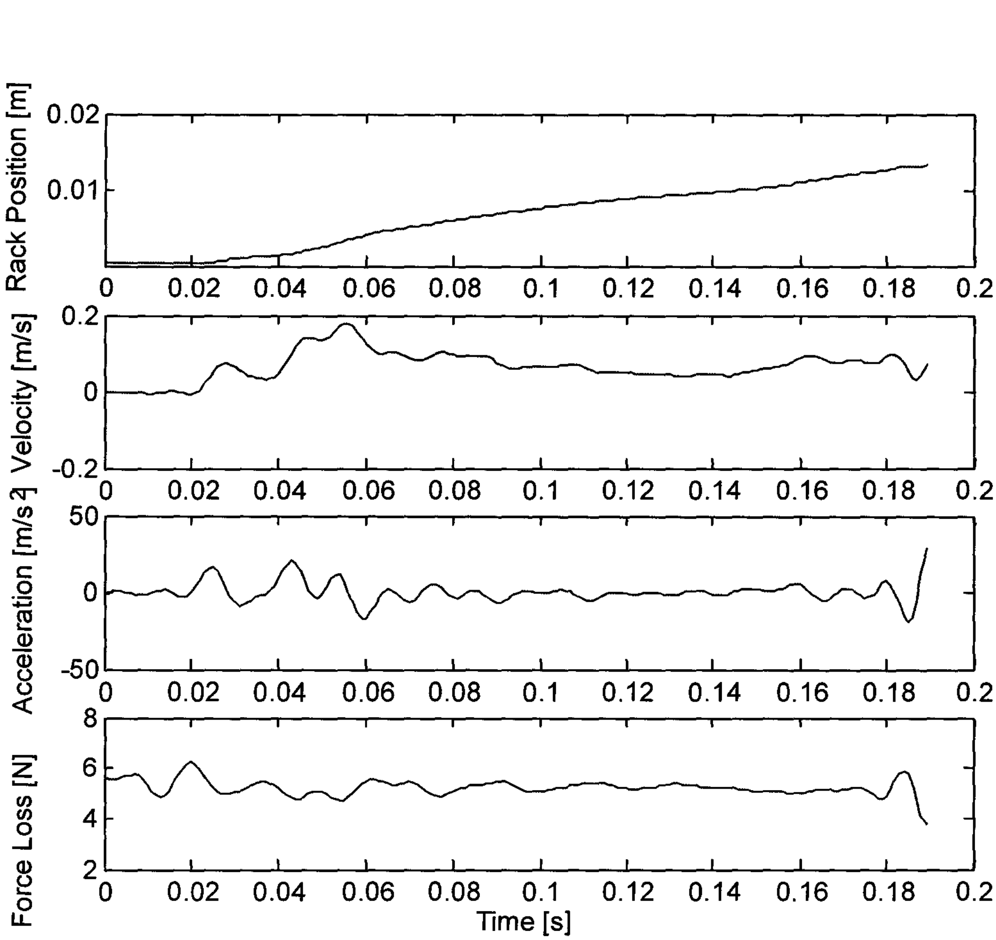

Figure 4.5.1: Plot of data from system force loss experiment (P_{ws} = 490 kPa).

Several key observations can be made from Figure 4.5.1. First, the force loss, acceleration, and velocity all settle to approximate constant values. Second, in examining the magnitude of the force loss compared to the water supply pressure, it is clear that the majority of the force generated by the 4 mm diameter cylinders is used to overcome friction and pressure losses. Hence, the main dynamic element in the system is the force loss. The valve resistance and mass acceleration force are significantly less than the force loss due to the small bore area of the miniature cylinders and the small moving mass of the system. Finally, the oscillations present in the force loss during the first 20 ms, when the joint has not yet begun to move, are caused by the oscillations in the water pressure when the valves first open.

4.5.2 Velocity Dependant Force Loss

As a simplification it was assumed that the force losses within the system could be modeled by the classic friction model. Friction is typically a nonlinear function of the velocity between two contacting surfaces. The classic friction model is given as,

$$F_f = \begin{cases} \left[F_c + (F_s - F_c)e^{-(v/v_s)^2}\right]\operatorname{sgn}(v) + F_v v & \textit{if } v \neq 0 \\ F_{ext} & v = 0 \textit{ and } |F_{ext}| < F_s \\ F_s \operatorname{sgn}(F_{ext}) & \textit{otherwise} \end{cases} \qquad (4.5.2)$$

where sgn(v) is signum function of the velocity,

$$\operatorname{sgn}(v) = \begin{cases} 1 & \textit{if } v > 0 \\ 0 & \textit{if } v = 0 \\ -1 & \textit{if } v < 0 \end{cases} \qquad (4.5.3)$$

In the above model, F_c is the kinetic Coulomb friction force, F_s is the stiction force, F_v is the viscous friction force, F_{ext} is the externally applied force, v is the velocity, and v_s is the Stribeck velocity. From the first part of equation 4.5.2, one can see that the moving friction is made up of Coulomb and viscous friction forces. The Stribeck velocity term, commonly referred to as the Stribeck effect, is dominant at very low velocities and is characterized by a large drop-off in the friction force. As the velocity rises, the Stribeck effect diminishes and the friction begins to increase due to the influence of the viscous friction term.

Upon examining the data from the tests it was determined that the Stribeck effect on the system force loss was negligible. This can be seen from Figure 4.5.1 by observing that the magnitude of the force loss decreases only slightly during the transition phase from static to kinetic friction.

By ignoring the Stribeck friction effects, the dominant velocity dependant force loss source is thus the viscous force loss and the total force loss of the hydraulic system can be given as,

$$F_l = F_c \operatorname{sgn}(v) + F_v v \tag{4.5.4}$$

The dominance of the viscous term is not surprising due to the small size of the tubes used in the system and the relatively high dynamic viscosity of water ($\mu = 1 \times 10^{-3}$ N·s/m^2) compared to other fluids like air and liquid methanol [47].

Another important observation that can be made from Figure 4.5.1 is the existence of an apparent inverse relationship between the rack velocity and the force loss. This is counter-intuitive to the directly proportional relationship predicted by the viscous term. The discrepancy can be explained by the presence of positional dependant force loss effects. These effects are a direct result of localized binding in the gear mechanism. At these locations the friction is greater due to the increased contact pressure between the teeth of the pinion and spur gears.

Incorporating the position dependant friction into the model gives,

$$F_l = F_c(y) \operatorname{sgn}(v) + F_v v \tag{4.5.5}$$

The model now consists of a position-dependant Coulomb term and a velocity-dependant viscous term. In order to properly model the force loss, the effect of each of the terms must be separated from the data calculated above.

The viscous term was isolated from the total force loss by noting that the variations in the velocity and force loss data were primarily caused by positional effects. Therefore, if the positional effects were removed the velocity and force loss would have relatively constant values. Based on this logic the average force loss and velocity over the joint's motion range were calculated. Hence, each force loss test produced one force loss versus velocity data point. A plot of all of the calculated force loss versus velocity data points is shown in Figure 4.5.2.

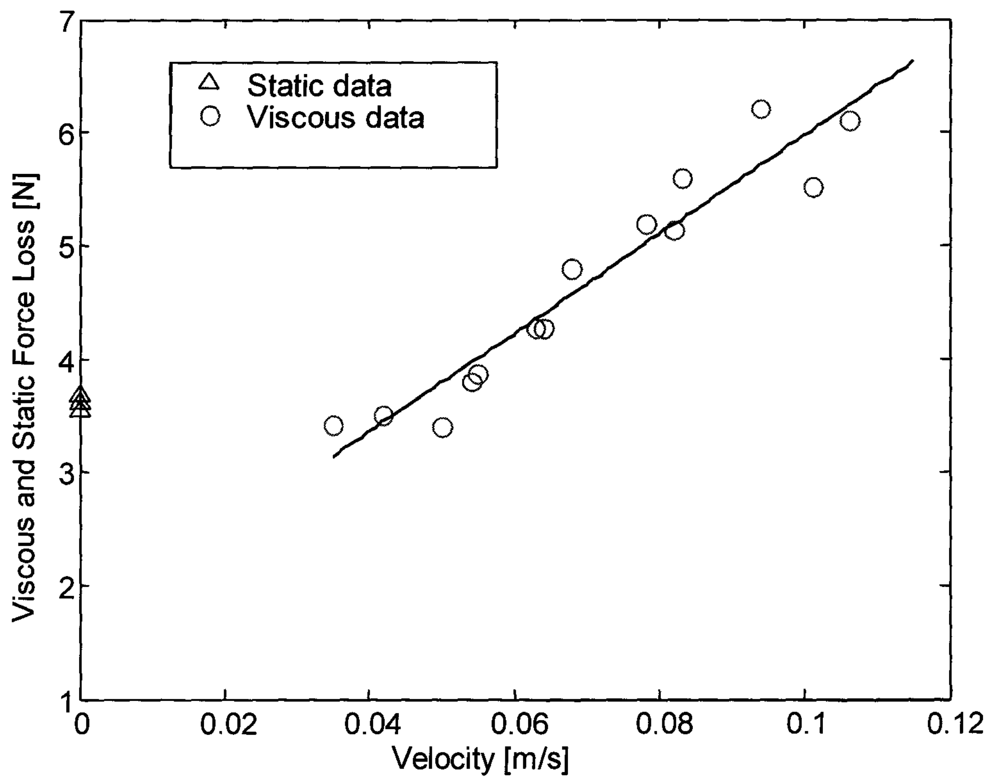

Figure 4.5.2: Plot of viscous and static force loss versus velocity.

Figure 4.5.2 shows that relationship between the viscous force loss and the rack velocity is relatively linear. This is in agreement with the linear proportional relationship predicted by the viscous term in the model equation. From the slope of the line shown in Figure 4.5.2, the viscous coefficient (F_v) was found to be 45.9 N/m/s. The static friction values (i.e. when the velocity equals 0) are also plotted in Figure 4.5.2. The average static friction value of the system was found to be 3.6 N.

4.5.3 Position Dependant Force Loss

With the viscous force loss term now modelled, the position dependant Coulomb force loss can be found as,

$$F_c = F_l - 45.9v \tag{4.5.6}$$

Using equation 4.5.6, the viscous force loss portion was subtracted from each data point for a given test. The Coulomb force loss was found for four sets of force loss data, two from CW tests and two from CCW tests, and used to model the change in Coulomb force loss with position. The resulting Coulomb force loss data plot and curve fit is shown in Figure 4.5.3. As can be seen from the figure, the relationship between the Coulomb force loss and rack position is highly nonlinear and has large uncertainty. An approximate fit to the data was achieved using a sixth order polynomial function given by,

$$\begin{aligned} F_c = &-3.051x10^{14} y^6 + 1.587x10^{13} y^5 - 3.244x10^{11} y^4 + 3.294x10^9 y^3 \\ &-1.727x10^7 y^2 + 4.36x10^4 y - 39.551 \end{aligned} \tag{4.5.7}$$

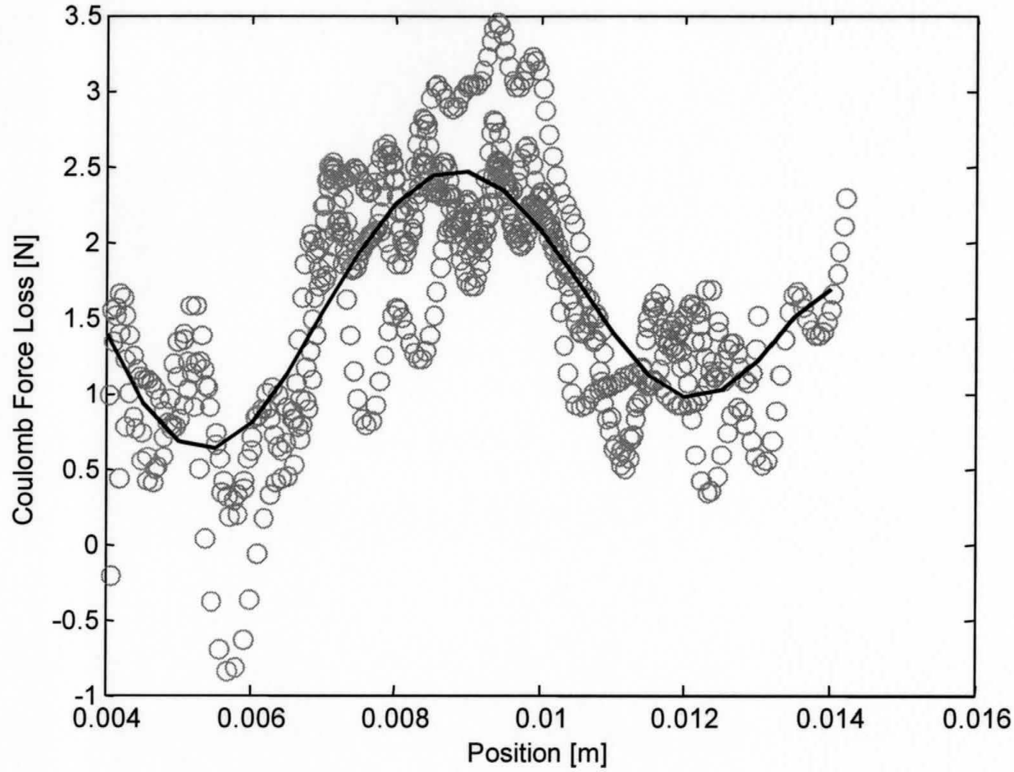

Figure 4.5.3: Coulomb force loss versus rack position.

4.6 Open Loop Validation of Model

Before proceeding with the control of the joint, it is first necessary to determine how well the developed model represents the system's true behaviour. In order to examine the validity of the model an open loop motion test was conducted. In the test the valves were sent a PWM duty cycle, which incremented in a sinusoidal manner after each PWM period. The sinusoid had a duty cycle amplitude of 45 % and a period of 1.6 s. The reason for using a sinusoidal signal was that it allowed the model to be tested for a wide range of PWM duty cycles in a single test. To avoid a hard stop collision between the output link and the joint housing, motion limits were coded into the software. When the joint reached one of the limits, it was commanded to reverse direction.

The joint response from the open loop test was compared to the simulated response of the model using the same input conditions. The simulation was programmed in Matlab and its procedure was as follows:

1) Set y, $\dot{y}$, $\ddot{y}$, and the PWM duty cycle to zero.
2) Calculate F_l using equations 4.5.7 and 4.5.5 respectively.
3) Every 16 ms sinusoidally increment the PWM duty cycle.
4) Calculate the discharge valve's resistance using equation 4.4.2.
5) If the magnitude of the duty cycle is less than 30 %, $\ddot{y}$ equals zero. Otherwise, use equation 4.4.1 to calculate $\ddot{y}$.
6) Use numerical integration to calculate $\dot{y}$ and y.
7) If one of the soft coded limits is reached, stop motion by setting duty cycle to zero, and then switch appropriate signs in equation 4.4.1 to initiate motion in other direction.
8) Repeat steps 2-7 until run time equals 3 seconds.

A plot of the joint's simulated position and real position along with the sinusoidal duty cycle signal used in the experiment is shown in Figure 4.6.1.

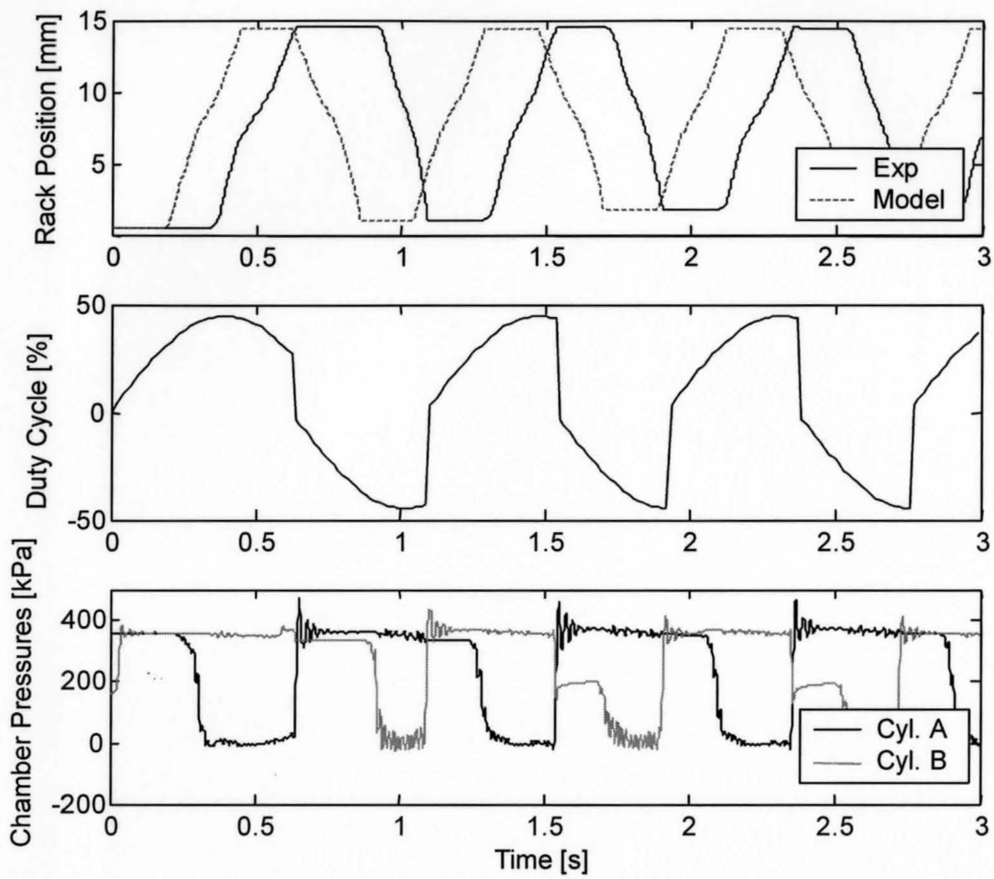

Figure 4.6.1: Comparison of experimental and model responses to sinusoidal duty cycle.

Figure 4.6.1 shows a definite motion time delay between the simulated model response and the actual joint response. In examining the plot of the cylinder chamber pressures in Figure 4.6.1, it can be seen that the initial motion delays in both the CW and CCW directions are a direct result of hydraulic pressure time delays. When one of the valves in the system opens it takes time for the cylinder chamber pressure to equalize with the line pressure it now sees. For instance, when the supply valve opens, the cylinder downstream takes time to see the increase in water pressure. The time required for the pressures to equalize is greater if the valves have been closed for a while, which was the case at the beginning of the open loop test. The hydraulic pressure time delay can be minimized through pre-charging the system by moving the joint from side to side before applying the control algorithms. This is evident by noticing that after the initial CW and CCW motion delays, the motion profiles of the model and joint become similar in shape. Overall, aside from the unmodeled initial pressure dynamics, the derived model appears to be a good representation of the system dynamics.

4.7 Conclusions

In this chapter the hydraulic servo system used to control the joint was described in detail and the dynamic equation for the system was derived. The flow resistance of the on/off solenoid valves with respect to PWM duty cycle was then modeled using experimentally gathered data. Next, the remaining friction and pressure losses in the system were lumped together into one system force loss. The force loss was estimated using experimental data and separated into velocity and position dependant components. Finally, the derived system model was compared against the open loop response of the joint to a sinusoidal PWM duty cycle in order to validate its accuracy. Overall, the model was found to be a good representation of the real system.

CHAPTER 5

CONTROLLER DESIGN AND EXPERIMENTS

5.1 Introduction

In this chapter the design, simulation, and experimental results are presented for three different controllers. The first controller that is examined is a linear position-velocity-acceleration (PVA) control architecture. The results from this controller are used as a baseline from which to compare the other two controllers. The second controller that is presented is a nonlinear model-based feedforward controller coupled with PVA error compensation. The final controller again features the nonlinear feedforward model and PVA action, but also contains sliding mode control within the 16 msec PWM period. The simulations were programmed in Matlab while the actual controllers were implemented using the C programming language.

5.2 Linear PVA Controller

In this section a linear PVA controller with deadzone compensation (DZC) is designed. The controller structure is described along with the procedure for tuning the gains. Experimental results are then given for three different trajectories.

5.2.1 PVA Controller Design

A PVA controller is a single-input single-output (SISO) controller that calculates and outputs a control signal based on the measurement of a single feedback signal. A PVA controller was used by Ning and Bone to control a pneumatic servo system [49]. In the case of the hydraulic system for the miniature joint, the measured feedback signal is the absolute linear position of the rack and the control signal sent to the valves is the PWM duty cycle. The control structure for the PVA controller is shown in Figure 5.2.1.

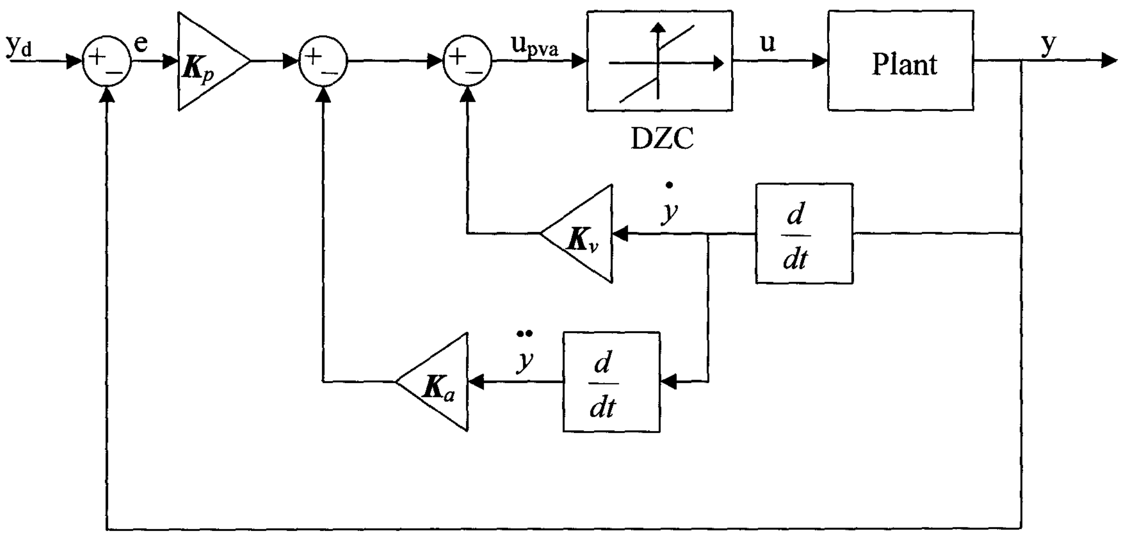

Figure 5.2.1: PVA + DZC controller structure

The PVA portion of the controller is given by the equation,

$$u_{pva} = K_p(y_d - y) + K_v\dot{y} + K_a\ddot{y} \tag{5.2.1}$$

where the gains K_p, K_v, and K_a represent the proportional, velocity and acceleration gains respectively. Note that a negative value for u signifies a change in rotational direction from clockwise to counter-clockwise. This is achieved by activating the other pair of valves.

As can be seen from equation 5.2.1, the PVA control structure requires both the velocity and acceleration. Since direct measurement of the velocity and acceleration is not available, their values must be estimated from the position. The velocity was estimated from the position using a low-pass filtered derivative, sometimes referred to as a velocity observer [44]. The observer functions are given as,

$$\begin{aligned} \hat{v} &= z_v + K_{OB}y \\ \dot{z}_v &= -K_{OB}\hat{v} \end{aligned} \tag{5.2.2}$$

where $\hat{v}$ is the velocity estimate and K_v is the velocity gain. The Laplace transfer function of the observer has the form,

$$\frac{K_{OB}s}{s + K_{OB}} \tag{5.2.3}$$

By its very nature the derivative action of the observer acts to amplify the high frequency noise contained in the Hall effect sensor's signal. If a low-pass filter is not used the velocity signal could become very noisy, leading to poor controller tracking performance. Therefore, the observer gain K_{OB} of the low-pass filter should be tuned to sufficiently filter out the high frequency noise portion of the Hall effect sensor signal, while still providing fast response. The same observer was also used to estimate the acceleration using the velocity. A plot illustrating the position and estimated velocity and acceleration signals generated from the observer used in the experiments is shown in Figure 5.2.2.

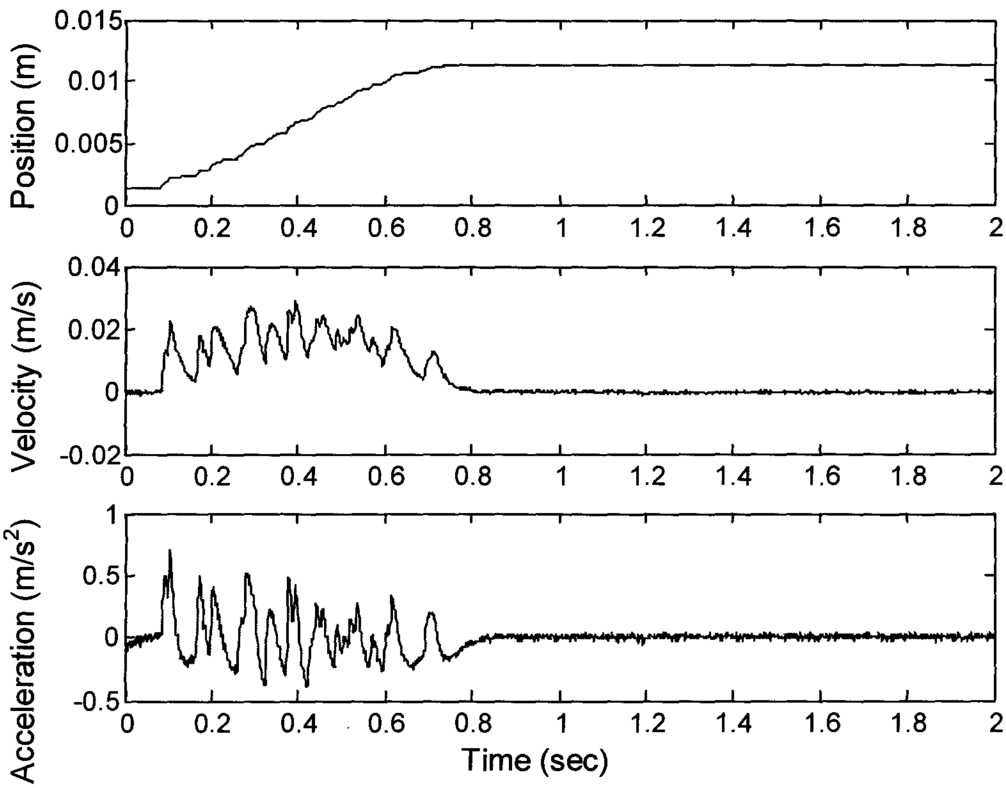

Figure 5.2.2: Position and estimated velocity and acceleration signals

To compensate for the valve delay and static friction, deadzone compensation was utilized similar to that used by Ning and Bone [49]. The deadzone compensation has the form,

$$u = \begin{cases} u_{pva} + 30\% & \text{if } \; u_{pva} > 0 \\ 0 & \text{if } \; u_{pva} = 0 \\ u_{pva} - 30\% & \text{if } \; u_{pva} < 0 \end{cases} \tag{5.2.4}$$

where u_{pva} is the control signal calculated by the PVA control structure. When u_{pva} is nonzero, the DZC acts to increment u_{pva} by ± 30%, which is the minimum duty cycle required to ensure that the valve turns on. The above DZC logic is employed if the positional error is larger than ± 0.3 mm. This value was arrived at through manually tuning the controller.

5.2.2 Experimental Results

Experiments were run to test the performance of the linear PVA controller. Three trajectories were tested as shown in Table 5.2.1. Each trajectory was tested five times in order to verify the repeatability of the controller's results.

Table 5.2.1: Trajectories used for the PVA controller experiments.

	Trajectory
1	Point-to-point rotation of the joint by 120° with cycloidal rising in the first second
2	Ramp speed of 10 mm/s
3	0.5 Hz sine wave with a 60° amplitude

The equations for the cycloidal motion profile of trajectory one are as follws:

$$\ddot{y}(t) = A_{\max} \sin \omega t \tag{5.2.5}$$

$$\dot{y}(t) = -\frac{A_{\max}}{\omega} \cos \omega t + \frac{A_{\max}}{\omega} \tag{5.2.6}$$

$$y(t) = -\frac{A_{\max}}{\omega^2} \sin \omega t + \frac{A_{\max}}{\omega} t \tag{5.2.7}$$

where A_{max} is the maximum acceleration and ω is the frequency of the profile in rad/s.

The gains used in the PVA controller were manually tuned to be: K_p = 80,000 [% / m], K_v = 50 [% / m/ s], and K_a = 1.5 [% / m / s^2]. As a starting point for tuning the gains the units of each gain were considered in selecting an initial guess. For the proportional gain a desired precision of 0.1 mm (0.0001 m) along with a corresponding desired valve duty cycle of 1 % was selected, giving an initial guess of 10,000 [% / m] for K_p. Initial guesses for both K_v and K_a were scaled relative to K_p. This was done by noting that from the open-loop tests the velocity of the system ranged between 0.01 m/s and 1 m/s while the acceleration ranged between 0 m/s^2 and 10 m/s^2. Since the velocity and acceleration are obtained from the derivatives of the position, it was important to limit the magnitude of K_v and K_a so as not to magnify the noise from the Hall effect sensor.

The experimental results for one test from each trajectory are plotted in Figures 5.2.3 to 5.2.5. Note that while the controller uses the rack displacement for its calculations, the results are plotted in degrees to give a clearer physical interpretation. Also, note that the scale for the error plot varies among the trajectories. This is done to improve the visibility of the error plots for each trajectory. However, to best illustrate the differences in tracking performance between the three control strategies the error scale for a given trajectory plot is the same for all controllers. In order to numerically measure the tracking performance of this and the other controllers, two metrics are used: the steady-state error (SSE) and the root of the mean square error (RMSE) given by,

$$\text{RMSE} = \sqrt{\frac{1}{n}\sum_{i=1}^{n} e_i^{\,2}} \tag{5.2.8}$$

where n is the number of data points and e_i is the error for the ith data point. The SSE and RMSE values for all three controllers is tabulated and compared in section 5.5.

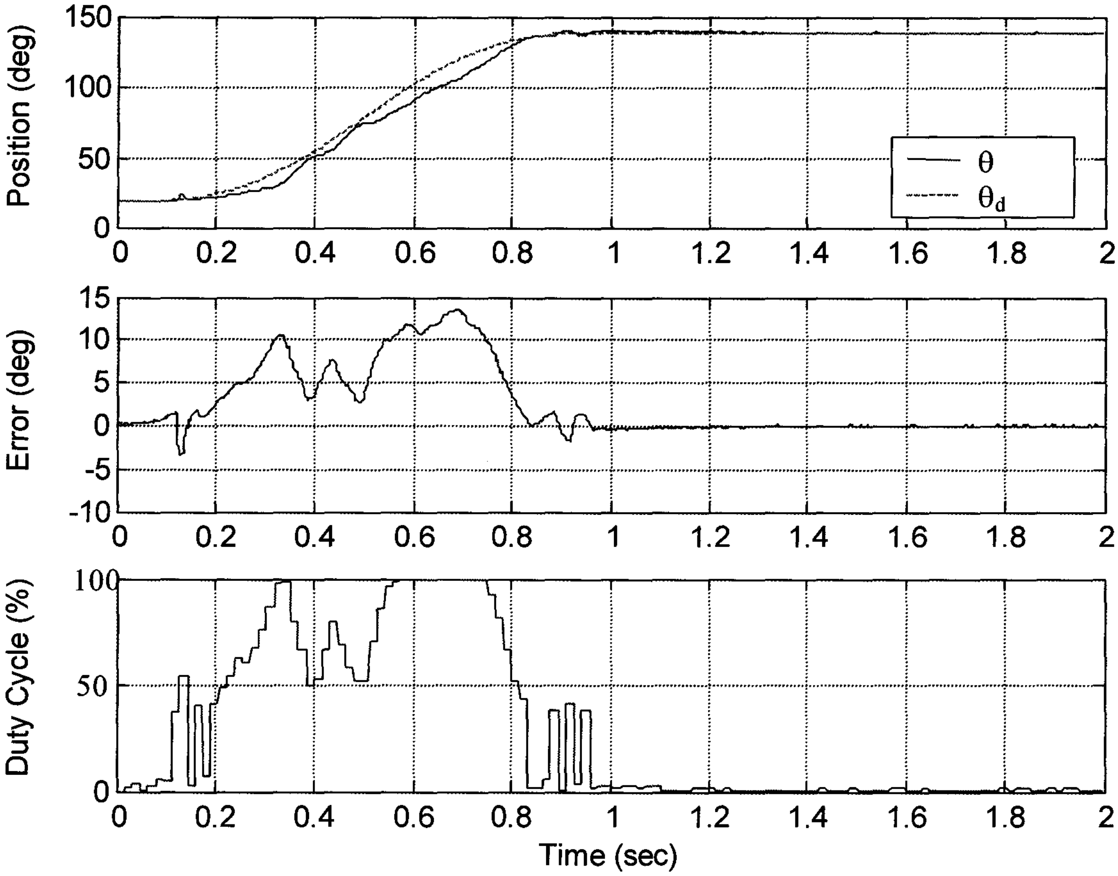

Figure 5.2.3: Trajectory 1 tracking experiment with PVA + DZC controller.

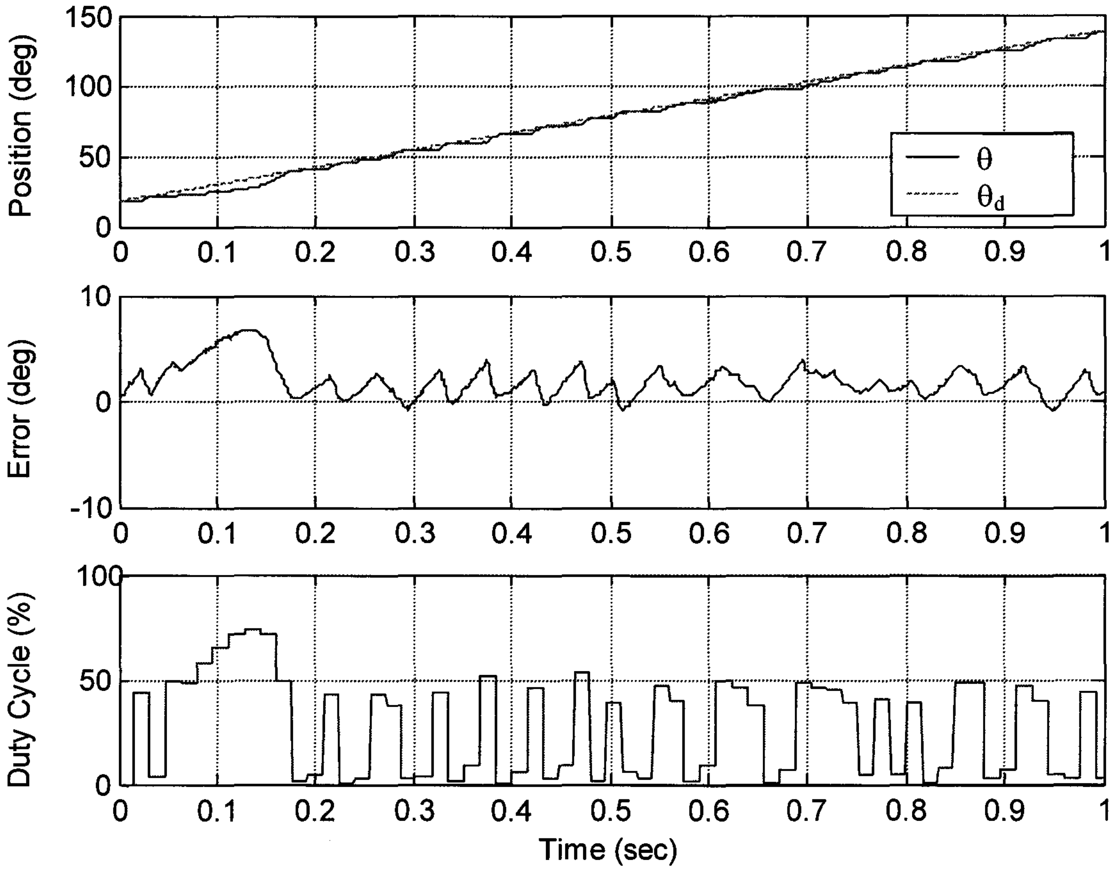

Figure 5.2.4: Trajectory 2 tracking experiment with PVA + DZC controller.

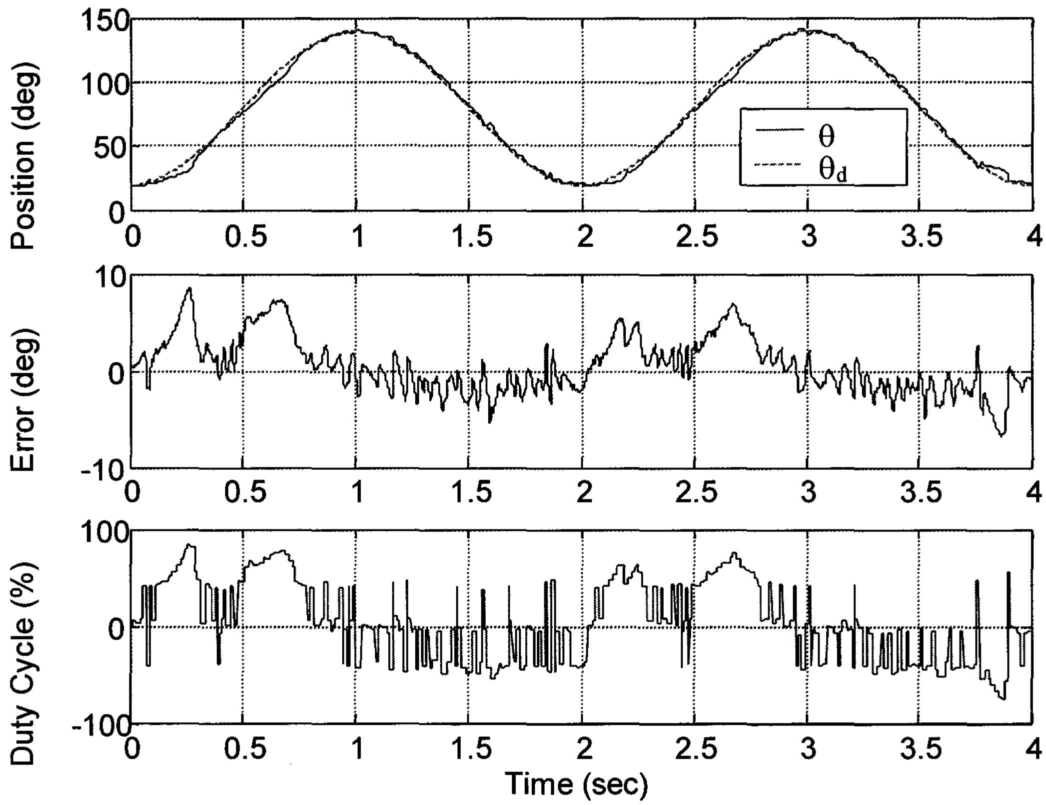

Figure 5.2.5: Trajectory 3 tracking experiment with PVA + DZC controller.

For trajectory 1, the steady-state error (SSE) in joint position was found to be in the range of ± 0.41°, or ± 0.034 mm in terms of rack position. However, as can be seen from Figure 5.2.3, the tracking performance during the cycloidal rising portion is quite poor with a maximum tracking error of 13.5° while the mean RMSE for the five tests is 4.2°, or 0.349 mm. The tracking performance for trajectories 2 and 3 are better with mean RMSE values of 2.93° (0.243 mm) and 3.00° (0.249 mm) respectively. The main causes of the SSE are friction and the minimum resolution of the valves due to their inherent time delays. The poor tracking performance can be attributed to the DZC's failure to adequately compensate for the changing friction loss of the system.

5.3 Model-based Feedfoward + PVA Controller

In this section a nonlinear model-based controller is given. The controller feeds forward a control signal that is calculated using the nonlinear model derived in chapter 4. The feedforward signal is then combined with a PVA control signal before being sent to the valves. The design procedure and controller structure are both described in detail. Simulation and experimental results follow.

5.3.1 Design of Feedforward + PVA Controller

The feedforward + PVA (FF + PVA) controller structure is shown in Figure 5.3.1.

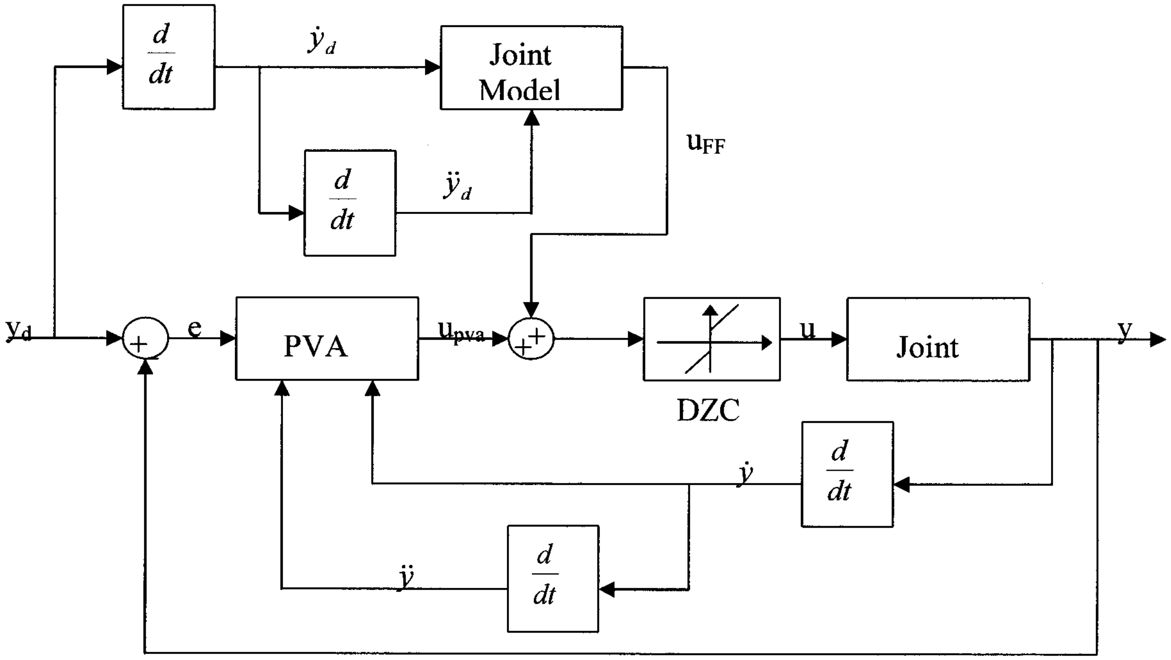

Figure 5.3.1: Model-based feedforward + PVA controller structure.

As can be seen from Figure 5.3.1 the total control signal sent to the valves is made up of three parts: the model-based feedforward signal, the PVA signal, and the DZC signal.

The feedforward part of the controller calculates the desired duty cycle for the valves by using the model equations developed in chapter 4. As described in chapter 4, the dynamic model equation for the hydraulic system is given by,

$$P_{ws}A - R_1A^2\dot{y} - R_4A^2\dot{y} - F_l = M\ddot{y} \tag{5.3.1}$$

Since both P_{ws} and R_1 are known quantities in the system, it is possible to rearrange equation 5.3.1 to solve for the required discharge valve resistance (R_4) necessary to achieve a desired rack velocity and acceleration. To illustrate, let $\dot{y}$ = $\dot{y}_d$ and $\ddot{y}$ = $\ddot{y}_d$. Then rearranging to solve for R_{v2}, equation 5.3.1 becomes,

$$R_4 = \frac{P_{ws}A - M\ddot{y}_d - R_1A^2\dot{y}_d - \hat{F}_l(y_d, \dot{y}_d)}{A^2\dot{y}_d} \tag{5.3.2}$$

where $\hat{F}_l$ is the estimated force loss calculated for a desired joint position and velocity using equations 4.5.5 and 4.5.7 given in sections 4.5.2 and 4.5.3. The appropriate duty cycle for the discharge valve can then be calculated by rearranging equation 4.4.2 to give,

$$d = \left(\frac{R_4}{1.8372x10^{14}}\right)^{\frac{-1}{2.1706}} \quad . \tag{5.3.3}$$

Combining equations 5.3.2 and 5.3.3 gives the feedforward control signal,

$$u_{FF} = \left[\frac{P_{ws} - M\ddot{y}_d - R_1A^2\dot{y}_d - \hat{F}_l(y_d, \dot{y}_d)}{(1.8372x10^{14})A^2\dot{y}_d}\right]^{\frac{-1}{2.1706}} \tag{5.3.4}$$

Examining equations 5.3.2 and 5.3.4, one can see that when the desired joint velocity equals zero the resistance of the discharge valve goes to infinity, causing the commanded duty cycle to be equal to zero. In order to avoid division by zero the value of the feedforward signal is simply set to zero whenever the desired joint velocity equals zero.

The total controller signal is the sum of the feedforward signal and the PVA signal as given by,

$$u = u_{FF} + u_{pva} = u_{FF} + K_p(y_d - y) + K_v\dot{y} + K_a\ddot{y} \tag{5.3.5}$$

The DZC signal shown in Figure 5.3.1 is once again used to compensate for the valve delay but its logic is different than that used in the PVA controller. The new DZC logic is given as,

$$u = \begin{cases} u = 30\% & if \quad 20\% \le u_{FF} + u_{pva} \le 30\% \\ u = -30\% & if \quad -30\% \le u_{FF} + u_{pva} \le -20\% \\ u = u_{FF} + u_{pva} & \quad\; otherwise \end{cases} \tag{5.3.6}$$

The new ranges for the DZC were arrived at by manually tuning the controller. The time period of the control signal to the valves is 16 ms, giving a control frequency of 62.5 Hz.

5.3.2 Simulation Results for the Feedforward + PVA Controller

Simulations were run to predict the tracking performance of the controller. In the simulations the friction model was assumed to be perfect, however the valve opening and closing delays of 5 ms and 2 ms respectively were included in the model of the joint response. The three PVA controller gains were manually tuned in the simulation with the goal of increasing the gains until the tracking errors were minimized without causing system instability.

Four trajectories were tested in the simulations as shown in Table 5.3.1.

Table 5.3.1: Trajectories used for simulation of FF + PVA controller.

	Trajectory
1	Point-to-point rotation of the joint by 120° with cycloidal rising in the first second
2	Ramp speed of 10 mm/s
3	0.5 Hz sine wave with a 60 deg amplitude
4	Series of point-to-point rotations with intermittent periods of rest

Trajectory four consists of four point-to-point rotations with cycloidal rising. First, a rotation of 120° with cycloidal rising in the first second is completed followed by a rest of 1 second. The second rotation is –120° with cycloidal rising in the first second, which takes the joint back to its initial point where it remains for 0.5 seconds. The joint then rotates 60° with cycloidal rising in the first 0.5 seconds, rests for 0.5 seconds and then rotates in an opposing trajectory back to the 0° position where it remains for the final second. A plot of the trajectory is shown in Figure 5.3.2.

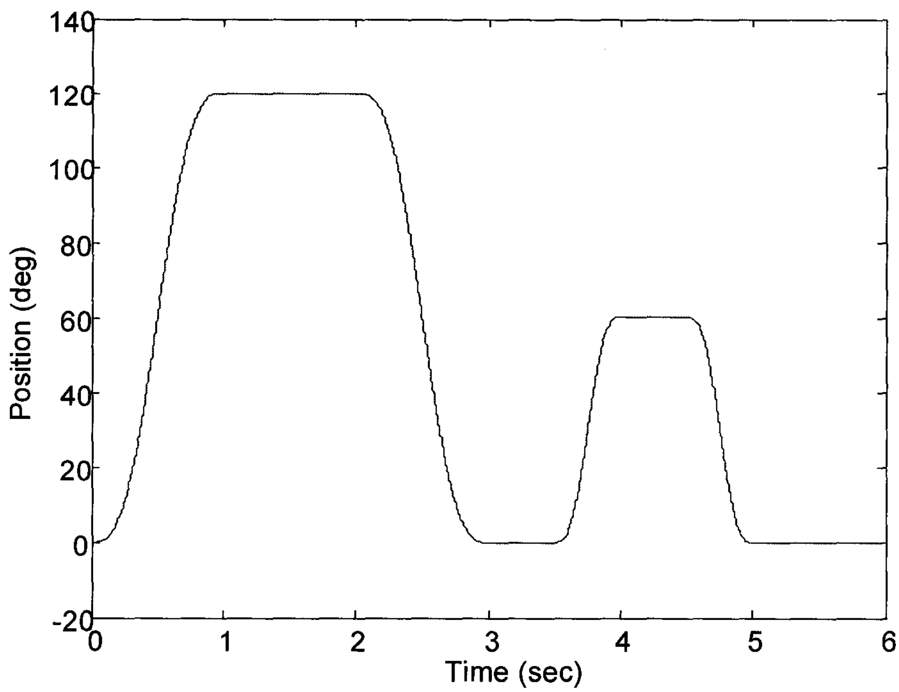

Figure 5.3.2: Fourth trajectory

The PVA gains used in the simulation were manually tuned to be: K_p = 50,000 [%/m], K_v = 50 [%/m/s], K_a = 1.5 [%/m/s^2]. The simulated results are shown in Figures 5.3.3 to 5.3.6.

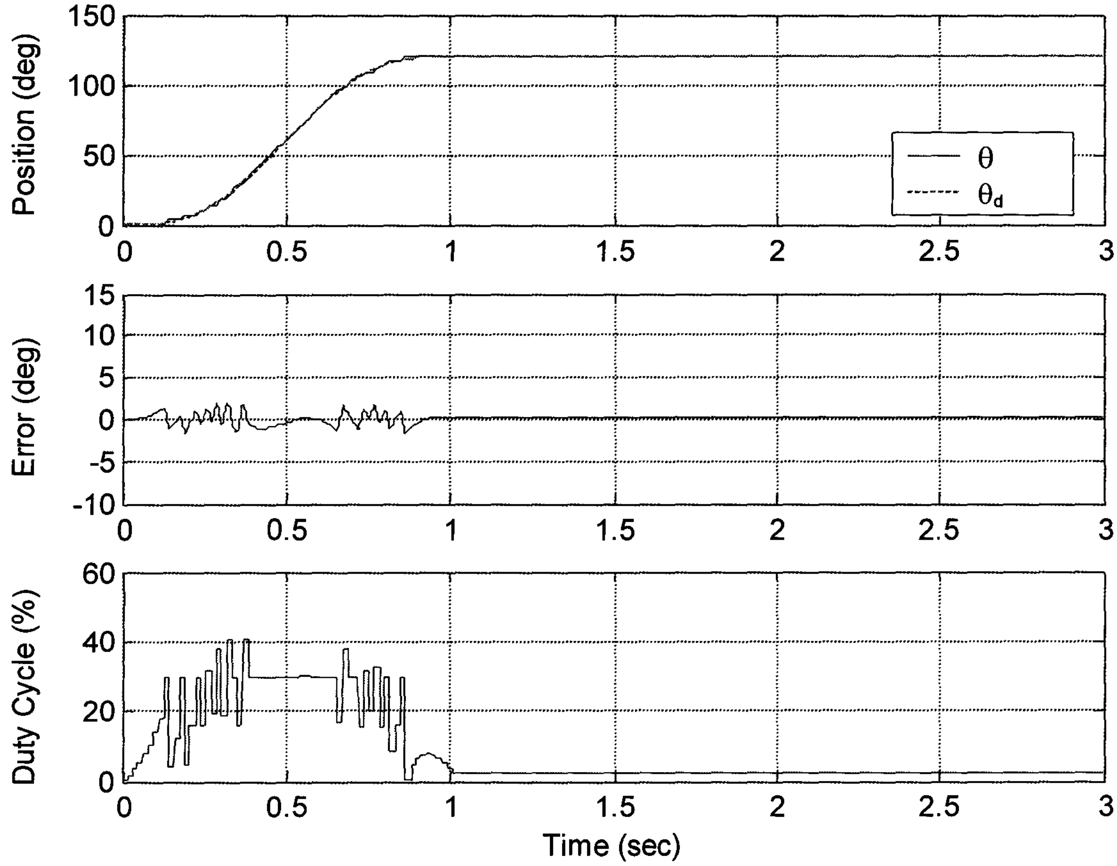

Figure 5.3.3: Trajectory 1 tracking simulation with FF + PVA controller.

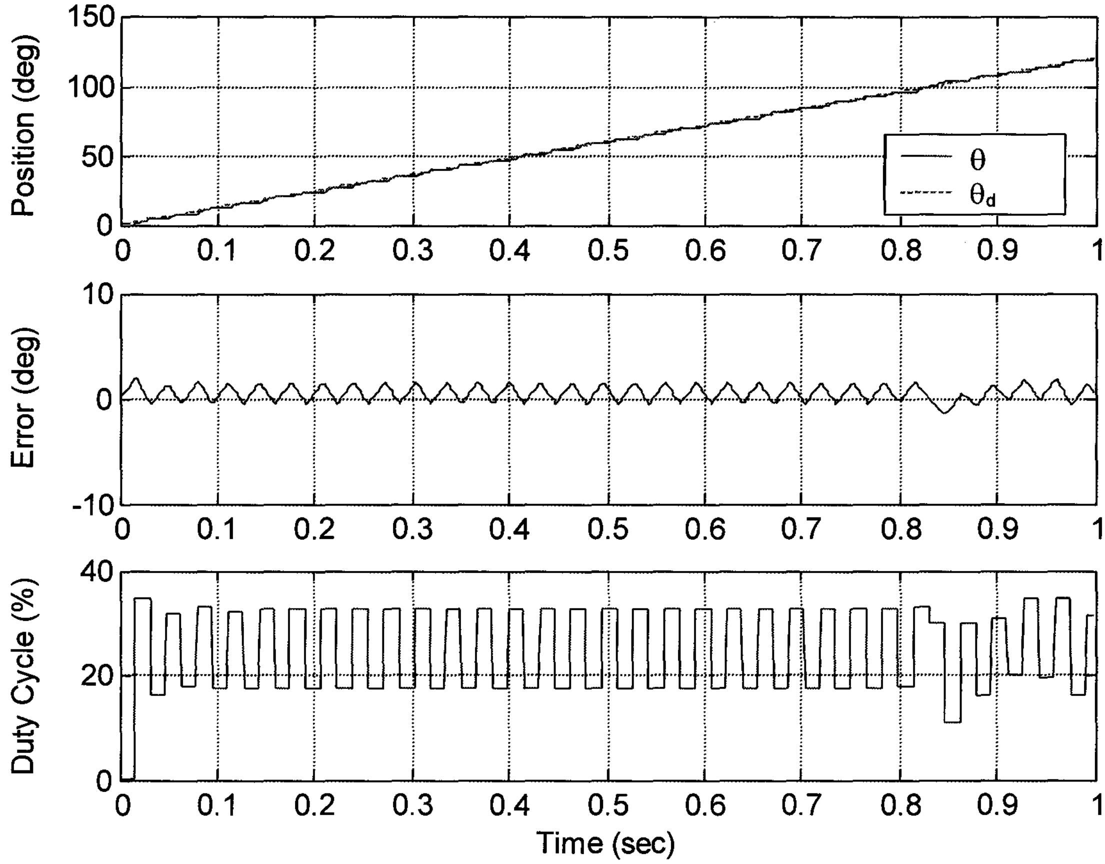

Figure 5.3.4: Trajectory 2 tracking simulation with FF + PVA controller.

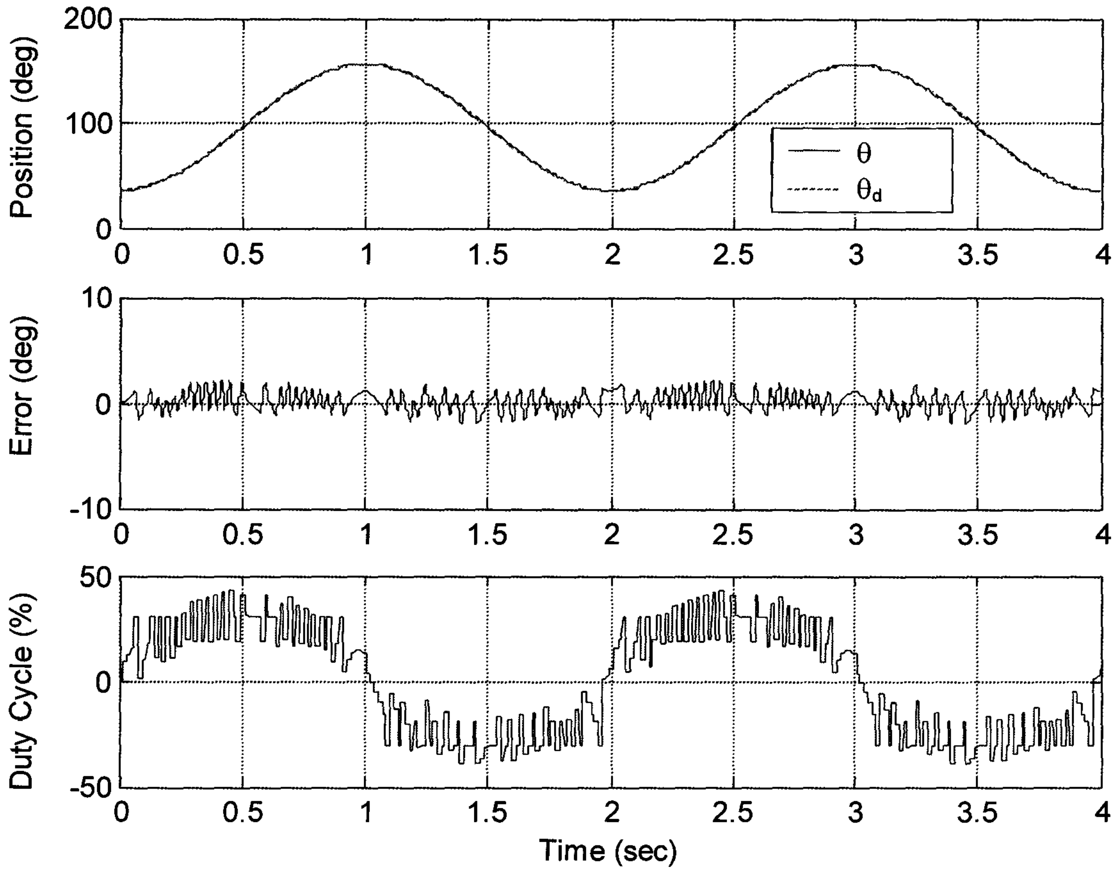

Figure 5.3.5: Trajectory 3 tracking simulation with FF + PVA controller.

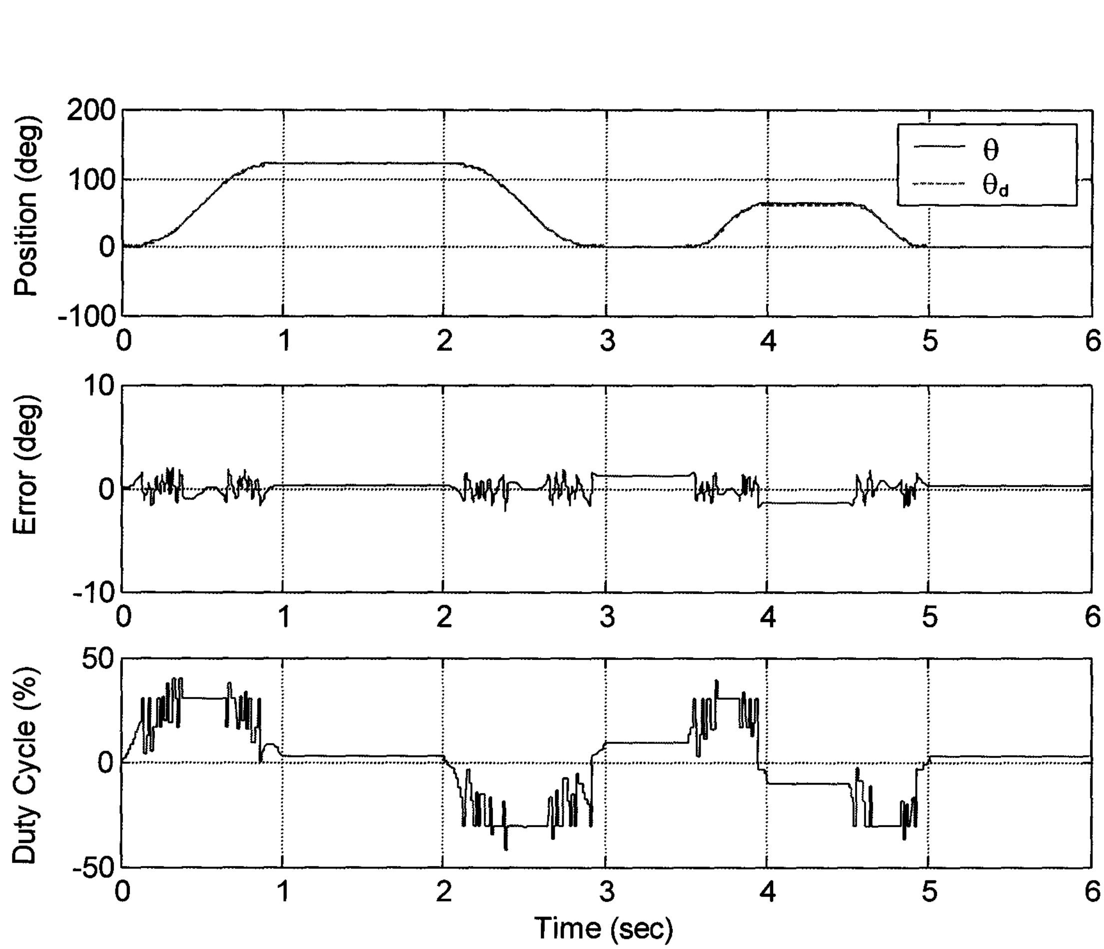

Figure 5.3.6: Trajectory 4 tracking simulation with FF + PVA controller.

The simulations predict promising results for the tracking performance of the model-based feedforward controller design. The SSE for trajectory 1 was 0.35°, while the SSE for the four rest positions of trajectory 4 were 0.35°, 1.21°, -1.39°, and 0.4° respectively. The maximum tracking error for all four trajectories was ± 2°. The RMSE values were 0.52°, 0.83°, 0.91°, and 0.8° for trajectories 1 through 4 respectively. The tracking errors in the simulations were caused by the modeled valve delays.

5.3.3 Experimental Results for the Feedforward + PVA Controller

Experiments were conducted in order to measure the real performance of the feedforward controller. The same four trajectories used in the simulations were tested. Each trajectory was tested five times to verify the repeatability of the controller. During the manual tuning of the gains it was found that only the proportional gain needed to be re-tuned from the simulation values. The new proportional gain was tuned to be K_p = 45,000 [%/m]. Plots of the experimental results are shown in Figures 5.3.7 to 5.3.10.

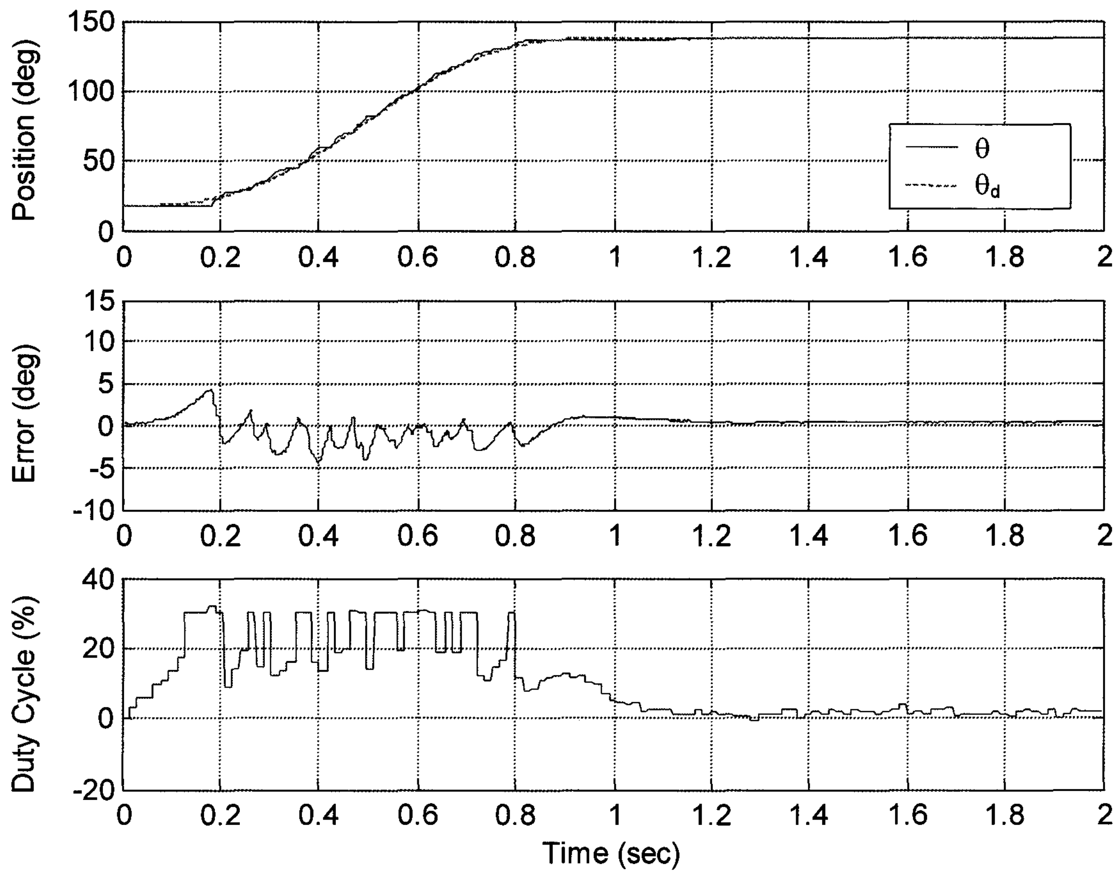

Figure 5.3.7: Trajectory 1 tracking experiment with FF + PVA controller.

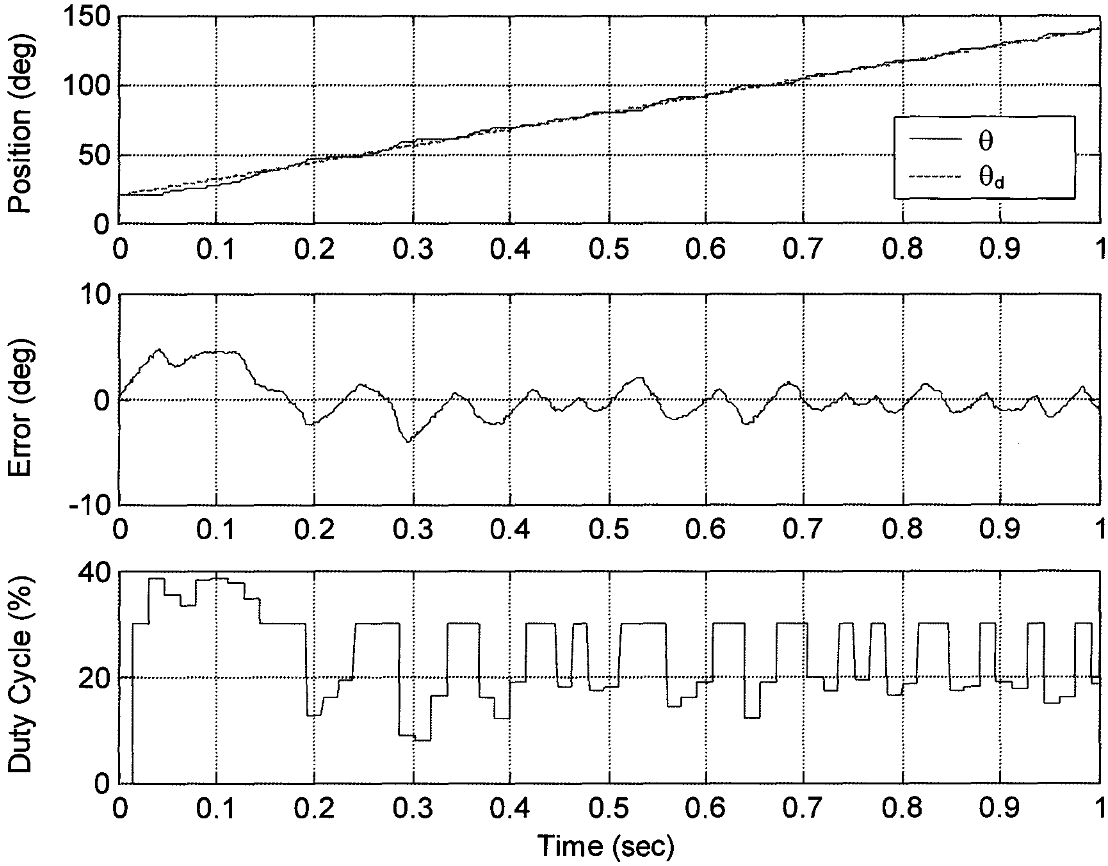

Figure 5.3.8: Trajectory 2 tracking experiment with FF + PVA controller.

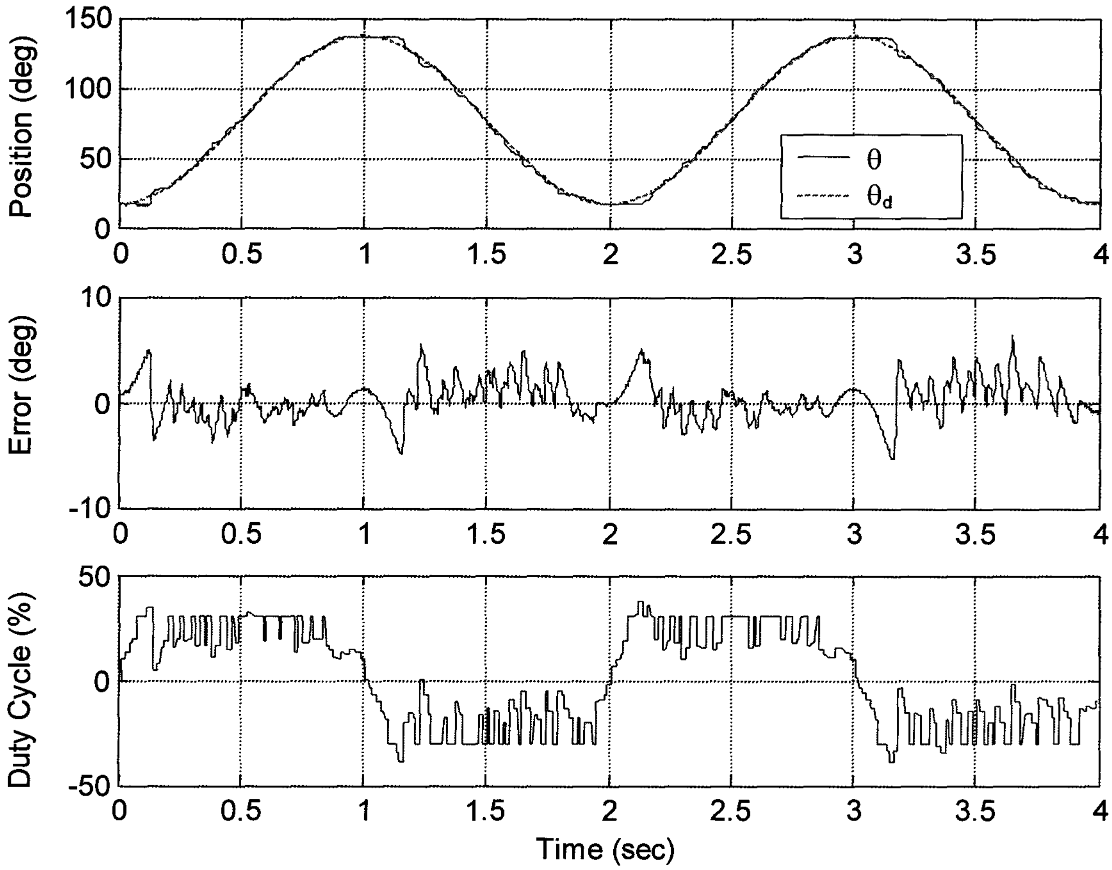

Figure 5.3.9: Trajectory 3 tracking experiment with FF + PVA controller.

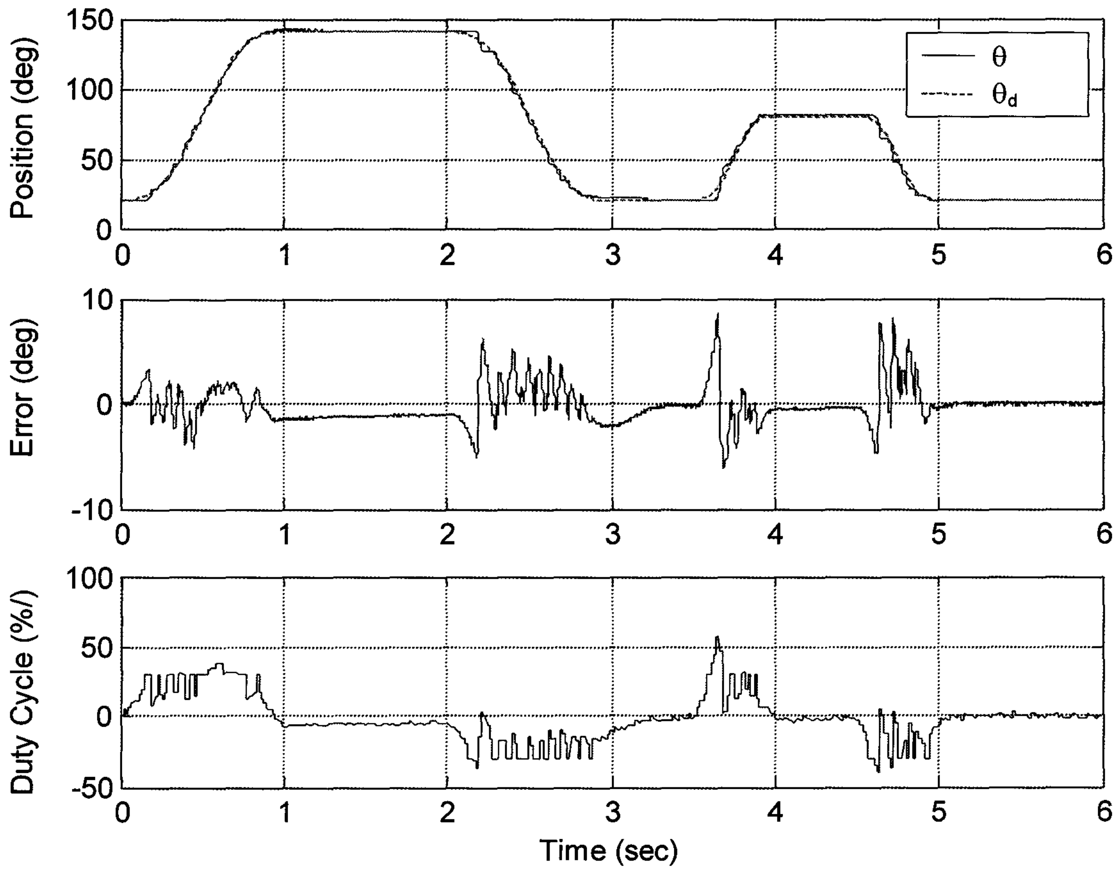

Figure 3.3.10: Trajectory 4 tracking experiment with FF + PVA controller.

The tracking result for trajectory 1 is shown in Figure 3.3.7. The SSE for all five tests is in the range of ± 0.77° while the mean RMSE and maximum tracking error are 1.40° and ± 5° respectively. Figures 3.3.8 and 3.39 show the results for the ramp and sine wave trajectories. The mean RMSE is 2.08° for the ramp trajectory and 2.09° for the sine wave trajectory. Both trajectories had a maximum tracking error of ± 5°. Figure 3.3.10 shows the tracking result for trajectory 4. The SSE range for the four rest positions are ± 1.65°, ± 2.03°, ± 0.99°, and ± 0.5°. The mean RMSE is 1.95° and the maximum tracking error is approximately ± 8°. From both trajectories 3 and 4 one can see that the tracking performance is slightly worse when the joint is moving counter-clockwise (towards 0°). This is due to modeling errors in the direction dependant friction. Overall, the tracking errors found in all four trajectories are a result of the response delays of the valves and friction and valve modeling errors. The contribution of the modeling errors to the overall positional tracking errors of the system can be quantified by comparing the simulation and experimental tracking results. On average the SSE and RSME values for the four trajectories were 50 % and 150 % higher in the experiments than in the simulations. Therefore, modeling errors represent approximately 33 % of the SSE and 60 % of the RSME measured during the experiments.

In the course of tuning the controller it was found that setting the value of the water supply pressure (P_{ws}) inside the feedforward model equation to a constant 300 kPa resulted in better tracking performance than using the measured value. The main reason for this is that the measurement signal reintroduces the pressure oscillations that were previously dissipated by the system through its natural damping. The resulting pressure signal oscillation caused oscillatory behaviour in the motion of the joint, degrading the tracking performance of the controller. A plot of a measured water supply pressure signal for one of the trajectory 1 tests is shown in Figure 5.3.11.

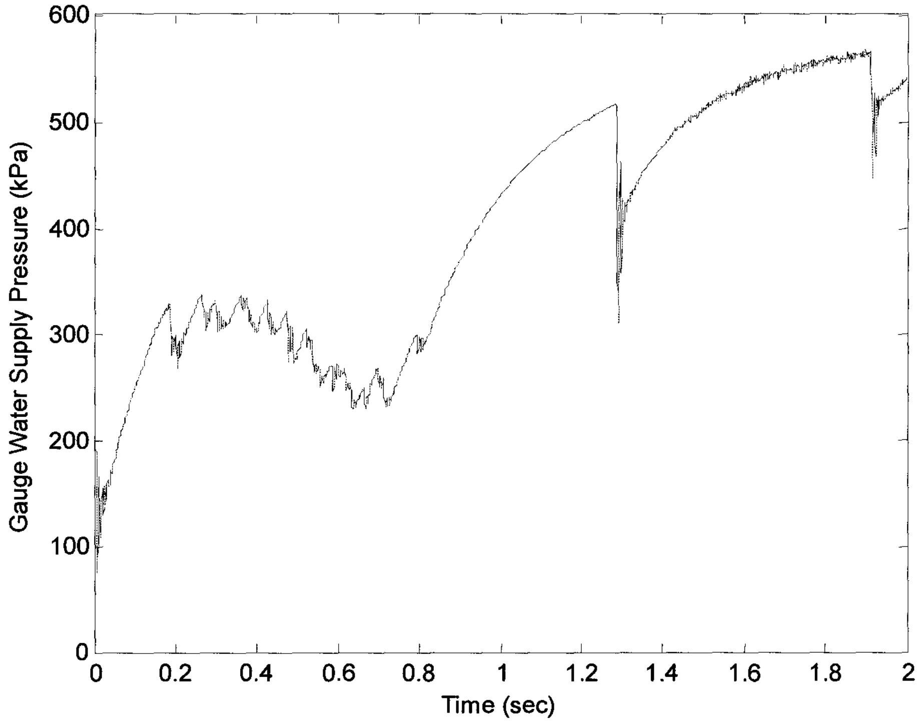

Figure 5.3.11: Water supply pressure (kPag) for trajectory 1 control.

The pressure oscillations present during the first 0.8 seconds occur while the joint is moving and are a direct result of the discharge valve rapidly opening and closing under the PWM signal. During this period the water supply pressure is less than it is in the static case. This makes sense if one remembers that the supply water is of finite volume and is pressurized through the compressive force generated by air in the opposing chamber. When one of the discharge valves is open to the atmosphere, the water begins to flow through the hydraulic circuit drawing water from the inside the supply cylinder. As the water leaves the cylinder the pressure imbalance between the two chambers causes the piston to accelerate. However, since the piston is now moving it must overcome dynamic friction. Therefore, the net compressive force acting on the water is less than when the piston is stationary.

After 0.8 s, the discharge valve has been shut and the joint stops moving. Since the system is no longer periodically open to the atmosphere, water does not exit the supply cylinder and the piston stops moving. With the water now trapped on the supply side of the solenoid valves, the water pressure starts to rise until the water and air pressure forces inside the supply cylinder chambers reach a static equilibrium. It can be seen from the figure that as the water pressure rises it is still subjected to residual pressure oscillations within the system that dissipate over time.

5.4 Addition of Sliding Mode Control to the FF + PVA Controller

Sliding mode control is a type of nonlinear, robust controller known as "variable structure control" (VSC). The controller uses switching logic to drive the output to a desired state by changing the structure of the control law based on the current state of the system. Sliding mode control was a logical choice for the given hydraulic system since it responds well to rapidly changing process parameters and mimics the mechanical switching behaviour of the on/off solenoid valves. First, the design procedure for the sliding mode control is described, after which simulation and experimental tracking results are given.

5.4.1 Design of Sliding Mode Control Logic

The objective of adding the sliding mode control to the FF + PVA controller was to provide a way of updating the control signal within the PWM period every 1 ms. This increases the control frequency from 62.5 Hz to 1000 Hz, which theoretically should improve the tracking performance compared to that achieved by the PVA and FF + PVA controllers.

The sliding surface used in the control is a first order function given by,

$$\sigma = \dot{e} + \lambda e = 0 \tag{5.4.1}$$

where: $$e = y_d - y . \tag{5.4.2}$$

Hence, the sliding surface is a line with its two states, velocity and position, used to determine the controller structure. If the switching logic was implemented such that the controller's goal was to drive the system states exactly along the line σ=0 harmful chattering would occur. To avoid this situation, a boundary layer can be added around the sliding surface. When σ is inside the boundary layer the discontinuous switching signal is replaced by a continuous output. The concept is illustrated in Figure 5.4.1.

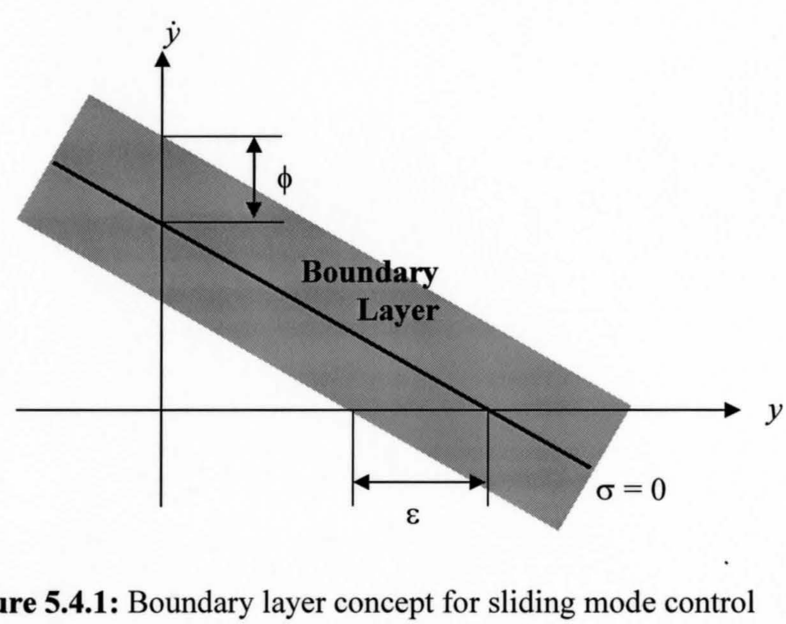

Figure 5.4.1: Boundary layer concept for sliding mode control

From Figure 5.4.1, ϕ is the height of the boundary layer in m/s and ε (= ϕ/λ) is the width of the boundary layer in m, often referred to as the precision.

Including the sliding mode control the total control signal sent to the valves is given by,

$$u = u_{FF+PVA} + u_{sw} \tag{5.4.3}$$

where u_{FF+PVA} is the model-based FF + PVA control signal from before and u_{sw} is the added sliding mode signal. Utilizing the boundary layer concept, the switching signal is given as,

$$u_{sw} = 100 sat\left(\frac{\sigma}{\phi}\right) \tag{5.4.4}$$

where the function $sat(x)$ is given by,

$$sat\left(\frac{\sigma}{\phi}\right) = \begin{cases} \mathrm{sgn}\left(\frac{\sigma}{\phi}\right) & if \quad \left|\frac{\sigma}{\phi}\right| > 1 \\ \left(\frac{\sigma}{\phi}\right) & if \quad \left|\frac{\sigma}{\phi}\right| \leq 1 \end{cases} \tag{5.4.5}$$

where sgn() is the signum function.

By combining equations 5.4.3 and 5.4.4, the total control law can be written as,

$$u = u_{FF+PVA} + 100 sat\left(\frac{\sigma}{\phi}\right) \tag{5.4.6}$$

The control law described by 5.4.6 contains two distinct parts. The signal generated by the FF + PVA controller (u_{FF+PVA}) is calculated outside the PWM period at a frequency of 62.5 Hz. The switching signal (u_{sw}) is calculated and added to the control signal inside the 16 ms PWM period every 1 ms, giving a control frequency of 1000 Hz. Intuitively the switching term allows for faster controller response, which should lead to improved tracking performance. Figure 5.4.2 has been included to help illustrate the effect of the sliding mode action.

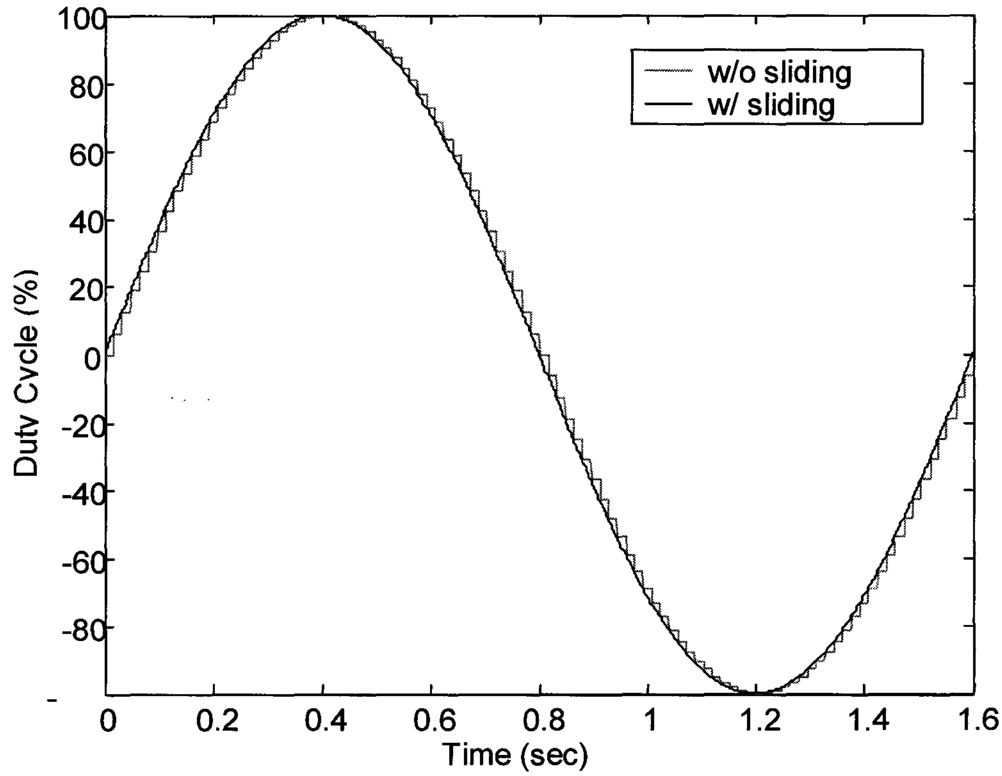

Figure 5.4.2: Illustration of effect of sliding mode action within 16 msec PWM period.

Figure 5.4.2 shows two valve control signals that are modified in a sinusoidal manner. The signal without the sliding mode contribution updates the duty cycle signal to the valve every 16 ms, while the signal with the sliding mode action is able to update the duty cycle every 1 ms. As illustrated by the two signal curves, the addition of the sliding mode action produces a much finer control resolution, which in theory should enable smoother and more accurate position tracking.

Examining equation 5.4.6, one can see that the switching term can range from ± 100%, depending on the magnitude and sign of σ. Simply put, the switching term uses the position and velocity errors to do one of the following with respect to the FF + PVA control command: 1) keep the discharge valve open longer, 2) close the valve early, 3) change direction by activating the other pair of valves, or 4) maintain the status quo. Please note that this controller does not contain the DZC used in the previous two controllers.

In order to implement this controller, values for the two gains λ and ϕ need to be determined. This was done by manually tuning the controller to find their approximately optimal values. If the value of λ is set too high or ϕ is set too low, $sat\left(\frac{\sigma}{\phi}\right)$ will approach ±1, causing the switching signal to approach ±100 % and harmful chattering of the joint will occur. The strategy in tuning the gains was to find the gain values for which the tracking error was minimized without inducing chattering of the joint at the steady-state positions.

5.4.2 Simulation Results

Simulations were run to predict the tracking performance of the controller under four different trajectories. The trajectories tested were the same as those for the FF + PVA controller. The PVA gains were tuned as follows: K_p = 50,000 [%/m], K_v = 50 [%/m/s], and K_a = 1.5 [%/m/s^2]. The switching gains were tuned to be: λ = 80 s^{-1} and ϕ =

0.2 m/s, giving an estimated precision of 0.0025 m. The results are shown in Figures 5.4.3 to 5.4.6.

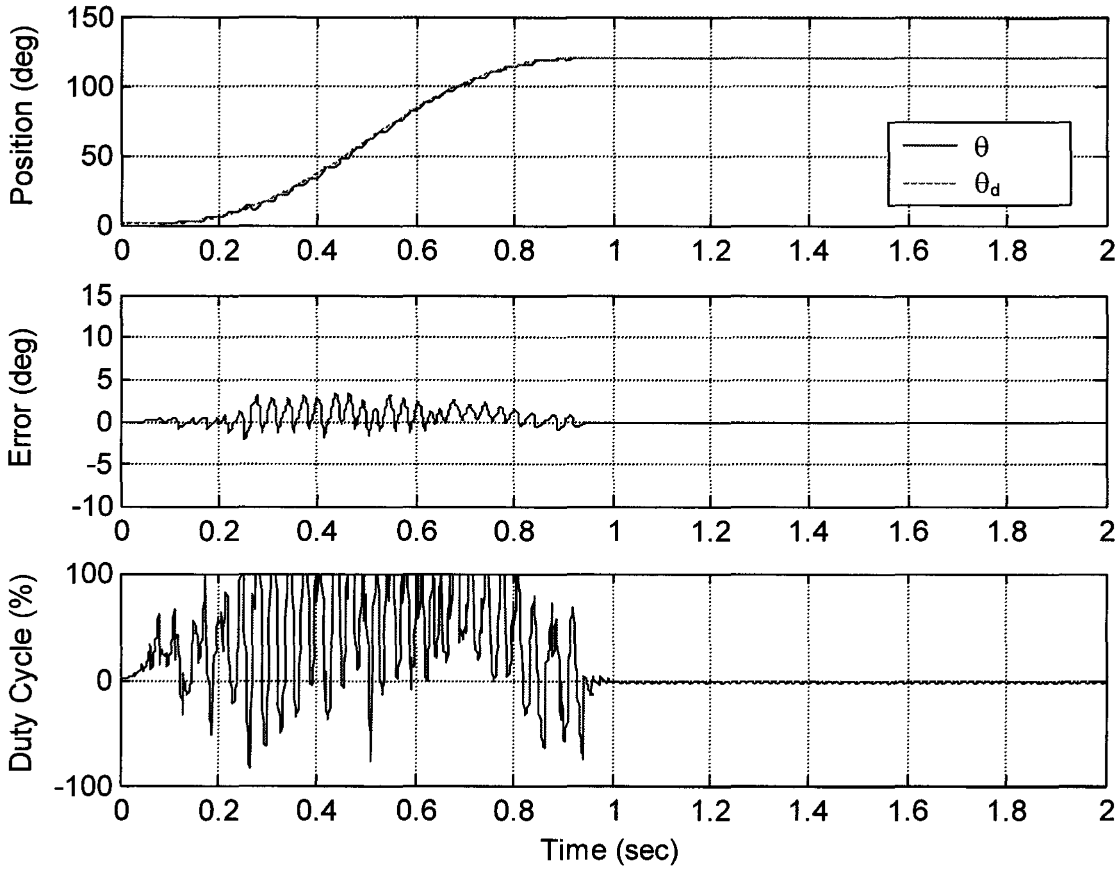

Figure 5.4.3: Trajectory 1 tracking simulation with sliding mode control

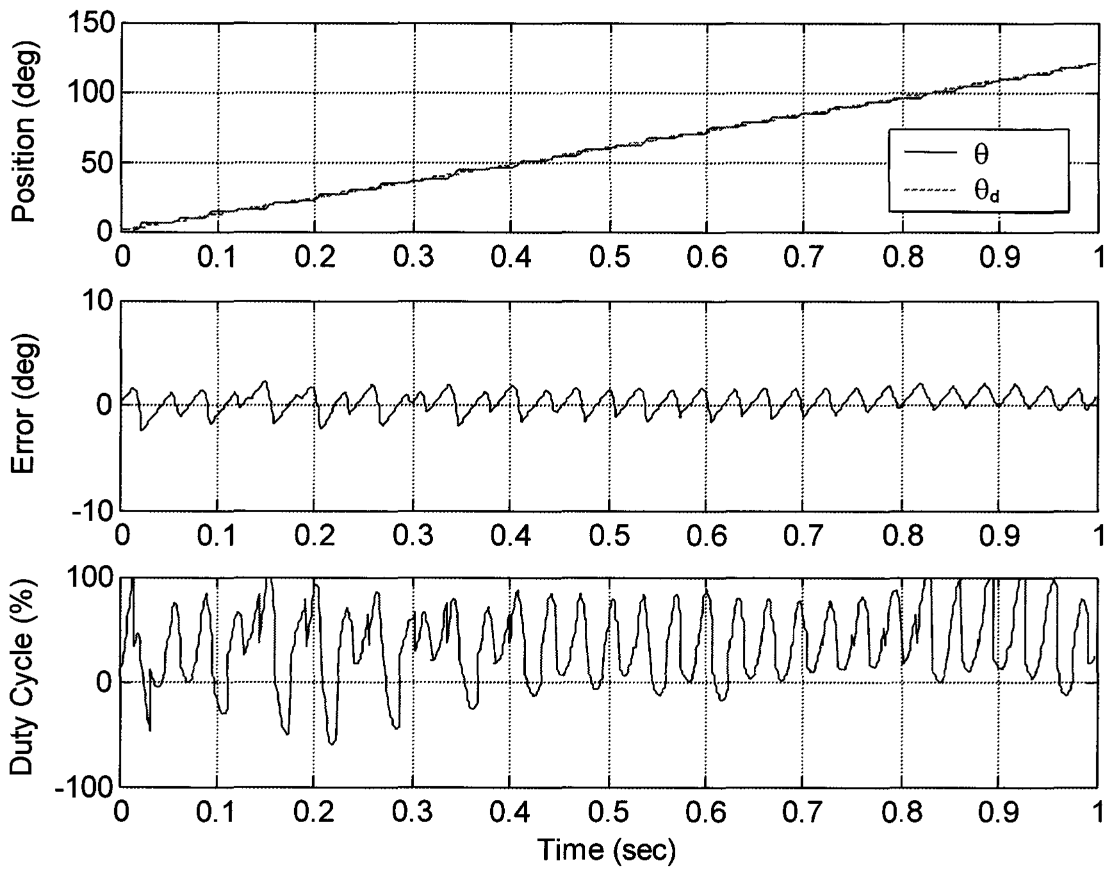

Figure 5.4.4: Trajectory 2 tracking simulation with sliding mode control

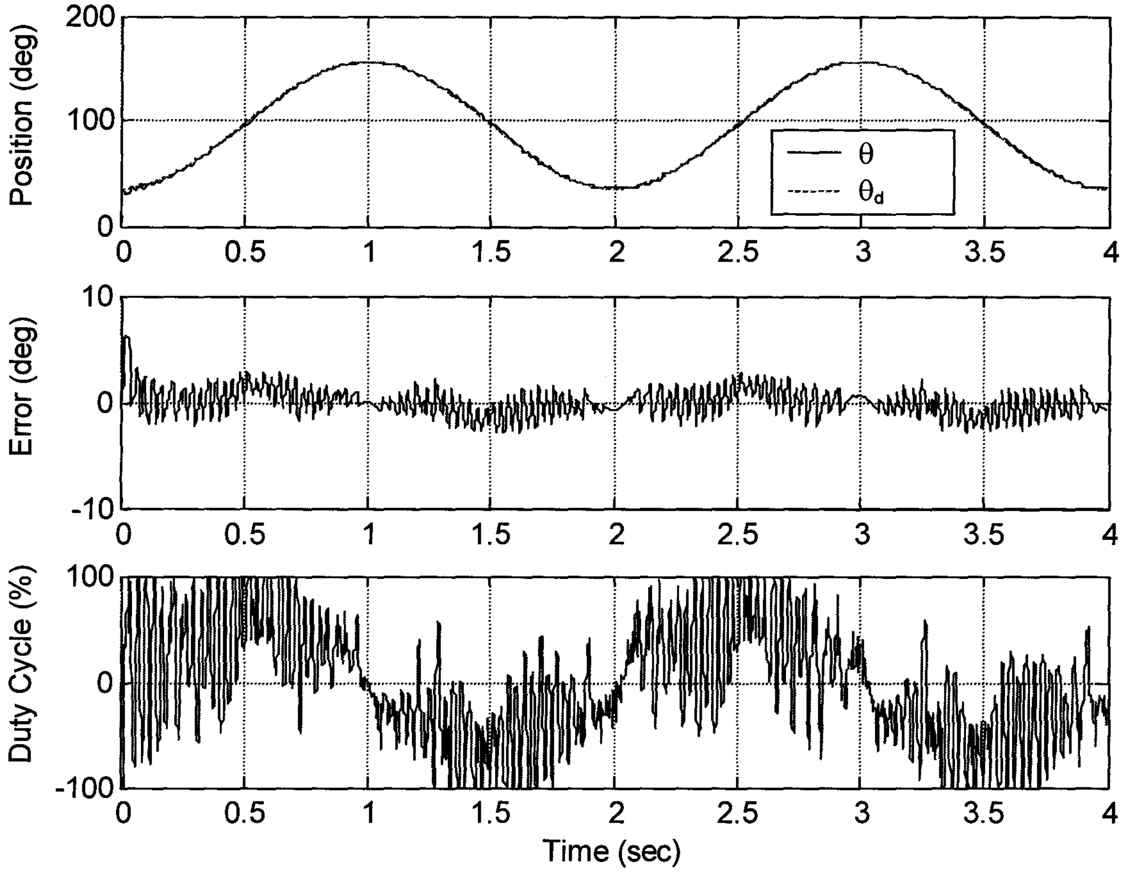

Figure 5.4.5: Trajectory 3 tracking simulation with sliding mode control

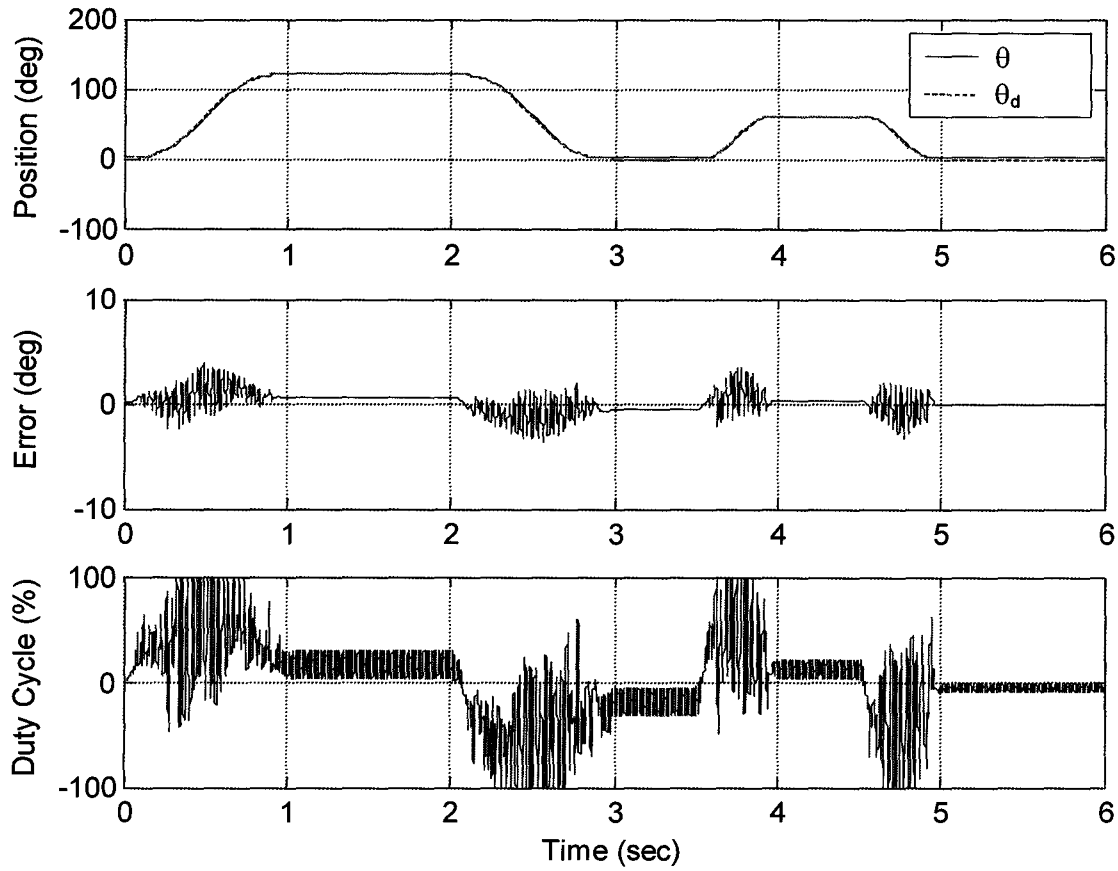

Figure 5.4.6: Trajectory 4 tracking simulation with sliding mode control

The value of the SSE for trajectory 1 was predicted to be 0.53°, while the four SSE values for trajectory 4 were 0.53°, -0.58°, 0.39°, and –0.17°. The RMSE values for trajectories 1 through 4 were 0.86°, 0.99°, 1.26°, and 0.94° respectively, while the maximum tracking error was approximately ± 3° for all four trajectories except for the beginning of trajectory 3 where the maximum tracking error reached ± 7°.

5.4.3 Experimental Results

Experiments were conducted in order to measure the controllers true tracking performance. The same four trajectories as in the simulation were used and five tests were run for each trajectory to verify the repeatability of the controller. For the experiments K_p, λ and ϕ needed to be manually re-tuned from their simulation values. Their re-tuned values were K_p = 50,000 [%/m], λ = 40 s^{-1} and ϕ = 0.3 m/s. The resulting estimated precision (ε) from λ and ϕ was 0.0075 m. The results for each trajectory are shown in Figures 5.4.7 to 5.4.10.

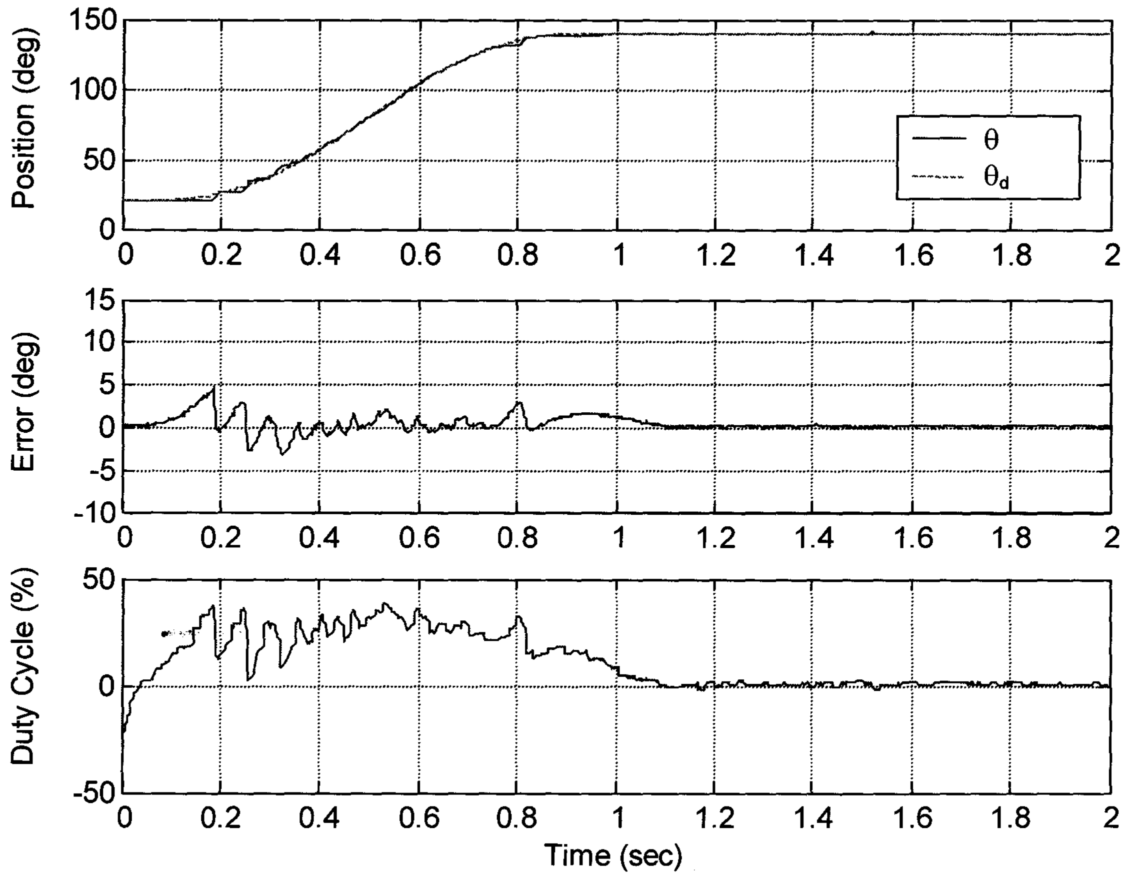

Figure 5.4.7: Trajectory 1 tracking experiment with sliding mode control

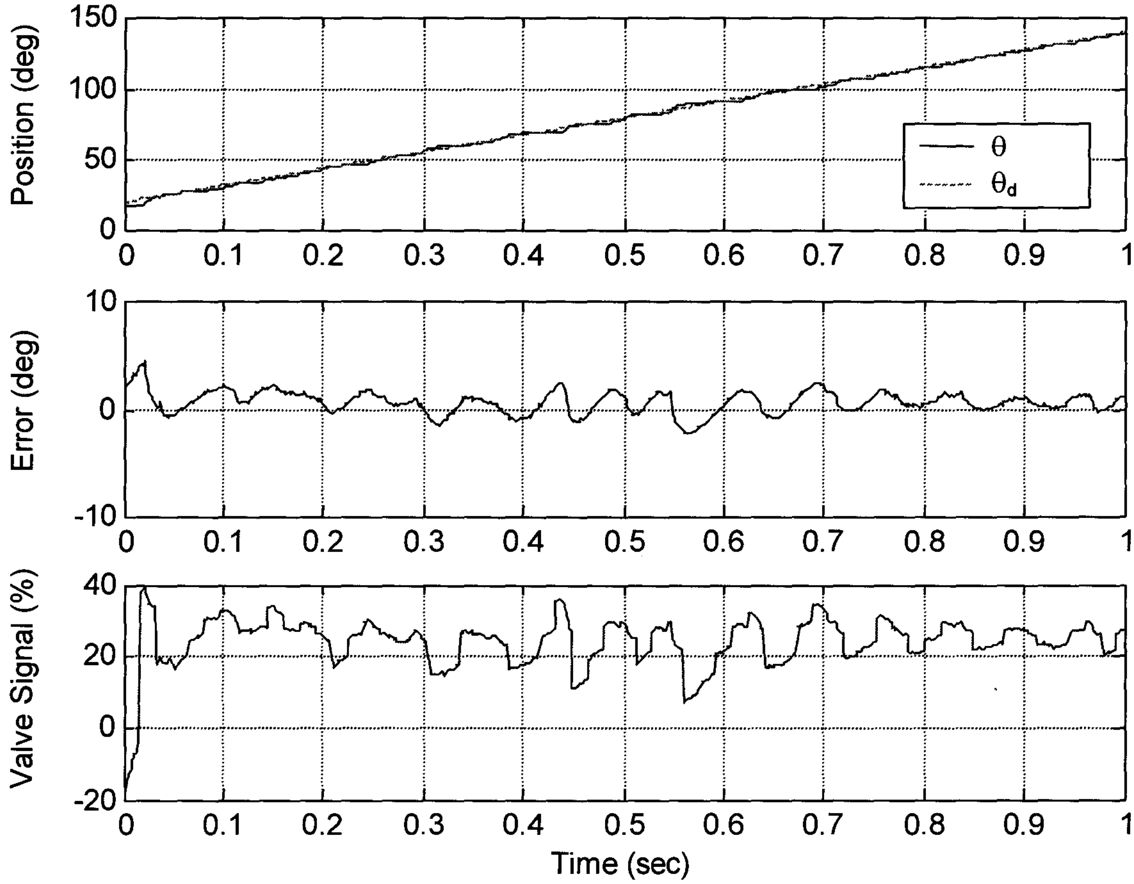

Figure 5.4.8: Trajectory 2 tracking experiment with sliding mode control

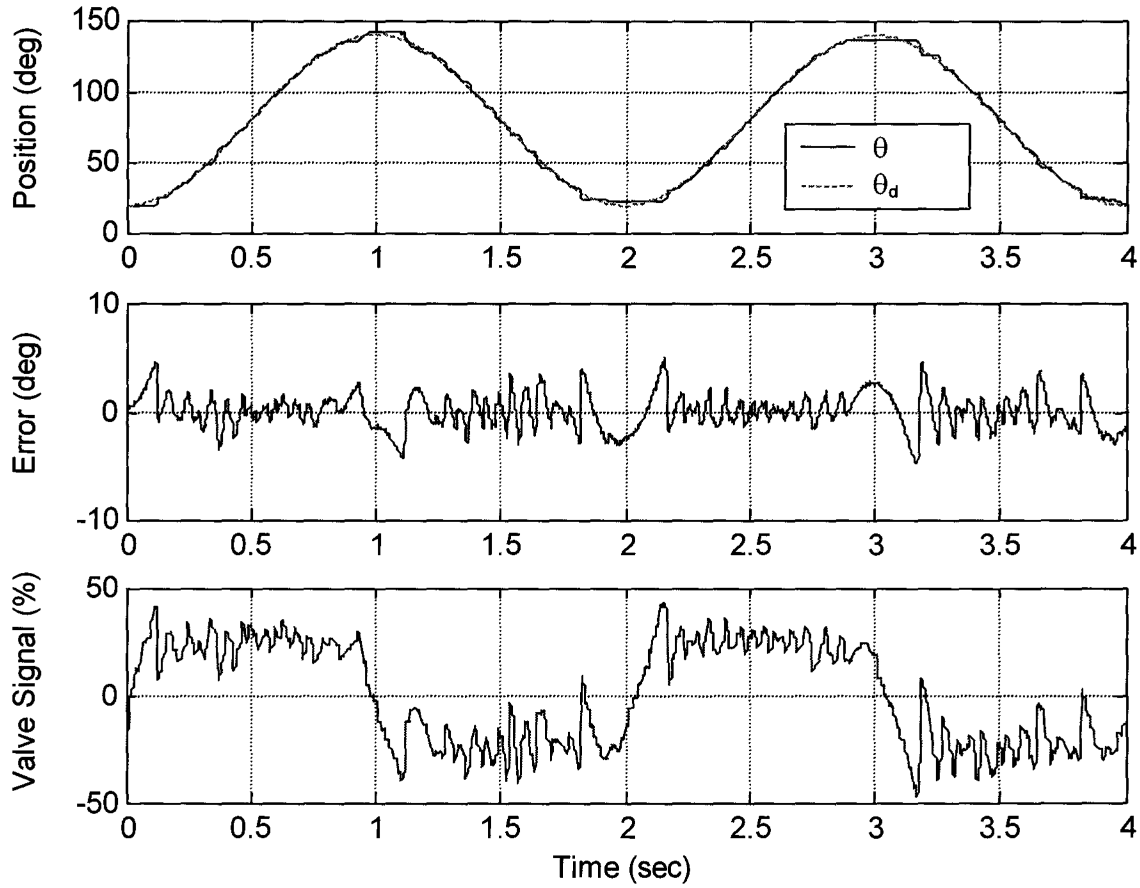

Figure 5.4.9: Trajectory 3 tracking experiment with sliding mode control

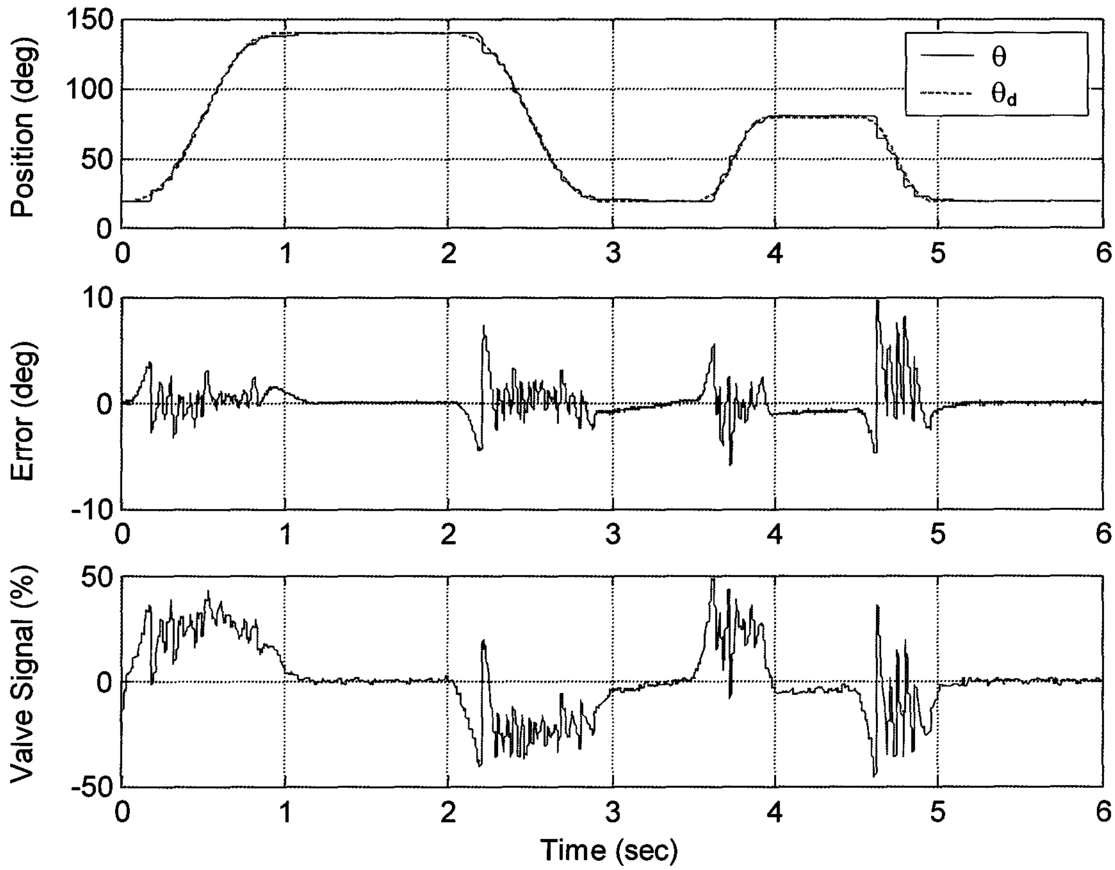

Figure 5.4.10: Trajectory 4 tracking experiment with sliding mode control

The SSE for all five tests of trajectory 1 was in the range of ± 0.85°, while the mean RMSE was 1.19°. The maximum tracking error was 5° at the beginning of the cycloidal rise, but diminished to ± 2.5° shortly after. The mean RMSE for trajectories 2 and 3 were 1.55° and 1.69° respectively. Trajectory 4 had a mean RMSE of 1.82°, while its SSE for the four setpoints were in the ranges of ± 1.43°, ± 2.71°, ± 1.53°, and ± 0.91°. As in the FF + PVA controller case, the tracking error is worse in the counter-clockwise direction due to friction modeling errors. Also, it can be observed from the above figures that the total valve signal sent to the valves changes at a much higher frequency than was the case with the previous two controllers. This is a direct result of the addition of the switching signal.

5.5 Comparison of Controller Performance

For comparison purposes the SSE and mean RMSE values for each controller and trajectory are shown in Tables 5.5.1 and 5.5.2 respectively.

Table 5.5.1: Controller SSE values [deg] for trajectory 1

	Test 1	Test 2	Test 3	Test 4	Test 5	Range
PVA controller	0.004	0.21	-0.06	0.41	-0.16	± 0.41
FF + PVA controller	-0.39	0.12	0.45	-0.44	-0.77	± 0.77
Sliding mode controller	0.32	0.16	0.47	-0.85	0.69	± 0.85

Table 5.5.2: Controller RMSE values [deg] for all 4 trajectories

	Test 1	Test 2	Test 3	Test 4	Test 5	Mean	Std. Dev.
PVA controller							
Trajectory 1	4.77	3.62	3.50	3.69	5.40	4.20	0.76
Trajectory 2	3.48	2.48	3.92	2.40	2.35	2.93	0.65
Trajectory 3	3.60	2.53	2.89	3.57	2.41	3.00	0.50
Feedforward + PVA controller							
Trajectory 1	1.42	1.38	1.31	1.42	1.49	1.40	0.06
Trajectory 2	1.96	1.81	2.03	2.21	2.41	2.08	0.21
Trajectory 3	1.89	2.10	2.04	2.22	2.21	2.09	0.12
Trajectory 4	1.86	1.80	2.24	1.88	1.98	1.95	0.16
Sliding mode controller							
Trajectory 1	1.28	0.98	1.27	1.15	1.26	1.19	0.11
Trajectory 2	1.33	1.85	1.74	1.62	1.20	1.55	0.25
Trajectory 3	1.60	1.81	1.60	1.67	1.77	1.69	0.09
Trajectory 4	2.02	1.55	1.98	1.74	1.83	1.82	0.17

From Table 5.5.1 one can see that the SSE is quite good for all three controllers, with the maximum range being ± 0.85°, or 0.07 mm. From Table 5.5.2 it can be seen that the tracking performance, as measured by the RMSE, is improved dramatically when the PVA controller is replaced by the model-based FF + PVA controller. The resulting average reduction in the RMSE is 42 %. The performance is improved further by adding the switching action of the sliding mode control to the FF + PVA controller. The sliding mode controller offers an average reduction in the RMSE of 54 % compared to the PVA controller and 16.5 % compared to the FF + PVA controller. This is due mainly to the increase in the controller's effective sampling frequency that helps to compensate for any modeling errors. Finally, the FF + PVA controller and the sliding mode controller both greatly improve the tracking performance standard deviation.

5.6 Conclusions

Three controllers were designed and tested for various trajectories to determine their tracking performance. First, a linear PVA controller was designed and used as a baseline to measure against the performance of the other two controllers. Second, a model-based feedforward controller coupled with linear PVA control was designed and tested. Third, sliding mode control was added inside the PWM period of the previous FF + PVA controller in order to increase the controller's effective sampling frequency. From the results it was found that both model-based controllers dramatically outperformed the linear PVA controller giving average reductions in the RMSE of 42 % and 54 % for the FF + PVA and sliding mode controllers respectively. The sliding mode controller was found to provide the best overall tracking performance for all trajectories tested and gave an RMSE reduction of 16.5 % when compared to the FF + PVA controller.

CHAPTER 6

ROBUSTNESS TESTING

6.1 Introduction

In the control systems field, the term robustness is used to describe a controller's ability to compensate for modeling errors and to reject disturbances. In practice the system models used in control are never 100 % accurate. It is still important however, that the controller be able to provide quality results. In this chapter the robustness of the both the feedforward + PVA controller and sliding mode controller are tested through two sets of experiments. In the first test, the payload that is moved by the joint is varied. The second test is a vertical motion test where the joint must act against unmodeled gravity while lifting different applied payloads.

6.2 Variation of Moving Payload

Under nominal model conditions the joint is carrying no load. In order to test the robustness of the two controllers to changes in payload, masses of 6.5 grams and 13.5 grams were placed on the end of the second link. Two trajectories were tested for each case: trajectory 1, the point-to-point rotation of 120° with cycloidal rising in the first second, and trajectory 3, the 0.5 Hz sine wave with amplitude of 60°. Each of the two trajectories was tested five times under each payload. The SSE results for all five tests of trajectory 1 for each controller are shown in Table 6.2.1. The RSME results for each test of the two trajectories are shown in Table 6.2.2. A comparison of the tracking performance of each controller under the three payload conditions is shown in Table 6.2.3.

Table 6.2.1: SSE values [deg] for controllers under varying payload for trajectory 1

	Test 1	Test 2	Test 3	Test 4	Test 5	Range
FF + PVA controller						
6.5 grams	-0.35	-1.17	0.94	0.57	-1.12	± 1.17
13.5 grams	-0.75	0.04	-0.64	-0.67	-1.19	± 1.19
Sliding mode controller						
6.5 grams	-0.53	-0.13	-0.2	-0.84	-0.58	± 0.84
13.5 grams	-0.1	-0.34	-0.25	-0.42	-0.38	± 0.42

Table 6.2.2: RMSE values [deg] for controllers under varying payload

		Test 1	Test 2	Test 3	Test 4	Test 5	Mean	Std. Dev.
FF + PVA controller								
6.5 g	Trajectory 1	1.92	1.28	1.88	1.78	1.58	1.69	0.24
	Trajectory 3	1.91	1.68	1.86	2.06	2.01	1.91	0.13
13.5 g	Trajectory 1	1.64	1.44	1.65	1.85	2.17	1.75	0.25
	Trajectory 3	2.07	1.99	2.15	1.97	2.06	2.05	0.06
Sliding mode controller								
6.5 g	Trajectory 1	1.52	1.24	1.13	1.34	1.30	1.31	0.13
	Trajectory 3	1.38	1.43	1.61	1.60	1.58	1.52	0.12
13.5 g	Trajectory 1	1.15	1.23	1.05	1.15	1.54	1.22	0.17
	Trajectory 3	1.74	1.74	1.79	1.84	1.74	1.77	0.04

Table 6.2.3: Effect of varying payload on controllers' tracking performance [deg]

	Controller	SSE Range	RMSE Mean
Trajectory 1			
No mass	FF + PVA	± 0.77	1.40
	Sliding mode	± 0.85	1.19
6.5 grams	FF + PVA	± 1.17	1.69
	Sliding mode	± 0.84	1.31
13.5 grams	FF + PVA	± 1.19	1.75
	Sliding mode	± 0.42	1.22
Trajectory 3			
No mass	FF + PVA	NA	2.09
	Sliding mode	NA	1.69
6.5 grams	FF + PVA	NA	1.91
	Sliding mode	NA	1.52
13.5 grams	FF + PVA	NA	2.05
	Sliding mode	NA	1.77

As can be seen from the SSE and RMSE values in Table 6.2.3, varying the payload has no significant degrading effect on the tracking performance of either controller. Therefore, both controllers seem to be robust in their responses to variation in the payload carried by the joint.

6.3 Vertical Motion Experiments

In order to test the FF + PVA and sliding mode controllers' robustness to changes in orientation, the joint was turned on its side and subjected to a series of vertical motion experiments.

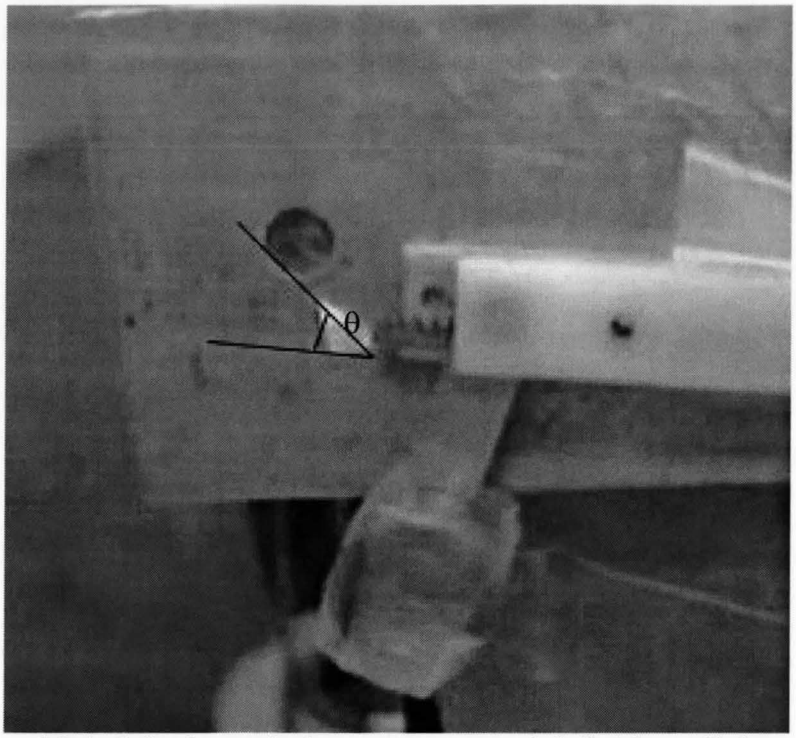

Figure 6.3.1: Joint in vertical arrangement and definition of joint angle.

Three experiments were conducted for each controller: no load, lifting a 6.5 g mass, and lifting a 13.5 g mass. Each experiment was repeated five times for each controller. The same two trajectories used in the varying payload experiments were tested. The SSE results for trajectory 1 are shown in Table 6.3.1, while the RMSE results for all of the tests are shown in Table 6.3.2. A comparison of the horizontal and vertical results is shown in Table 6.3.3.

Table 6.3.1: Trajectory 1 SSE [deg] results for vertical motion tests.

	Test 1	Test 2	Test 3	Test 4	Test 5	Range
FF + PVA controller						
No mass	1.08	0.93	-0.50	-0.77	-0.36	± 1.08
6.5 grams	-0.40	0.81	0.52	0.24	0.27	± 0.81
13.5 grams	0.57	0.25	0.28	0.46	-0.50	± 0.57
Sliding mode controller						
No mass	0.18	-0.77	-0.12	0.16	-0.86	± 0.86
6.5 grams	-0.20	-0.04	-0.68	0.06	-0.30	± 0.68
13.5 grams	-0.63	-0.58	-0.90	-0.11	-0.82	± 0.90

Table 6.3.2: Tracking performance RMSE values [deg] for vertical motion tests.

		Test 1	Test 2	Test 3	Test 4	Test 5	Mean	Std. Dev.
FF + PVA controller								
No mass	Trajectory 1	2.00	1.76	1.42	1.48	1.49	1.63	0.22
	Trajectory 3	2.33	2.28	2.44	2.59	2.34	2.40	0.11
6.5 g	Trajectory 1	1.95	1.76	1.72	1.39	1.75	1.72	0.18
	Trajectory 3	2.79	3.10	3.28	2.79	3.38	3.07	0.24
13.5 g	Trajectory 1	4.85	4.84	5.04	3.94	4.09	4.55	0.45
	Trajectory 3	2.95	4.04	4.55	3.64	4.80	4.00	0.66
Sliding mode controller								
No mass	Trajectory 1	1.47	1.94	1.59	1.33	1.54	1.57	0.20
	Trajectory 3	2.04	1.84	1.85	1.84	2.11	1.94	0.12
6.5 g	Trajectory 1	1.55	1.30	1.68	1.60	1.42	1.51	0.13
	Trajectory 3	2.03	1.90	2.29	2.23	2.17	2.12	0.14
13.5 g	Trajectory 1	2.71	3.79	4.02	3.72	3.14	3.48	0.48
	Trajectory 3	2.58	2.49	2.78	2.33	2.78	2.59	0.18

Table 6.3.3: Comparison of RMSE [deg] for horizontal and vertical tests of trajectory 3.

Controller	Horizontal (no mass)	Vertical (no mass)	Vertical (6.5 g mass)	Vertical (13.5 g mass)
FF + PVA	2.09	2.40	3.07	4.00
Sliding mode	1.69	1.94	2.12	2.59

It can be seen from Table 6.3.3 that changing to a vertical motion degraded the tracking performance of both controllers. Also, as the mass attached to the end of the joint was increased the performance deteriorated further. This is due to the increased effect of the unmodeled gravity force acting against the controller response. In comparing the controllers, the sliding mode control is more robust to changes in vertical orientation than the FF + PVA controller. For instance, the percentage increase in RMSE between the horizontal case and the vertical case with a payload of 13.5 g is 91.4 % for the FF + PVA controller and only 53.3 % for the sliding mode controller. The main reason for the performance difference is that the sliding mode controller can better adapt to modeling errors and disturbances due to its increased control response. In addition, the switching action of the sliding mode control is purely error dependant and thus not affected by modeling errors. Finally, one can observe from Table 6.3.2 that the sliding mode control on average leads to lower standard deviations, making the tracking performance more repeatable in the face of disturbances.

One should note from Table 6.3.1 that while the dynamic tracking ability of the controllers diminished with the vertical tests, the SSE was not adversely affected. This means that while the velocity of the joint was slowed down by the gravity force, the joint was still able to reach its final destination.

It was found during the vertical tests of the sinusoidal trajectory, that the directional dependency of the tracking performance worsened with increasing payload. When the joint is rotating upwards from 20° to 140° the controller must work against gravity. However, when the joint moves downwards, gravity acts in the direction of motion causing the joint to move faster. The controller has trouble compensating for the increased velocity and the motion of the joint becomes jerky, leading to poorer tracking performance. A plot of one of the sinusoidal tracking experiments using the sliding mode controller that demonstrates this phenomenon is shown in Figure 6.3.1.

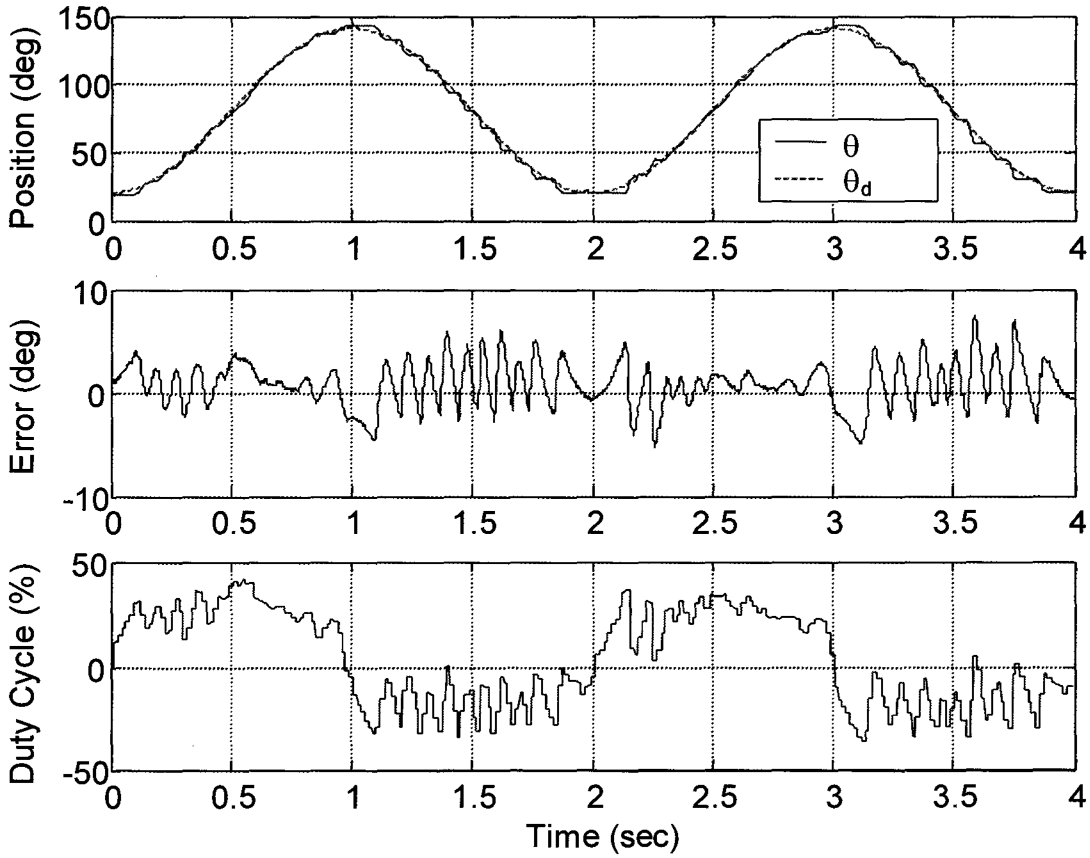

Figure 6.3.2: Trajectory 3 tracking performance for vertical motion with 13.5 g payload.

6.4 Conclusions

In this chapter, the robustness to modeling errors and disturbances of the FF + PVA and sliding mode controllers was tested through two experiments: varying payload and vertical motion. It was found that both controllers were robust to changes in payload, but suffered deterioration in tracking performance during the vertical motion tests. The deterioration increased with increasing payload in the vertical direction. The sliding mode controller was found to be the more robust to vertical motion with a maximum RMSE increase of 53.3 % compared to 91.4 % for the FF + PVA controller. Finally, vertical motion was found to amplify the effect of motion direction on the tracking performance of both controllers.

CHAPTER 7

CONCLUSIONS

7.1 Summary

The research presented in this thesis consisted of two parts: the design of a miniature rotary joint and the development of a servo positioning system. The joint was driven by two miniature cylinders using low-pressure water as their working fluid. The linear motion of the cylinder shafts was converted to rotation through the use of a small rack and pinion mechanism. In developing the servo positioning system the dynamics of the joint, valves and water were modelled. Three controllers were designed, simulated and experimentally tested. The three controllers were a linear PVA controller, a non-linear PVA plus model-based feedforward controller (PVA + FF) and the PVA + FF controller coupled with sliding mode control. Both non-linear controllers were found to be robust to changes in mass payload. The PVA + FF plus sliding mode controller was more robust to carrying payloads in the vertical direction than the PVA + FF controller.

7.2 Achievements

The major achievements of this research are as follows:

(1) A rack and pinion design was implemented with miniature cylinders of 4 mm bore diameter to create a miniature rotary joint capable of meeting both the size and torque specifications required by the application. This design showed

the feasibility of using off-the-shelf miniature cylinders for miniature robotic applications.

(2) An innovative micro position sensor was designed using a Hall-effect sensor and small rectangular bar magnet and installed inside the joint mechanism. The development of the sensor allowed for direct measurement of the joint position, which led to a high level of accuracy and the ability of the joint to meet its overall size requirements.

(3) A novel valve model was developed for on/off solenoid valves, which related PWM duty cycle to the valve flow resistance. This model allowed inexpensive on/off solenoid valves to be used and gave the valves the ability to approximate the function of proportional valves. This was critical for successful position control of the joint since adequate affordable proportional solenoid valves were not commercially available.

(4) A novel control strategy was designed for controlling the on/off solenoid valves that involved the addition of sliding mode control within the 16 ms PWM period. The sliding mode action increased the control resolution by decreasing the response time of the controller from 16 ms to 1 ms resulting in improved position tracking performance and more robust control (see next two points).

(5) The PVA + FF and PVA + FF plus sliding mode controllers achieved steady-state errors of $\pm 0.77^\circ$ and $\pm 0.85^\circ$, or ± 0.06 mm and ± 0.07 mm in terms of rack position, respectively. The maximum tracking errors for both controllers

was 5^{o} (0.41 mm), occurring during the initial portion of the cycloidal rising in trajectory 1. Also, when compared to the performance of the PVA controller the PVA + FF controller achieved an average reduction of 42% in the RMSE, while the PVA + FF plus sliding mode controller was able to reduce the RMSE by an average of 54%.

(6) Both controllers were robust to changes in payload mass. When varying the payload for motion in the vertical direction the PVA + FF plus sliding mode controller was found to be more robust achieving on average a 30 % reduction in RMSE compared to the PVA + FF controller.

7.3 Recommendations for Future Work

(1) To maintain a more constant water supply pressure, alternative pressurized supply sources, such as an accumulator, should be investigated to replace the current air-over-water system. Achieving a more constant supply pressure will allow for increased position control performance.

(2) Since friction is the dominant dynamic in the system it has a dramatic effect on controller performance. To increase the accuracy of the friction model a map of the static friction variation over the position range of the joint should be studied. This can be accomplished by activating the joint from different rest positions. The joint can be commanded to the desired rest positions using one of the current controllers. It is recommended that a duty cycle of 100 % be used to minimize oscillations in the pressure data. Also, pressures low enough

to just move the joint should be used so as to not overestimate the static friction values.

(3) Periodic searches should be made for proportional solenoid valves that offer flow rate and pressure ratings comparable to that of the on/off solenoid valves. The valves that were used in this thesis could not achieve flow rates below 1×10^{-6} m^3/s. If available, affordable proportional valves should improve the performance of the position control by allowing for finer flow rate resolution.

(4) In this thesis a PWM period of 16 ms was used for all the control algorithms throughout. As previously mentioned, this time period was selected to balance the opposing requirements of high position control resolution against fast control response time. Other PWM time periods should be tried to observe their effects on the tracking performance of the controllers.

(5) Other control techniques could be implemented to try and improve the position tracking performance of the joint. One suggestion would be to implement a PVA controller in a similar manner as the sliding mode control to determine if similar results are obtained.

(6) The current velocity and acceleration observers should be replaced with model-based versions to determine the impact on signal quality.

REFERENCES

[1] K. Uchino and J. R. Giniewicz, *Micromechatronics*. New York: Marcel Dekker Inc., 2003.

[2] J. D. Nicoud, O. Matthey, and G. Caprari, "Control and Analysis of Low Inertia Miniature Synchronous Motors", *IEEE International Symposium on Micromechatronics and Human Science*, 1998, pp. 97-103.

[3] Maxon Motor USA: Products and Specs. Retrieved from the World Wide Web: Oct. 4, 2004. http://www.maxonmotorusa.com/products/

[4] Faulhaber: Products and Specs. Retrieved from the World Wide Web: Oct. 10, 2004. http://www.faulhaber-group.com/n164058/n.html

[5] K. B. Yesin, *Design of Meso-Scale Robotic Systems with Miniature Actuators*. UMN-AML-TR-00-02. Minneapolis, Minn: University of Minnesota, 2000. Retrieved from the World Wide Web: Nov. 3, 2004. http://www.me.umn.edu/divisions/design/adv_microsystems/techreports/umn-aml-tr-00-02.pdf

[6] H. Yamashita, D. Kim, N. Hata, and T. Dohi, "Multi-Slider Linkage Mechanism for Endoscopic Forceps Manipulator", *Proceedings of the IEEE/RSJ International Conference on Intelligent Robots and Systems*, Las Vegas, Nevada, October 2003, pp. 2577-2582.

[7] J. Peirs, D. Reynaerts and H. Van Brussel, "A Miniature Manipulator for Integration in a Self-Propelling Endoscope", *The 14th European Conference on*

Solid-State Transducers, Copenhagen, Denmark, August 27-30 2000, pp. 309-312.

[8] P. Dario, M. C. Carrozza, C. Stefanini and S. D'Attanasio, "A Mobile Microrobot Actuated by a New Electromagnetic Wobble Micromotor", *IEEE/ASME Transactions on Mechatronics*, Vol. 3, No. 1, pp. 9-16, March 1998.

[9] T. Fukuda, H. Hosokai and M. Uemura, "Rubber Gas Actuator Driven by Hydrogen Storage Alloy for In-pipe Inspection Mobile Robot with Flexible Structure", *Proceedings of the IEEE International Conference on Robotics and Automation*, 1989.

[10] P. Kallio, M. Lind, Q. Zhuo and H. N. Koivo, "A 3 DOF Piezohydraulic Parallel Micromanipulator", *Proceedings of the IEEE International Conference on Robotics & Automation*, Leuven, Belgium, May 1998, pp. 1823-1828.

[11] K. Suzumori, S. Iikura and H. Tanaka, "Development of Flexible Microactuator and Its Applications to Robotic Mechanisms", *Proceedings of the IEEE International Conference on Robotics and Automation,* Sacramento, California, April 1991, pp. 1622-1627.

[12] J. Peirs, D. Reynaerts and H. Van Brussel, "A Miniature Hydraulic Parallel Manipulator for Integration in a Self-propelling Endoscope", *The 13th European Conference on Solid-State Transducers,* The Hague, The Netherlands, September 12-15 1999, pp. 753-756.

[13] T. Morita, "Miniature Piezoelectric Motors", *Sensors and Actuators*, Vol 103, pp. 291-300, 2003.

[14] Physikinstrument: P-915K094 Product Spec Sheet. Retrieved from the World Wide Web: Nov. 8, 2004.
http://www.pi-china.cn/pdf/pdf/PI_PIline.pdf

[15] A. M. Flynn, "Performance of Ultrasonic Mini-motors Using Design of Experiments", *Smart Material Structures*, Vol. 7, pp. 286-294, 1998.

[16] K. Tani, M. Suzuki, K. Furuta, T. Sakuhara and T. Ataka, "Development of a New Type Piezoelectric Micromotor", *Proceedings of the 11th Annual International Workshop on Micro Electro Mechanical Systems*, January 1998, Vol. 25, No. 29, pp.396-401.

[17] M. Bexell and S. Johansson, "Fabrication and Evaluation of a Piezoelectric Miniature Motor", *Sensors and Actuators*, Vol. 75, pp. 8-16, 1999.

[18] M. Bexell, S. Johansson, "Characteristics of a Piezoelectric Miniature Motor", *Sensors and Actuators*, Vol. 75, pp. 118-130, 1999.

[19] S. Dong et al, "Piezoelectric Ultrasonic Micromotor with 1.5 mm Diameter", *IEEE Transactions on Ultrasonics, Ferroelectrics, and Frequency Control*, Vol. 50, No. 4, pp. 361-367, April 2003.

[20] Muscle Wires: Mondotronics Product Website. Retrieved from the World Wide Web: Feb. 17, 2005.
http://www.mondotronics.com/shapememoryalloys.shtml

[21] J. Peirs, D. reynaerts and H. Van Brussel, "The 'True' Power of SMA Micro-Actuation", *Proceedings of the Micromechanics Europe Workshop*, Cork, Ireland, 2001, pp. 217-220.

[22] M. A. Thrasher, A. R. Shahin, P. H. Meckl and J. D. Jones, "Efficiency Analysis of Shape Memory Alloy Actuators", *Smart Material Structures*, Vol. 3, pp. 226-234, 1994.

[23] Y. Nakamura, A. Matsui, T. Saito and K. Yoshimoto, "Shape-Memory-Alloy Forceps for Laparoscopic Surgery", *IEEE International Conference on Robotics and Automation*, 1995, pp. 2320-2327.

[24] K. Ikuta, M. Tsukamoto and S. Hirose, "Shape Memory Alloy Servo Actuator System with Electric Resistance Feedback and Application for Active Endoscope", *Robotics and Automation*, Vol. 1, pp. 427-430, 1988.

[25] J. Peirs, D. Reynaerts and H. Van Brussel, "Shape Memory Micro-Mechanisms for Medical Applications", *The 8th International Conference on Advanced Robotics*, Monterey, California, July 7 – 9, 1997, pp. 155-160.

[26] H. H. Asada, S. Mascaro and B. Roy, "High-Speed Shape Memory Actuators Using a Fluidic Circulatory System", *Progress Report No. 3-3 for MIT Home Automation and Healthcare Consortium*, March 31, 2002.

[27] T. Hino and T. Maeno, "Development of a Miniature Robot Finger with a Variable Stiffness Mechanism using Shape Memory Alloy", *International Symposium on Robotics and Automation*, Queretaro, Mexico, August 25-27, 2004.

[28] R. H. Baughman, "Conducting Polymer Artificial Muscles", *Synthetic Metals*, Vol. 78, pp. 339-353, 1996.

[29] Y. Bar-Cohen, "Electroactive Polymers as Artificial Muscles – Reality and Challenges", *Proceedings of the 42nd AIAA Structures, Structural Dynamics, and*

Materials Conference, Gossamer Spacecraft Forum, Seattle, Washington, April 16-19 2001.

[30] A. Della Santa, D. De Rossi and A. Mazzoldi, "Characterization and Modelling of a Conducting Polymer Muscle-like Linear Actuator", *Smart Material Structures*, Vol. 6, pp. 23-34, 1997.

[31] S. Hara, T. Zama, W. Takashima and K. Kaneto, "Polypyrrole-metal Coil Composite Actuators as Artificial Muscle Fibres", *Synthetic Metals*, Vol. 146, pp. 47-55, 2004.

[32] J. D. Madden, R. A. Cush, T. S. Kanigan and I. W. Hunter, "Fast Contracting Polypyrrole Actuators", *Synthetic Metals*, Vol. 113, pp. 185-192, 2000.

[33] E. W. H. Jager, O. Inganas and I. Lundstrom, "Microrobots for Micrometer-Size Objects in Aqueous Media: Potential Tools for Single-Cell Manipulation", *Science*, Vol. 288, pp. 2335-2338, June 30, 2000.

[34] J. D. Madden et al, "Encapsulated Polypyrrole Actuators", *Synthetic Metals*, Vol. 105, pp. 61-64, 1999.

[35] S. H. Cho et al, "Sliding Mode Tracking Control of a Low-Pressure Water Hydraulic Cylinder Under Non-Linear Friction", *Journal of Systems and Control Engineering*, Vol. 216, pp. 383-392, 2002.

[36] M. Linjama et al, "On/Off Position Control of Low-Pressure Water Hydraulic Cylinder Using Low-Cost Valves", Linkoping, Sweden, May 31 – June 1, 2001, pp. 41-55.

[37] T. Noritsuga, "Development of PWM Mode Electro-Pneumatic Servomechanism Part II: Position Control of a Pneumatic Cylinder", *Journal of Fluid Control*, Vol. 17, No. 2, pp. 7-28, 1987.

[38] K. Kurz et al, "Developing a Flexible Automated Fixturing Device", *Mechanical Engineering*, pp. 59-63, July 1994.

[39] R. B. van Varseveld and G. M. Bone, "Accurate Position Control of a Pneumatic Actuator Using On/Off Solenoid Valves", *IEEE/ASME Transactions on Mechatronics*, Vol. 2, No. 3, pp. 195-204, September 1997.

[40] L. Rong et al, "Theoretical and Experimental Study on Hydraulic Servo Position Control System with Generalization Pulse Code Modulation Control", *Conference on Fluid Power Transmission and Control*, Hangzhou, China, April 3-5, 2001, pp. 176-179.

[41] F. Malaguti and E. Pregnolato, "Proportional Control of On/Off Solenoid Operated Hydraulic Valve by Nonlinear Robust Controller", *Proceedings of the 2002 IEEE International Symposium on Industrial Electronics*, Vol. 2, pp. 415-419, 2002.

[42] A. K. Paul, J. K. Mishra and M. G. Radke, "Sliding Mode Control of Pneumatic Actuator for Robotic Application", *Proceedings of the 1993 IEEE/RSJ International Conference on Intelligent Robots and Systems*, Yokohama, Japan, July 26-30, 1993, pp. 1268-1275.

[43] A. K. Paul, J. K. Mishra and M. G. Radke, "Reduced Order Sliding Mode Control for Pneumatic Actuator", *IEEE Transactions on Control Systems Technology*, Vol. 2, No. 3, pp. 271-276, 1994.

[44] Z. Rao, "Modeling and Control of Miniature Servo Pneumatic Actuators", M.A.Sc. dissertation, McMaster University, Hamilton, ON, Canada, 2005.

[45] Boston Gear: Gear Catalog pp. 142. Retrieved from the World Wide Web: May 19, 2005.
http://bostongear.com/pdf/catalogs/P-1482-BG_cat-OpenGearing.pdf

[46] R. A. Serway, *Physics for Scientists and Engineers*, 4th Edition. Toronto: Saunders College Publishing, 1996.

[47] A. J. Smits, *Fluid Mechanics*, 1st Edition. Toronto: John Wiley & Sons, Inc., 2000.

[48] J. L. Shearer, B. T. Kulakoski and J. F. Gardner, *Dynamic Modeling and Control of Engineering Systems*, 2nd Edition. New Jersey: Prentice Hall, 1997.

[49] S. Ning and G. Bone, "Development of a Nonlinear Dynamic Model for a Servo Pneumatic Positioning System", *Proceedings of the IEEE International Conference on Mechatronics & Automation*, Niagra Falls, Canada, July 2005, pp. 43-48.

APPENDIX A

CALCULATION OF SYSTEM'S DYNAMIC MASS

Dynamic Mass Components

The dynamic mass of the hydraulic servo system includes the following items:

- the shafts and pistons of the two miniature cylinders
- the two racks, pinion gear and reduction spur gear
- the output link
- the water contained in the miniature cylinder chambers and inside all of the tubing located between the water supply pressure sensor and the discharge tank

The above control volume for the water was selected to match the control volume of the system's dynamic equation as derived in chapter 4.

Mass of Linear Moving Components

Rack (m_{rack}): 0.46 grams (measured)

Cylinder shaft and piston (m_{cyl}): 2 grams (from manufacturer's spec sheet)

Water (m_{water}): 27.16 grams (ρ_{water} x volume of tubing = 1000 kg/m^3 x 2.716 x 10^{-5} m^3)

Moment of Inertia of Rotating Components

The moment of inertia for both the pinion gear and spur gear can be calculated as the moment of inertia of a larger disk with diameter equal to the gear's pitch diameter minus the moment of inertia of the gear's hole. For the pinion gear this gives,

$$J_{pinion} = \frac{1}{2} m_o r_o^{\ 2} - \frac{1}{2} m_h r_h^{\ 2}$$

where m_o and r_o are the mass and radius of the outer disk and m_h and r_h are the mass and radius of the hole. Given that the pinion is made of brass with a density of 8500 kg/m^3, has a pitch radius of 1.85 mm, a hole radius of 0.79 mm and is 3.18 m high, its moment of inertia can be calculated as,

$$J_{pinion} = \frac{1}{2} \rho V_o r_o^{\ 2} - \frac{1}{2} \rho V_h r_h^{\ 2} = \frac{1}{2} \rho(\pi h r_0^{\ 2}) r_o^{\ 2} - \frac{1}{2} \rho(\pi h r_h^{\ 2}) r_h^{\ 2} = 4.8x10^{-10}\, kg/m^2 .$$

Completing a similar calculation for the spur gear which has a pitch radius of 4.77 mm, a hole radius of 1.2 mm and a height of 1.59 mm gives a moment of inertia of,

$$J_{spur} = 1.095x10^{-8}\, kg/m^2 .$$

The moment of inertia of the joint's output link can be calculated by modeling the link as a beam and calculating its moment of inertia around its point of rotation (the shaft). Given that the mass of the link was measured to be 0.6 grams the moment of inertia can be calculated as,

$$J_{link} = \frac{1}{3} m_l l^2 = 2.45x10^{-7}\, kg/m^2 \ .$$

<u>Equivalent Linear Moving Mass of Rotating Components</u>

Since a linear moving mass of the system is desired for the system dynamics equation the calculated moment of inertias for the rotating parts must be converted to equivalent linear moving masses. This can be accomplished by manipulating the fundamental dynamic equations for force and torque as follows:

$$F = \frac{T}{r} \rightarrow ma = \frac{J\alpha}{r} = \frac{Ja}{r^2}$$

where F is the force, T is the torque, α is the angular acceleration and r is the radius of the component in question.

Using the above relationship the linear moving masses of the pinion, spur gear and output link can be found to be,

Pinion: $m_{eqPINION} = \frac{J_{pinion}}{r^2} = 0.14g$

Spur Gear: $m_{eqSPUR} = \frac{J_{spur}}{r^2} = 0.48g$

Output Link: $m_{eqLINK} = \frac{J_{link}}{r^2} = 0.2g$

Total Moving Mass of System

The total moving mass of the system is given by,

$M = m_{water} + 2m_{rack} + 2m_{cyl} + m_{eqPINION} + m_{eqSPUR} + m_{eqLINK} = 32.9$ grams.

APPENDIX B

WIRE CONNECTIONS

Sensor	From	To	Wire Colour
Pressure Sensor 1 (Cylinder A)	Pin 1	+5V/ power supply	Red
	Pin 2	GND/ power supply	Grey
	GND/ power supply	Terminal 67 (AI GND)	Grey
	Pin 3	Terminal 33 (AI 1)	Purple
Pressure Sensor 2 (Cylinder B)	Pin 1	+5V/ power supply	Red
	Pin 2	GND/ power supply	Grey
	GND/ power supply	Terminal 32 (AI GND)	Grey
	Pin 3	Terminal 65 (AI 2)	Light Green
Pressure Sensor 3 (Water Supply)	Pin1	+5V/ power supply	Red and Black
	Pin 2	GND/ power supply	Black
	GND/ power supply	Terminal 64 (AI GND)	Black
	Pin 3	Terminal 30 (AI 3)	Cream
Valve 1 (Cylinder A supply)	Middle pin	VO-/ DD	Black
	Outer pin	VO+/ DD	Black
	BO-/ DD	Terminal 18 (DGND)	Grey
	B0+/ DD	Terminal 52 (P 0.0)	Yellow
Valve 2 (Cylinder A discharge)	Middle pin	V1-/ DD	Black
	Outer pin	V1+/ DD	Black
	B1-/ DD	Terminal 50 (DGND)	Grey
	B1+/ DD	Terminal 17 (P 0.1)	White
Valve 3 (Cylinder B supply)	Middle pin	V2-/ DD	Black
	Outer pin	V2+/ DD	Black
	B2-/ DD	Terminal 15 (DGND)	Grey
	B2+/ DD	Terminal 49 (P 0.2)	Light blue
Valve 4 (Cylinder B discharge)	Middle pin	V3-/ DD	Black
	Outer pin	V3+/ DD	Black
	B3-/ DD	Terminal 13 (DGND)	Grey
	B3+/ DD	Terminal 47 (P 0.3)	Green
Hall-effect sensor	Pin 1	+5V/ power supply	Grey
	Pin 2	GND/ power supply	Grey
	Pin 2	Terminal 29 (AI GND)	Grey
	Pin 3	Terminal 28 (AI 4)	Grey

- Pins refer to sensors, terminal refers to NI DAQmx board (PCI-6221)
- DD refers to the digital converter box